ANALYSIS OF ORTHOGONAL EDGE TRIMMING OF UNI-DIRECTIONAL COMPOSITES: NUMERICAL, ANALYTICAL, AND EXPERIMENTAL APPROACH

A Dissertation by

Ashkan Sahraie Jahromi

M.S. in Mechanical Engineering, Amir Kabir University of Technology at Iran, 2003

B.S. in Mechanical Engineering, Amir Kabir University of Technology at Iran, 2001

Submitted to the Department of Mechanical Engineering
and the faculty of the Graduate School of
Wichita State University
in partial fulfillment of
the requirements for the degree of
Doctor of Philosophy

May 2010

ANALYSIS OF ORTHOGONAL EDGE TRIMMING OF UNI-DIRECTIONAL COMPOSITES: NUMERICAL, ANALYTICAL, AND EXPERIMENTAL APPROACH

The following faculty members have examined the final copy of this dissertation for form and content, and recommend that it be accepted in partial fulfillment of the requirement for the Doctor of Philosophy with a major in Mechanical Engineering.

Behnam Bahr, Committee Chair

Hamid Lankarani, Committee Member

Keshavanarayana Raju, Committee Member

Brian Driessen, Committee Member

Ramazan Asmatulu, Committee Member

Accepted for the College of Engineering

Zulma Toro-Ramos, Dean

Accepted for the Graduate School

J. David McDonald, Dean

DEDICATION

To my parents, my wife, my sister, and my brother

Love, optimism, and peace of mind act as brain boosters.

ACKNOWLEDGMENTS

I would like to express my deep and sincere gratitude to my advisor, Dr. Behnam Bahr, former faculty member of the Department of Mechanical Engineering at Wichita State University. His wide knowledge, logical way of thinking, understanding, and support have been of great value to me. Above all, I sincerely thank Dr. Bahr for funding me throughout my doctoral studies.

I extend my gratitude to my committee members, Dr. S. Keshavanarayana Raju, Dr. M. Hamid Lankarani, Dr. B. Brian Driessen, and Dr. Ramazan Asmatulu, for their helpful comments, support, and suggestions.

I am grateful to my beloved wife, Niloufar Mahmoudnejad, for her support, understanding, and help throughout my dissertation. Without her assistance, I would not have been able to finish this study.

I take this opportunity to express my sincere gratitude to my father, mother, brother, and sister for providing me spiritual and financial support.

I am grateful to all the faculty and staff of the Department of Mechanical Engineering for their constant support and guidance throughout the duration of my studies at Wichita State University.

I am sincerely grateful to Spirit AeroSystems (Dan Thurnau, John Boccia), Hawker Beechcraft (Dave Richardson, Brad Moss, Marvyn Rock), Cessna Aircraft Company (Kececi Erkan, Dhananjay Joshi, Carolyn Wyatt), and Precision Dormer Inc. (Gary Kirchhoff and Brian Carpenter) for supporting this project and providing valuable suggestions.

I take this opportunity to express my sincere gratitude to the faculty and staff of Wichita Area Technical College (WATC), especially Mark Meek, for providing me guidance and support and the required infrastructure for my experimentation.

In particular, many thanks to Heath Misak for his valuable help and contribution to the enjoyment of my studies, always with a broad smile on his face.

I wish to give my sincere thanks to the Ablah Library staff at Wichita State University and the Interlibrary Loan personnel for their hard work providing research recourses. In particular, I thank Betty Sherwood, who fielded my numerous requests with a degree of tolerance above and beyond the call of duty.

A very special thank you to Kristie Bixby for her invaluable help with the final language editing of my thesis and for her kindness.

Also, many thanks to Dr. Klaus A. Hoffmann for his friendly help with my dissertation.

Last, but not least, I take this opportunity to thank Khan Habeeb Ur Rahman for his valuable help and support in successfully completing this thesis.

ABSTRACT

As the use of composites increases, more problems arise with processing and manufacturing of this type of material in order to make it a more durable and reliable for today's applications. One of the most important problems in the cutting of composites is the poor quality of the machined surface and unknown status of the machining forces. Knowing the status of forces during the final machining process helps reduce such defects as delamination and fiber-matrix debonding. This research attempted to develop a fully theoretical model for edge trimming of composites for fiber orientations greater than 90 degrees. The energy method was used as the approach, and the machining forces were compared to the experimental results. A series of experiments were conducted to validate the theoretical foundations.

Composite coupons with different fiber orientations and tool rake angles were prepared for the machining experiments, and the cutting forces were measured using a four-component dynamometer. In addition, a finite element model (FEM) was built to model the depth of damage along the fibers. The theoretical depth of damage compared to the FEM analysis showed that they were in good agreement. The parameters affecting the machining forces of composites can be divided into three categories: tool geometry, material properties, and machining conditions. The effect of all of these parameters is reflected in the formula. In addition to the thrust and cutting forces, the depth of damage along the fibers can be calculated.

It was concluded that the material properties and machining conditions, more than the geometry of an orthogonal cutting tool, are more influential in affecting the processing and manufacturing of composite materials.

TABLE OF CONTENTS

Chapter **Page**

TABLE OF CONTENTS (Continued)

Chapter **Page**

TABLE OF CONTENTS (Continued)

Chapter **Page**

LIST OF TABLES

Table **Page**

LIST OF FIGURES

Figure **Page**

LIST OF FIGURES (Continued)

Figure **Page**

LIST OF FIGURES (Continued)

Figure **Page**

LIST OF FIGURES (Continued)

Figure **Page**

LIST OF FIGURES (Continued)

Figure **Page**

LIST OF SYMBOLS

A_0	undeformed chip cross-sectional area
A_s	deformed chip cross-sectional area
A_m	matrix cross-sectional area associated with one fiber
B	amplitude of the waviness of the fibers
B_0	initial amplitude of the waviness of the fibers
B_c	critical waviness amplitude
B_c^{shear}	critical waviness amplitude in matrix shear failure
B_c^{bend}	critical waviness amplitude in fiber-bending failure
C	constant
D_{ijkl}	material constants
D	damage variable
E_i	Young modulus in i direction
E_c	adhesive material stiffness
E_f	Young modulus of fiber
E_m	Young modulus of matrix
E_1^t	tensile modulus in 1 direction
E_1^c	compressive modulus in 1 direction
E_2^t	tensile modulus in 2 direction
E_2^c	compressive modulus in 2 direction
F_c	cutting force
F_t	thrust force

LIST OF SYMBOLS (Continued)

F_r	normal force in oblique cutting
F	friction force along tool
F_n	normal force on the shear plane
F_s	shear force in Region 1
F_{y_i}	horizontal cutting force in Region i $(0 \leq \theta \leq 90)$
F_{z_i}	vertical cutting force in Region i $(0 \leq \theta \leq 90)$
G_{ij}	shear modulus in ij plane
G^C	dissipated failure energy
G_n, G_s, G_t	work done by the traction and its conjugate relative displacement in the normal, first, and second-shear directions, respectively
G_n^C, G_s^C, G_t^C	critical fracture energies
G_m	shear modulus of matrix
G_{LT}	shear modulus of a circular fiber-reinforced composite
H	depth of cut
I_f	second moment of area of the cross section of the fiber
K_{cc}	cutting constant for cutting force
K_{tc}	cutting constant for thrust force
K_{rc}	cutting constant for normal force
K	coefficient to be determined by experiment
K_c	stiffness of interface
L	reinforcement length

LIST OF SYMBOLS (Continued)

M	resultant moment on the fiber
N	normal force to rake face of tool
N	total bouncing force
P_{real}	real resultant force in Region 2 $(0 \leq \theta \leq 90)$
P	buckling axial force
P_{cr}	critical buckling axial force
R	cutting resultant force
S	shear failure strength
S_{ij}	shear failure in ij plane
T_0	original thickness of the cohesive element
T_c	cohesive layer thickness
T	total external work
V	linear velocity
V_f	strain energy in fiber
V_m	strain energy in matrix
V	resultant shear force on fiber
X_1	tensile (compressive) strength in direction 1
X_2	tensile (compressive) strength in direction 2
X_t	tensile strength in direction 1
X_c	compressive strength in direction 1
X_c^f	flexure strength of fiber

LIST OF SYMBOLS (Continued)

Y_t	tensile strength in direction 2
Y_c	compressive strength in direction 2
a_c	feed rate (undeformed chip thickness)
a_0	deformed chip thickness
a_e	contact length
$2c$	reinforcement spacing
h	reinforcement thickness
k	volume fraction of reinforcement
k_s	material parameter
m	number of buckling waves
n	a coefficient
r_c	cutting ratio
r_e	tool nose radius
r	fiber radius
s	lateral force acting on the composite
t	traction vector
t_n	traction along the normal direction (local direction 3)
t_s	shear traction along the local direction 1 in three-dimensional problems
t_t	shear traction along the local direction 2 in three-dimensional problems
t_n^0, t_s^0, t_t^0	peak values of individual nominal stress
v_f	fiber volume fraction

LIST OF SYMBOLS (Continued)

v_m	matrix volume fraction
v	transverse displacement in fiber
v_0	initial waviness of fibers
v	waviness of fibers
ϕ	shear plane angle
ϕ_n	normal shear angle
ϕ_i	oblique shear angle
ψ_r	tool approach angle
α	clearance angle
α_n	normal clearance angle
β	friction angle
β_e	effective rake angle
$\beta^{'}$	back rake angle
γ	rake angle in orthogonal cutting tool
γ_n	normal rake angle
$\delta_n, \delta_s, \delta_t$	separation corresponding to each traction vector
δ_m^f	effective displacement at complete failure
δ_m^0	effective displacement at the initiation of damage
$\bar{\epsilon}_S^{pl}$	equivalent plastic strain at the onset of damage
$\epsilon_n^0, \epsilon_s^0, \epsilon_t^0$	peak values of individual nominal strain
η	sheared chip flow angle

LIST OF SYMBOLS (Continued)

θ	fiber orientation
θ_s	shear stress ratio
$\kappa_{r'}$	horizontal clearance
λ_s	cutting edge inclination
λ	end fixity of reinforcement
μ	friction coefficient
ν_{ij}	Poisson's ratio in ij plane
ν_f	Poisson's ratio of fiber
ν_m	Poisson's ratio of matrix
ρ_c	adhesive material density
$\bar{\rho}_c$	density of interface
σ_s	normal stress on shear plane
σ_{ij}	stress in ij direction
σ_{CE}	critical buckling stress in extension mode
σ_{CS}	critical buckling stress in shear mode
$\sigma_{f_{cr}}$	critical compressive fiber stress
$\sigma_{c_{cr}}$	critical compressive circular fiber-reinforced composite stress
σ_c	composite buckling strength for undulated fiber model
σ_c^{shear}	composite buckling stress for the matrix shear failure
σ_c^{bend}	composite buckling stress for the fiber-bending failure
τ_s	shear stress in shear plane

LIST OF SYMBOLS (Continued)

τ_{s_0}	shear stress on the shear plane at zero normal stress
τ_{max}	maximum shear stress
τ_{xym} , γ_{xym}	shear stress and strain in matrix
τ_c	shear strength of matrix

CHAPTER 1

INTRODUCTION

1.1. Fiber-Reinforced Composite Materials

Composite materials consist of two or more materials arranged or mixed together to produce desirable properties that cannot be achieved by themselves. For example, fiber-reinforced composite materials consist of high-strength and high-modulus fibers embedded in the matrix material. Here, the fibers are the principal load carrying members, and matrix material keeps the fibers together, acts as a load-transfer medium between fibers, and protects the fibers from being exposed to the environment (e.g., moisture, humidity, etc.).

The major difference between composites and alloys is that the materials forming alloys can be combined so that the resulting material is homogeneous and the components are indistinguishable with the naked eye; however, composites, if well designed, usually exhibit the best qualities of their components and often-other qualities that neither component possesses. Some of the properties that can be improved by forming a composite material are as follows [1]:

- strength
- stiffness
- corrosion resistance
- wear resistance
- attractiveness
- weight
- fatigue life
- temperature-dependent behavior
- thermal insulation
- thermal conductivity
- acoustical insulation

Of course, not all of these properties are improved simultaneously and usually there is no requirement to do so. Actually, depending on the required design specifications, components can be mixed so that the resulting material has only the characteristics needed to perform the task for which it is designed. A good example of a design factor would be thermal or electrical insulation versus thermal or electrical conductivity [1].

Composite materials have a long history of usage. The very first time they were used is not clear yet, but all recorded history contains references to some type of composites. For instance, straw was used by Israelites to strengthen mud bricks. The ancient Egyptians used plywood. They also realized that wood could be rearranged to achieve better strength and resistance to thermal expansion as well as absorb moisture to cause swelling. Medieval swords and armor were constructed with layers of different metals. More recently, fiber-reinforced, resin-matrix composite materials that have high strength-to-weight and stiffness-to-weight ratios have become important in weight-sensitive applications such as aircraft and space vehicles [1].

1.2. Classification and Characteristics of Composite Materials

Four common types of composite materials are as follows:

- *Fibrous* composite materials that consist of fibers in a matrix.
- *Laminated* composite materials that consist of layers of various materials.
- *Particulate* composite materials that are composed of particles in a matrix.
- *Combinations* of some or all of the first three types [1].

It is known that fibers are stiffer and stronger than the same material in bulk form since they have a near crystal-sized diameter and a very high length-to-diameter ratio, whereas matrix materials have their usual bulk-form properties.

Fiber-reinforced composite materials for structural applications are often formed in thin layers or laminas in the form of pre-impregnated. A lamina is a macro unit of material, the material properties of which are determined through appropriate laboratory tests. One can stack them in appropriate orientation in structural elements such as bars, beams, or plates to gain the best performance of the element for the specific application. Although fiber-reinforced polymers (FRPs) are generally fabricated as near-net-shape, additional machining is often necessary in order to trim the fabricated part to its final dimensions. The purpose of this study was to develop equations that estimate the machining forces in the cutting of unidirectional composite plates. The analysis of the machining forces used to form unidirectional composites involves an understanding of machining theories, composites failure theories, and structural theories (i.e., kinematics of deformation) [2].

The machining of FRPs differs in many aspects from the cutting of metals. The material behavior in composites is not only inhomogeneous but also depends on fiber and matrix mechanical properties, fiber orientation, tool geometry, and type of weave [3].

1.3. Research Rationale

This research effort focused on understanding the machinability of unidirectional carbon fiber-reinforced polymers (CFRP) during orthogonal cutting, since there is no reliable cutting theory for the machining of composites. The chip-formation mechanism in orthogonal machining of composites is different from that of metals; therefore, the cutting theories developed for metals cannot be used directly in the orthogonal machining of composites. In addition, more mechanisms are involved in the cutting of composites than for metals.

1.4. Objectives and Research Scope

The primary objective of this research was to study, by experiments and analysis, the cutting forces in orthogonal machining of unidirectional CFRP materials. Experiments were conducted using a single-edge turning tool. Orthogonal cutting forces were then compared to the developed theory. Knowledge of cutting forces and the effect of tool geometry and cutting direction will lead to better design of materials and tooling systems. The specific objectives of this research were as follows:

- To develop a theoretical and semi-empirical formula for the cutting forces in orthogonal cutting of unidirectional composite materials considering different involved cutting mechanisms.
- To investigate the effects of fiber orientation, cutting parameters, and tool geometry on the cutting mechanisms.
- To extend the developed theoretical cutting models to include multidirectional composites and machining with multi-edge cutting tools to improve the surface qualities of the workpiece [4].

1.5. Organization of Dissertation

The chapters of this research are organized as follows: Chapter 2 describes the geometry of single-edge cutting tools. Both orthogonal and oblique cutting tools and their geometries are explained in detail here. Chapter 3 describes different theories in metal cutting and the effects of tool geometry on thrust and cutting forces. In addition, different finite element and statistical-based force-prediction models are presented here. In Chapter 4, the developed mechanics model to predict the cutting and thrust forces for unidirectional FRP composites is described.

CHAPTER 2

BACKGROUND AND LITERATURE REVIEW

2.1. General

One of the problems in the machining of composites is related to the abrasiveness of reinforcement fibers, which causes fast tool wear and deterioration of the machined surface. Among damages that can result from abrasiveness, delamination is the major problem. Few theories and investigations have been published in this area, and they are primarily based on artificial neural network (ANN) or statistical analysis. One of the problems with ANN is that these theories are not reliable outside of their training domain. A discussion about the background of orthogonal and oblique cutting in order to understand the cutting mechanics of isotropic material will follow in sections of this chapter. This discussion will then be extended to the machining mechanisms of FRP composites in the chapters that follow.

First, orthogonal cutting tool geometry will be discussed. Then, orthogonal and oblique metal cutting mechanisms and force prediction theories using a single-edge cutting tool will be introduced. Following that, chip formation in the machining of FRP composites will be discussed from a machining point of view, and problems with machining of fiber-reinforced composites will be discussed briefly. This will be followed by discussion of the use of traditional machining processes in composite machining and developed orthogonal cutting models [4]. Finally, an analytical approach to find the machining forces will be presented.

2.2. Geometry of a Single-Edge Orthogonal Cutting Tool

Koshal [5] states that orthogonal is a simplified situation which is seldom met with in practice and most of the research into chip formation has been based on that. The tool approaches the work with its cutting edge parallel to the uncut work surface and at right angles to the direction of cutting. The tool as shown in Figure 2-1 is wider than the work to prevent end effects. Orthogonal cutting can be achieved only in a planing or shaping operation; however, a close approximation can be obtained when turning on the end of a thin-walled tube.

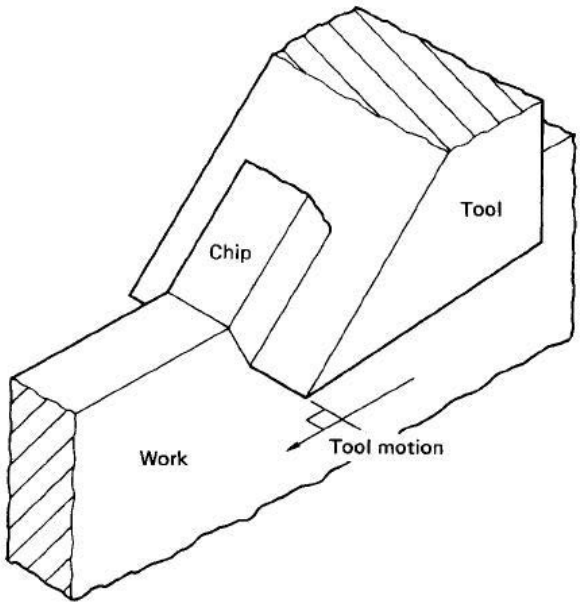

Figure 2-1. Orthogonal Machining [5]

In practice, cutting tools usually approach the work obliquely and have rake angles in both directions on the rake face, together with a nose radius at the end of the cutting edge. The direction in which the chip flows across the tool surface is determined by this complicated geometry. British Standard 1296: 1972 defines the angles on single-point

cutting tools in terms of the normal rake system, as shown in Figure 2-2, and is based on two coordinate rake angles. The back rake or cutting-edge inclination λ_s is measured parallel to the cutting edge in the vertical plane, and the normal rake γ_n is measured in a plane at right angles to the cutting edge and perpendicular to the rake face. The tool approach angle is ψ_r, and the horizontal clearance angle, or tool minor cutting edge angle, is $\kappa_{r'}$. In addition, the tool is relieved to give vertical clearance angles of about 5°.

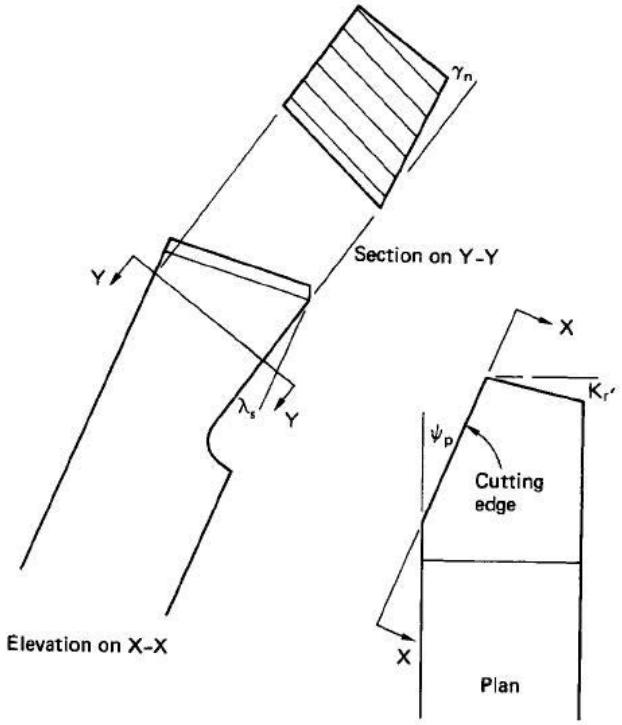

Figure 2-2. Angles in the normal rake system [5]

Other systems of tool nomenclature relate the rake angles to the coordinate axes of the tool shank, or to the cutting edge, measuring the angles in each case in the vertical plane. Although these systems are conceptually simpler, they are of little use in deducing the direction of chip flow. The British Standard relates to single-point tools, but it can be applied also to multi-point tools and is generally preferable to other systems.

2.3. Geometry of a Single-Edge Oblique Cutting Tool

Experimental work has shown that the direction in which the chip passes across the rake face of the tool can be expressed using Stabler's law [5]. This is best understood by referring to Figure 2-3, which shows an oblique shaping operation. This law simply states that $= \lambda_s$, where λ_s is the cutting-edge inclination, and γ is the angle measured on the rake face between the normal to the cutting edge and the direction of chip flow. In this example, the tool approach angle is zero, but the result is equally applicable for turning or face-milling cutters where the tool approach angle is generally not zero.

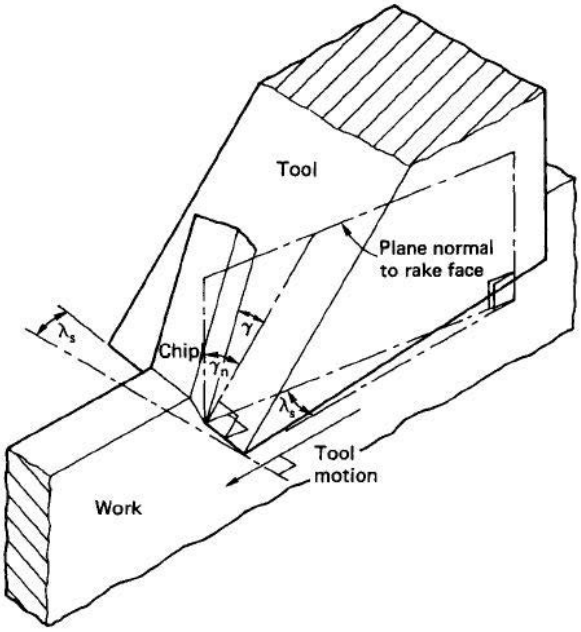

Figure 2-3. Oblique machining [5]

The chip geometry and the principal cutting force are determined by a rake angle measured in the direction of chip flow. This is known as the "effective rake" and is shown as β_e in Figure 2-4, which relates to a lathe tool, where [5]

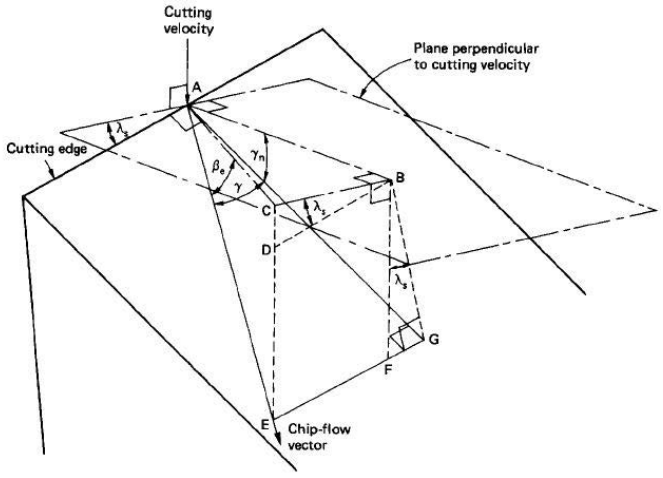

Figure 2-4. Angles in oblique machining [5]

$$\sin\beta_e = \sin\gamma_n + \sin^2\lambda_s - \sin\gamma_n \sin^2\lambda_s = \cos^2\lambda_s \sin\gamma_n + \sin^2\lambda_s \qquad (2\text{-}1)$$

If the normal rake is not specified, it can be calculated from the vertical rake angle's coordinate to the cutting edge, as shown in Figure 2-5, from which it can be seen that [5]

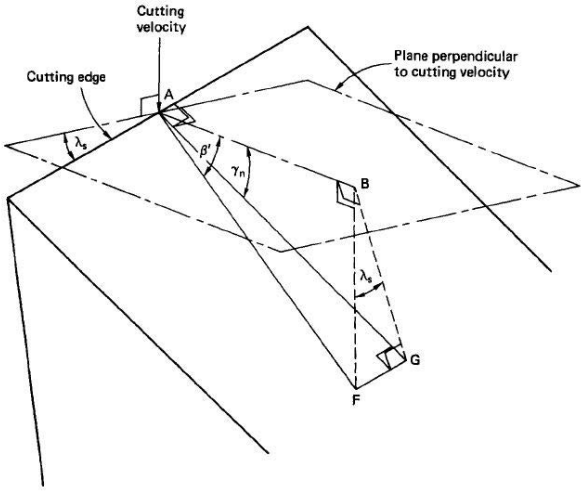

Figure 2-5. Back rake and normal rake relationship [5]

$$\tan\gamma_n = \tan\beta' \cos\lambda_s \qquad (2\text{-}2)$$

CHAPTER 3

CUTTING FORCES IN METAL CUTTING

3.1. Cutting Forces in Orthogonal Machining of Metals

The basic mechanics of chip-type machining processes are shown, in simplest two-dimensional form, in Figure 3-1 [6]. A tool with a certain rake angle a (positive, as shown) and relief angle moves along the surface of the workpiece at a depth of a_c. The material ahead of the tool is sheared continuously along the shear plane, which makes an angle of ∅ with the surface of the workpiece. This angle is called the shear angle and, together with the rake angle, determines the chip thickness a_c. The ratio of a_c to a_0 is called the cutting ratio r_c. The relationship between the shear angle, the rake angle, and the cutting ratio is given by equation (3-1) [6].

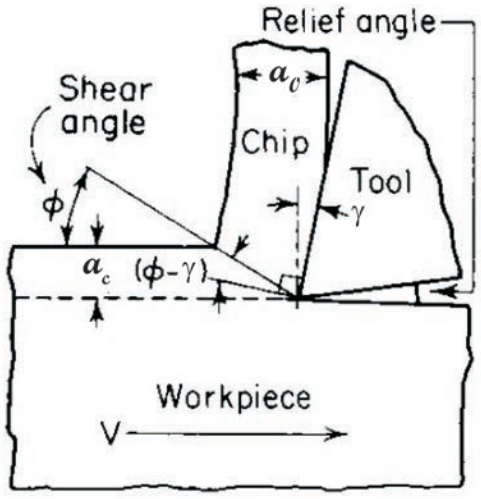

Figure 3-1. Basic mechanics of metal-cutting process [6]

$$\tan\phi = \frac{r_c \cos\gamma}{1 - r_c \sin\gamma} \tag{3-1}$$

It can readily be seen that the shear angle is important in that it controls the thickness of the chip. This, in turn, has great influence on cutting performance. The shear strain that the material undergoes is given by equation (3-2). Shear strains in metal cutting are usually less than 5.

$$\gamma = \cot\phi + \tan(\phi - \gamma) \tag{3-2}$$

Investigations have shown that the shear plane may be neither a plane nor a narrow zone, as assumed in simple analysis. Various formulas that define the shear angle in terms of such factors as the rake angle and the friction angle β have been developed. The forces acting on the cutting tool are shown in Figure 3-2. The resultant force R has two components, F_c and F_t. The cutting force F_c in the direction of tool travel determines the amount of work done in cutting. The thrust force F_t does not work but, together with F_c, produces deflections of the tool. The resultant force also has two components on the shear plane: F_s is the force required to shear the metal along the shear plane, and F_n is the normal force on this plane. Two other force components also exist on the face of the tool: the friction force F and the normal force N.

Whereas the cutting force F_c is always in the direction shown in Figure 3-2, the thrust force F_t may be in the opposite direction to that shown in Figure 3-2. This occurs when both the rake angle and the depth of cut are large, and friction is low.

From the geometry of Figure 3-2, the following relationships can be derived:

$$\mu = \frac{F_t + F_c \tan\gamma}{F_t + F_c \tan\gamma} \tag{3-3}$$

$$F = F_t \cos\gamma + F_c \sin\gamma \tag{3-4}$$

$$\tau_s = \frac{F_c \sin\phi \cos\phi - F_t \sin^2\phi}{A_0} \tag{3-5}$$

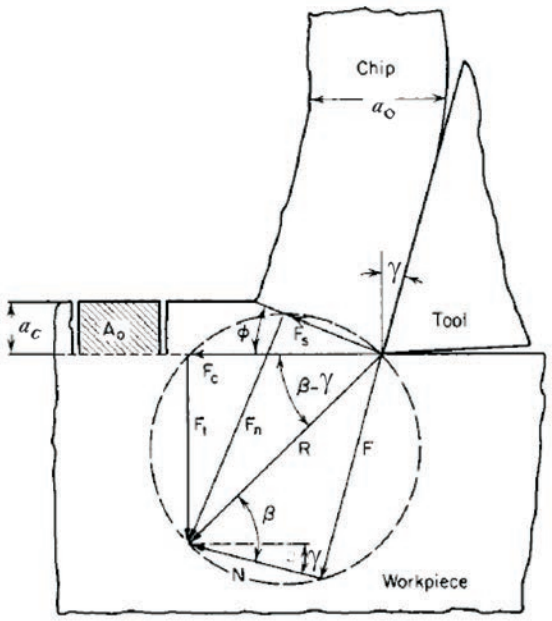

Figure 3-2. Force system in metal cutting process

where μ is the friction coefficient, F is the friction force along the tool, and τ_s is the shear stress in the shear plane.

3.2. Chip Thickness

Boothroyd [7] claims that the chip thickness a_0 in metal cutting is not only governed by the geometry of the cutting tool and the undeformed-chip thickness a_c but, as will be seen, is also affected by the frictional conditions existing at the chip-tool interface. Because the cutting process is affected by these factors, it differs fundamentally from other metal-deformation processes, where the final shape of the deformed material is determined by

the shape or setting of the tool used. In metal cutting, before predictions of cutting forces can be made, the chip thickness a_o must be determined in order for the geometry of the process to be known.

It has been shown in equation (3-1) that a knowledge of the shear angle ϕ allows a_0 to be estimated for a given set of cutting conditions. Experiments show that, ϕ and the cutting ratio r_c depend on the workpiece and tool materials and the cutting conditions. A number of attempts have been made in the past to establish a theoretical law that predicts the shear angle ϕ, and two of these attempts are considered below.

Although Piispanen attempted to solve this problem in 1937, Boothroyd [7] notes that the first complete analysis resulting in a so-called "shear-angle solution" was presented by Ernst and Merchant. The chip is assumed to behave as a rigid body in their analysis. It is assumed to be in equilibrium by the action of the forces transmitted across the chip-tool interface and across the shear plane. It is also supposed that the resultant tool force is transmitted across the chip-tool interface and there is no force acting on the tool edge or flank (i.e., the plowing force is zero).

The basis of Ernst and Merchant's theory was to minimize the cutting force for the shear angle ϕ. Since, for given cutting conditions, the work done in cutting is proportional to F_c, it was necessary to develop an expression for F_c in terms of ϕ and then to obtain the value of ϕ for which F_c is a minimum.

From Figure 3-2,

$$F_s = R\cos(\phi + \beta - \gamma) \tag{3-6}$$

$$F_s = \tau_s A_s = \frac{\tau_s A_0}{\sin\phi} \tag{3-7}$$

$$R = \frac{\tau_s A_0}{\sin\phi}\frac{1}{\cos(\phi+\beta-\gamma)} \tag{3-8}$$

Now by geometry

$$F_c = R\cos(\beta-\gamma) \tag{3-9}$$

Hence, from equations (3-8) and (3-9),

$$F_c = \frac{\tau_s A_0}{\sin\phi}\frac{\cos(\beta-\gamma)}{\cos(\phi+\beta-\gamma)} \tag{3-10}$$

Equation (3-10) may now be differentiated with respect to ϕ and equated to zero to find the value of ϕ for which F_c is a minimum. The required value is given by

$$2\phi+\beta-\gamma = \frac{\pi}{2} \tag{3-11}$$

Merchant found that this theory agreed well with experimental results obtained when cutting synthetic plastics; however, did not agree well enough with experimental results obtained for steel machined with a sintered carbide tool.

It should be noted that, in differentiating equation (3-10) with respect to ϕ, it was assumed that A_0, γ, and τ_s would be independent of ϕ. On reconsidering these assumptions, Merchant included in a new theory the relationship

$$\tau_s = \tau_{s_0} + k\sigma_s \tag{3-12}$$

which indicates that the shear strength of the material τ_s increases linearly with the increase in normal stress σ_s on the shear plane; at zero normal stress, τ_s is equal to τ_{s_0}.

It is assumed that k and τ_{s_0} are constants for the particular workpiece materials and that A_0 and γ are constants for the cutting operation. The resulting expression is

$$2\phi + \beta - \gamma = C \tag{3-13}$$

3.3. Oblique Machining Theory

The oblique cutting was first addressed by Merchant [8]. A few theories exist about the orthogonal cutting of metals in which the tool has zero inclination. However, complex tool geometries are widely used in industry where orthogonal cutting theories are not directly applicable. In oblique cutting, the cutting edge of the tool is not perpendicular to the cutting velocity. Most analyses assume that the mechanics of cutting in the normal plane are identical to that of orthogonal cutting; therefore, all of the force and velocity vectors are projected on the normal plane [9]. In the analysis of oblique cutting, the chip flow in the plane normal to the cutting edge acts as an orthogonal flow. The obliqueness of the cutting process is described by including a sliding process in the direction parallel to the cutting edge. Another approach to the oblique cutting analysis, described by Shaw et al. [10], considers the chip flow in the plane containing the cutting velocity and chip flow normal to this plane, but the normal stresses on the shear plane does not act in the direction parallel to this plane.

In Figure 3-3, ϕ_n is called the normal shear angle located between the shear and xy planes. The shear velocity lies on the shear plane but makes an oblique shear angle ϕ_i with the vector normal to the cutting edge on the normal plane. The sheared chip flow angle η is measured from a vector on the rake face and normal to the cutting edge [9]. The geometrical relation between the shear direction and chip flow is given by

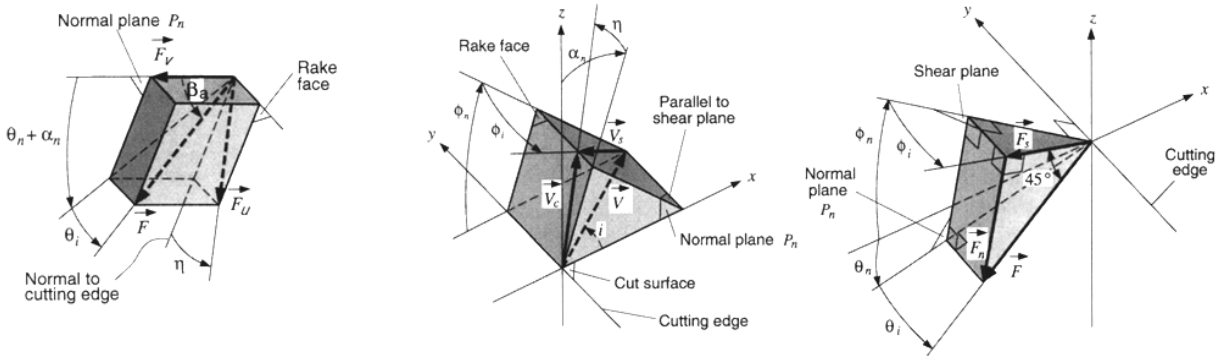

Figure 3-3. Force, velocity, and shear diagrams in oblique cutting [7]

$$\tan\eta = \frac{\tan i \cos(\phi_n - \alpha_n) - \cos(\alpha_n)\tan(\phi_i)}{\sin\phi_n} \tag{3-14}$$

Based on Armarego and Whitfield's [11] oblique model, the force components in the directions of cutting force (F_c), the thrust force (F_t), and the normal force (F_r) are given by

$$\begin{aligned} F_c &= bh\left[\frac{\tau_s}{\sin\phi_n}\frac{\cos(\beta_n - \alpha_n) + \tan i \tan\eta \sin\beta_n}{\sqrt{\cos^2(\phi_n + \beta_n - \alpha_n) + \tan^2\eta \sin^2\beta_n}}\right] \\ F_t &= bh\left[\frac{\tau_s}{\sin\phi_n \cos i}\frac{\sin(\beta_n - \alpha_n)}{\sqrt{\cos^2(\phi_n + \beta_n - \alpha_n) + \tan^2\eta \sin^2\beta_n}}\right] \\ F_r &= bh\left[\frac{\tau_s}{\sin\phi_n}\frac{\cos(\beta_n - \alpha_n)\tan i - \tan\eta \sin\beta_n}{\sqrt{\cos^2(\phi_n + \beta_n - \alpha_n) + \tan^2\eta \sin^2\beta_n}}\right] \end{aligned} \tag{3-15}$$

Therefore, the corresponding cutting constants are

$$K_{cc} = \frac{\tau_s}{\sin\phi_n} \frac{\cos(\beta_n - \alpha_n) + \tan i \tan\eta \sin\beta_n}{\sqrt{\cos^2(\phi_n + \beta_n - \alpha_n) + \tan^2\eta \sin^2\beta_n}}$$

$$K_{tc} = \frac{\tau_s}{\sin\phi_n \cos i} \frac{\sin(\beta_n - \alpha_n)}{\sqrt{\cos^2(\phi_n + \beta_n - \alpha_n) + \tan^2\eta \sin^2\beta_n}} \tag{3-16}$$

$$K_{rc} = \frac{\tau_s}{\sin\phi_n} \frac{\cos(\beta_n - \alpha_n)\tan i - \tan\eta \sin\beta_n}{\sqrt{\cos^2(\phi_n + \beta_n - \alpha_n) + \tan^2\eta \sin^2\beta_n}}$$

3.4. Review of the Machining of Fiber-Reinforced Polymers

Presently, almost every aerospace company is focusing on composites and developing products made with fiber-reinforced composite materials. There have been several stages of progress in FRP composites since the 1960s. The impact of the use of composite materials on jet-engine performance is substantial. Currently, with various metal alloys, thrust-to-weight ratios of 5 to 1 are achieved. Fiber-reinforced plastics and metals might lead to ratios as high as 16 to 1. Ultimately, with advanced graphite-fiber composites, thrust-to-weight ratios on the order of 40 to 1 appear possible. An eightfold increase in the performance index of thrust-to-weight ratio should lead to drastically pyramided weight savings in an entire aircraft due to substantially lessened structural support requirements [12]. This explains the dramatic increasing demand in FRP materials.

The processes used to make composite structures usually require that trimming and other secondary machining operations such as drilling and milling be performed prior to assembly of the components. Machining processes are required to manufacture accurate surfaces and holes to allow precision fitting of parts into an assembly. Since composite materials shrink during the curing stage, it is not practicable to place holes in the part

during the molding stage; therefore, milling, cutting, drilling, etc. are considered post-cure operations.

Modern composites are very abrasive and tough; therefore longer lasting and stronger tools are needed to be able to economically cut composites. A large database of machining information for various high-speed steel- and carbide-cutting tool materials exists for machining metal, wood, and some thermoplastic materials. However, much of this data cannot be directly applied to the machining of modern composites. Modern composites, like graphite-epoxy, aramid-epoxy, and carbon-carbon each have their own machining characteristics which may result in poor machined surface quality if ignored.

Composites are neither homogeneous nor isotropic; therefore, the machining characteristics depend on the tool path in relation to the direction of the reinforcing fibers. Metals or metal alloys have almost homogeneous properties throughout the workpiece, but each component in a composite material retains its individual properties [13]

3.4.1. Problems in Machining of Fiber-Reinforced Polymers

A few advantages in the machining of composites are as follows:

- The surface quality is improved, unless the part is directly in contact with the mold surface.
- Accuracy, in terms of dimensional and geometrical accuracy for assembly, increases.
- The majority of problems associated with part shrinkage and insert movement during the fabrication processes are eliminated.

On the other hand, the machining of composites poses several problems, one of which is associated with drilling. Drilling is a widely used process that is essential for assembling composite parts. Drilling of FRP may cause problems, which are different from

what occurs during drilling of metals. Delamination, fracture, break-out, and separation are some of the most common failures involved with drilling. Delamination (surface and sub-surface) is the most critical of these, as it reduces the structural integrity, results in poor assembly tolerance, adds a potential for long-term performance deterioration, and may occur at both the entrance and exit planes. Delamination can be prevented by finding optimal thrust force (minimum force above which delamination is initiated) [13]. In composite materials, particularly when they are being used in the aircraft industry, delamination plays a major role in the quality of the hole, since numerous microcracks in the drilled-hole surface can be detrimental. At lower altitudes, water vapor can penetrate into these microcracks, and then when the airplane reaches higher altitudes and thus freezing temperatures, the absorbed water vapor freezes, propagates into the microcracks, and deteriorates the fatigue properties [14].

In general, problems associated with traditional machining of FRPs include fiber pull-out, fiber push-down, delamination, burning, machined-surface fuzzing, and dust-like chips, all of which are health hazards [4].

3.4.2. Mechanics of Chip Formation in Unidirectional FRP

Machining of FRP depends on fiber and matrix properties, which describe how they respond to each machining process. In addition, the following factors affect the choice of specific process: type of machining operation, part geometry and size, finish and accuracy requirements, number of parts, diversity material construction of parts, availability of appropriate machine and cutting tools, availability of in-house technology, current machining practice, manufacturing schedule, capital requirements and justification for new equipment, and overall costs [15].

Chip formation in FRP differs from that which occurs in metals. In metals, the material shears and the chip forms and flows over the tool, based on the cutting angles and parameters; however, in the machining of composites, other mechanisms affect the cutting forces.

It has been found that chip formation in composites highly depends on fiber orientation and the angle of the cutting direction with the fibers.

The chip formation mechanisms in the orthogonal machining of unidirectional FRPs have been described in detail [16-19]. Here, orthogonal cutting was used to study the chip formation process. The most significant findings in these studies are summarized here. Three different cutting modes occur during orthogonal machining of FRPs and are described schematically in Figure 3-4.

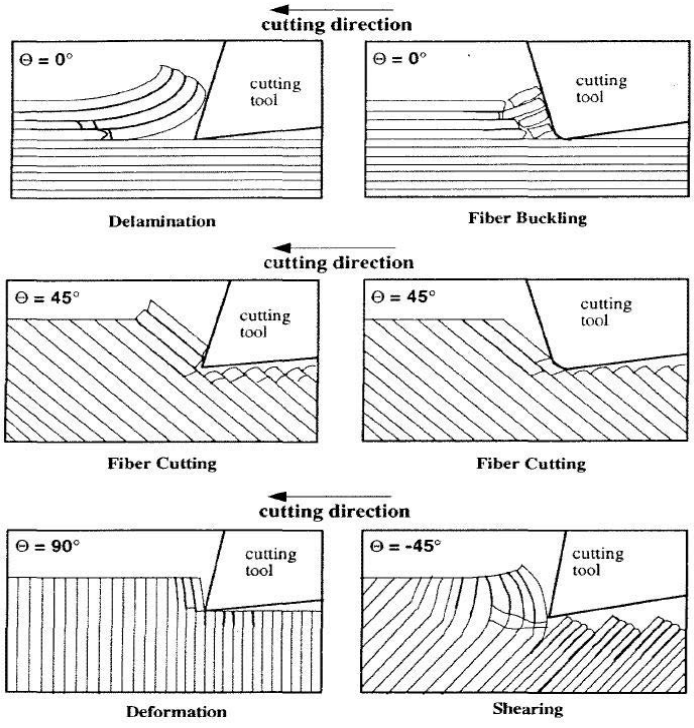

Figure 3-4. Cutting mechanisms in the orthogonal machining of graphite/epoxy [18]

Wang and his colleagues [18] used a charge-coupled device (CCD) camera with additional optical equipment necessary for obtaining a high-quality image. Figure 3-5 shows typical frames obtained by Wang et al. [18] during orthogonal trimming of 0°, 45°, 90°, and 135° unidirectional graphite/epoxy, respectively, and illustrates the dramatic change in chip formation with fiber orientation. They observed that when the cutting direction is along the fiber orientation, peel fracture begins from the tool point and propagates along the fiber/matrix interface, which resulted in small but distinct fragmented chips, as shown in Figure 3-5 (a). Depending on the depth of cut and tool rake angle, chip formation occurs with bending of the chip and fracture under cantilever loading, thus creating the broken-chip surface. They also observed that when trimming with 0° or negative rake angle tools, microbuckling was more prominent. At higher fiber orientations, small discontinuous dust chips were produced (Figure 3-5 (b)), and it was more difficult to observe and record the chip formation because of its small size. Figure 3-5 (d) shows the generation of delamination and macro fracture ahead of the tool in 135° fiber orientation. Another study by Koplev and his colleagues [16] showed that increasing the rake angle of the tool reduces the principal cutting force to some extent, while no definite trend was found on the thrust force. They also found that the cutting direction relative to the fiber orientation has a significant effect on the quality of the machined surface. Koplev et al. [16] also logged thrust and principal cutting forces as function of fiber orientation and cutting parameters. Then, cutting forces were correlated to the chip formation and tool wear to extract the fundamental relationships.

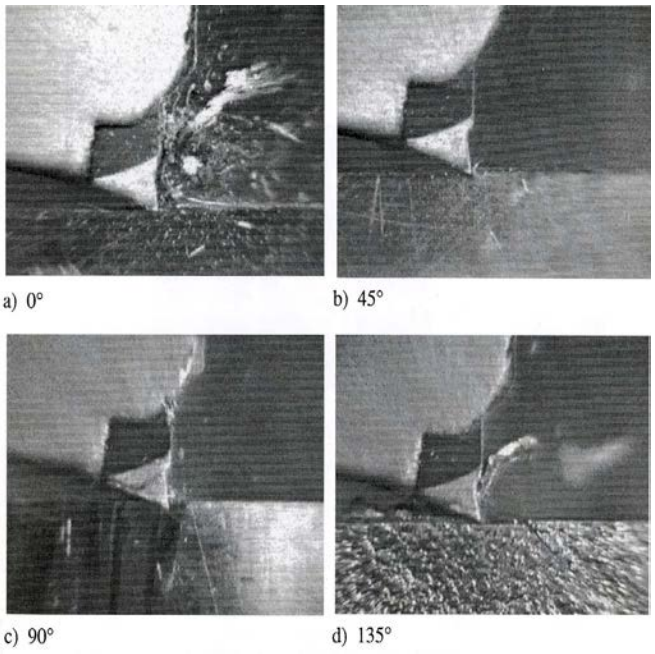

Figure 3-5. Chip formation during orthogonal trimming: (a) 0°, (b) 45°, (c) 90°, and (d) 135° [20]

In another study, Kaneeda [17] investigated the cutting mechanisms using a scanning electron microscope by cutting laminates parallel to the cutting direction. He found that the main chip formation mechanism is due to fiber-matrix debonding. He also claimed that the chip forms in two stages when the cutting tool has a positive rake angle. In the first stage, the cutting tool bends the work material layer, and in the second stage, fiber fracture occurs. When the tool rake angle is zero or negative and the cutting direction is parallel to the fiber orientation, the prominent cutting mechanism is fiber microbuckling. When the cutting direction makes an angle with the fiber orientation, the author observed that the primary chip formation mechanism is cutting the fibers. This cutting mode is also known as the fiber crushing mode, since extensive crushed fibers were observed on the machined surface.

It was also noted that the chip formation mechanism highly depends on the cutting direction, fiber orientation, and tool-tip geometry. The force fluctuation pattern expresses the chip formation mode [18]. When cutting parallel to the fiber orientation and with a positive rake angle, fiber-matrix debonding, or Mode I, occurs, followed by bending of the chips, sliding over the rake face, and finally fracture due to bending stress. With cutting tools having a negative rake angle and cutting parallel to the fiber direction, Mode II of chip formation occurs, which is fracture by buckling. According to the same study, in the machining of composites with a relative fiber orientation of $0° \leq \theta \leq 75°$, and with a positive rake angle, Mode II fracture occurs. Fibers fracture as the result of shear induced across the fiber axis. Fiber-matrix interfacial fracture and sliding along the fiber direction causes the chip to slide over the rake face. A Mode III fracture occurs in the machining of unidirectional composites with a relative fiber orientation greater than 90° in which consecutive planes of fiber-matrix interface are subjected to in-plane and out-of-plane type of shear.

Based on researchers' observations, there are similarities between the orthogonal cutting of ductile metals and unidirectional composites when the fiber orientation is $10° \leq \theta \leq 75°$, and these researchers have attempted to employ Merchant's well-known shear plane theory in the cutting of composites [21-23]. Merchant assumed that chip deformation occurs along a shear plane that forms at the tip of the cutting edge and continues upward to a point where the chip-free surface meets the workpiece-free surface, and the shear plane angle takes the value, which minimizes the energy consumed in the cutting [8].

The shear plane theory for composite materials is limited to a certain range of fiber orientation, which according to the literature is approximately $10° \leq \theta \leq 75°$; however, this approach would not apply to all possible fiber orientations in a composite structure. Another limitation is caused by interfacial shearing, which occurs along the fiber-matrix interface and forces the chips to slide up the rake face. In a way, this forces the shear plane angle to assume a value equal to the fiber-orientation angle, regardless of the minimum energy principal [22]. Results from this approach have shown reasonable agreement with experiments, only when the fiber orientation is $10° \leq \theta \leq 60°$.

Experiments show that machining conditions and tool point geometry have less influence on principal and thrust forces in a trimming operation. The cutting force increases as the fiber orientation approaches 75° , then it increases at a faster rate while trimming a 90° fiber orientation. With any further increase in the fiber orientation, the principal force decreases, with the sprouting decrease occurring at 150° and 165° orientations [18-19]. It was found that the thrust force during the cutting of composites was nearly always higher than the corresponding principal force, except when trimming material with fiber orientations of $\theta = 0°$ and $\theta \geq 90°$, which is different from what occurs in the conventional cutting of metals. Generally thrust force increased with fiber orientation up to 45° and then decreased to 90° [18-19]. Higher thrust-force generation is probably the result of deformation of fibers in the contact zone prior to fracture [18-19]. In addition, it was noted that cutting speed does not have a significant effect on the cutting forces; however, principal cutting force increased linearly with depth of cut.

In another study, Wang and Zhang [24] reported different deformation mechanisms in the cutting zone when the depth of cut and fiber orientation change. These deformation

mechanisms are schematically illustrated in Figure 3-6 using a model with a single fiber. When θ is less than 90°, as shown in Figure 3-6(a), regardless of depth of cut, the fiber is pushed by the tool (Force F_1) perpendicular to the fiber axis and toward the workpiece subsurface. In this case, there is minor fiber bending due to the matrix support behind the fiber. Also, as the tool moves toward the workpiece, a tensile force is acting along the fiber axis to cause the fiber to break in the neighborhood of the cutting zone. When the fiber orientation is greater than 90°, the situation becomes more complicated. When the depth of cut is less than $d.\sin(\theta - 90)$, where d is the fiber diameter, i.e., when the tool is cutting the very top surface of the fiber, as shown in Figure 3-6(b), the fiber is under compression. In this case, the fiber is unlikely to break when the surrounding epoxy, which is quite brittle, is fractured. The forces will be changed as the depth of cut becomes greater than $d.\sin(\theta - 90)$.

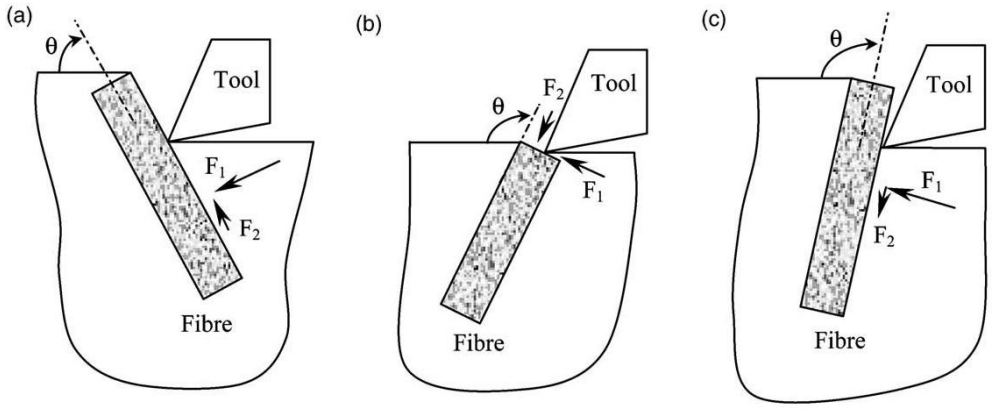

Figure 3-6. Schematic cutting models [24]

There have been several semi-empirical and statistical models to predict forces in the machining of composites. Therefore, it is important to review some of those models to understand their pros and cons.

3.4.3. Mechanics of Chip Formation in Machining Multidirectional Laminates

Wang et al. [18-19] studied orthogonal cutting mechanisms in the edge trimming of graphite/epoxy laminate with polycrystalline diamond tools. They observed discontinuous chips in the cutting of multidirectional composite plates as with the trimming of unidirectional panels. They claimed that the cutting mechanisms for 0° and 45° plies were the same as those in trimming unidirectional material. However, chip formation mechanisms in cutting 90° and −45° plies of multidirectional plies are different because of the support provided by adjacent plies. They found that chip formation and the machined surface quality in cutting unidirectional material highly depend on fiber orientation, with limited tool geometry influence. They also noted that increasing rake angle reduces the cutting forces while cutting material with 0° fiber orientation. With fiber orientation up to 90°, increasing the rake angle increased the thrust force. Smaller relief values caused higher thrust force values, and cutting the speed did not show a significant effect on the forces involved. An increase in the depth of cut linearly increased the forces [19]. They used a graphite/epoxy panel composed of 350I-6 resin and IM-6 fibers with 6 μm fiber diameter, 0.68 fiber volume fraction, and 200 μm ply thickness for the edge trimming experiments. The stacking sequence of the plies was $[45°/-45°/(0°/90°/45°/-45°)_2]_s$, where the stretching/bending coupling was eliminated because of the specific layup, which results in less chance for delamination and debonding. In contrast to the results obtained from the machining of a unidirectional laminate, the cutting force in the machining of multidirectional composite panels was found to be greater than the thrust force for all cutting conditions and tool geometries.

Using factorial design, Wang et al. developed empirical cutting force models for principal and thrust forces in terms of rake angle (γ), clearance angle (α), depth of cut (a_c), and cutting speed (V). Gauss-Newton search and nonlinear regression was employed to construct the generalized machining force models.

$$Force = C_0 + \sum_i C_i \,.X_i + \sum_i \sum_j C_{ij} \,.X_i.X_j \tag{3-17}$$

where $Force$ is the machining force, X_i are factors, and C_0, C_i, and C_{ij} are coefficients.

They performed an analysis of variance (ANOVA) on the average cutting force data and found the main effects on the principal cutting (F_c) and thrust (F_t). Equation (3-18) shows the empirical relations for principal and thrust forces. The correlation coefficients for the principal and thrust force models are 0.98 and 0.83, respectively.

$$\begin{aligned} F_c &= 10.68 - 11.67\gamma + 1584.53a_c + 0.99\gamma^2 - 7.10Va_c + 12.74\alpha a_c \\ F_t &= 147.27 - 4.92\alpha + 188.55a_c + 0.77\gamma^2 - 32.54\gamma a_c + 24.19\alpha a_c \end{aligned} \tag{3-18}$$

where γ is the rake angle, a_c is depth of cut, α clearance angle, and V is cutting velocity.

Analysis of the optimal principal cutting force showed that a rake angle (γ) of approximately 7° minimized the cutting force. Thrust force, however, increased with an increasing rake angle but decreased with an increasing clearance angle. They found that a tool with 6°~7° γ and 17° α angles minimizes the resultant forces. Increasing the clearance angle beyond 17° would result in lower thrust force and therefore resultant force, but this would reduce the tool life. They also found that the resultant cutting force in trimming multidirectional laminates is nearly equivalent to a summation of forces from independent

unidirectional laminates, based on a rule of mixtures approach; therefore, the superposition rule can be employed for this problem. This implies that edge trimming of multidirectional laminates will be dominated by the ply with the most rigid structural characteristics. To examine the dynamic effects and periodicity events in the chip formation process, the cutting force signatures and machined surface profiles were inspected [20]. For multidirectional laminate, spectral analysis showed that no periodicity existed, which is in agreement with the observation that the material behaved as an assembly of independent materials, each with its own chip formation characteristics [4].

3.5. Modeling of Chip Formation in Machining FRPs (Mechanics-Based)

A few mechanics-based models have been proposed for the cutting forces in both unidirectional and multidirectional composites, which are founded on the mechanics of cutting in metals. Some of them divide the cutting direction in two intervals and develop a model for each one separately. However, in most, a shear plane is considered to form, extending up from the tool cutting edge to the point of intersection of the free surfaces of the work and chip.

3.5.1. Bhatnagar Model

The first study on the orthogonal machining of fiber-reinforced polymers was done by Everstine and Rogers [25]. They used the continuum mechanics approach to develop a theory to predict minimum cutting force in the case of parallel (0°) fiber orientation. Bhatnagar et al. [22] developed a model for the cutting forces in orthogonal trimming of carbon fiber-reinforced polymers, based on Merchant's theory, for the power required for the removal of materials. They noted that the in-plane shear strength of material has a significant effect in determining cutting forces. The shear strength of FRP for different fiber

orientations can be measured by the Iosipescu shear test method [26]. Similar to the observations of Koplev et al. [16], Bhatnagar et al. [22] reported that the chip formation mechanism depends on relative fiber orientation. Figure 3-7 shows a schematic representation of fiber orientation in Bhatnagar et al.'s study of orthogonal cutting of unidirectional FRPs. They took the machining direction as the datum and expressed the fiber orientations with respect to θ as the only rotational parameter. θ varies from 0° to 180°. However, it is split into two broad groups: $0° - 90°$ as $+\theta$ and $180° - 90°$ as $-\theta$.

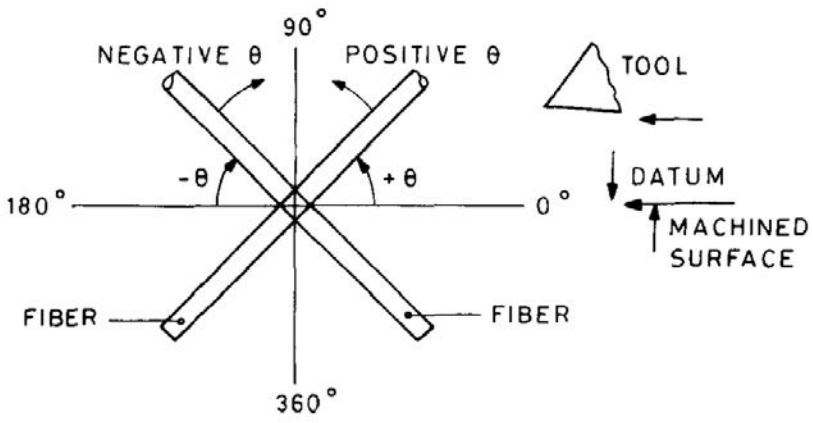

Figure 3-7. Schematic representation of the location of fiber orientation [22]

Using the Iosipescu shear tests, Bhatnagar et al. correlated the shear strength to the fiber orientation as

$$\tau(\theta) = 85.4285 - 2.2280\,\theta + 0.0300\,\theta^2 - 0.0001\,\theta^3 \qquad MPa \qquad (3\text{-}19)$$

In this approach, to model the $-\theta$ cutting forces, the following assumptions are made:

- The shear plane is along the fiber direction at which the matrix shears.

- The cutting forces depend on the in-plane shear strength of the respective fiber angle.
- Cutting and modeling are two-dimensional.
- The model is for $-\theta$ only when $90° \leq \theta \leq 180^\circ$ (Figure 3-8).

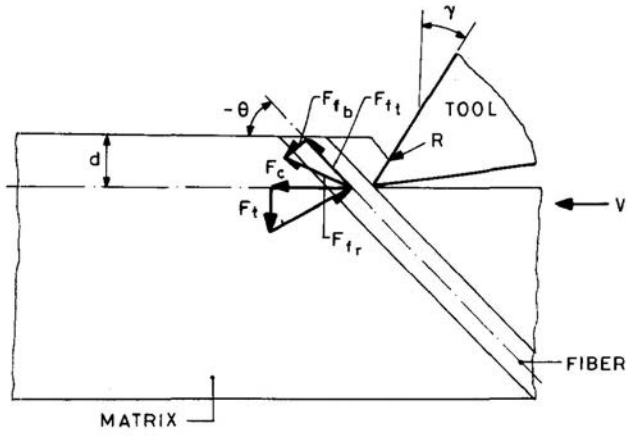

Figure 3-8. Schematic illustrating cutting mechanism for -θ UD-FRP [22]

The cutting and thrust forces are determined from the shear plane model as

$$F_c = \frac{\tau(\theta) a_c h}{\sin\theta} \frac{\cos(\beta - \gamma)}{\cos(\theta + \beta - \gamma)} \tag{3-20}$$

$$F_t = \frac{\tau(\theta) a_c h}{\sin(\theta)} \frac{\sin(\beta - \gamma)}{\cos(\theta + \beta - \gamma)} \tag{3-21}$$

where, β is the mean friction angle, and γ is the rake angle. The friction angle β can be calculated using the theory of metal machining as

$$\mu = \tan\beta = \frac{N}{F} = \frac{F_c \sin\gamma + F_t \cos\gamma}{F_c \cos\gamma - F_t \sin\gamma} \tag{3-22}$$

However, since it is difficult to obtain the mean friction angle value (β) for each specimen configuration, Bhatnagar et al. used the Merchant's circle to calculate the value of (β).

The experimental results for the cutting force showed a cyclic variation of the force ratio $^{N}/_{F}$ with the fiber angle. Figure 3-9 and Figure 3-10 show the variations of thrust and cutting forces for different fiber orientations and rake angles.

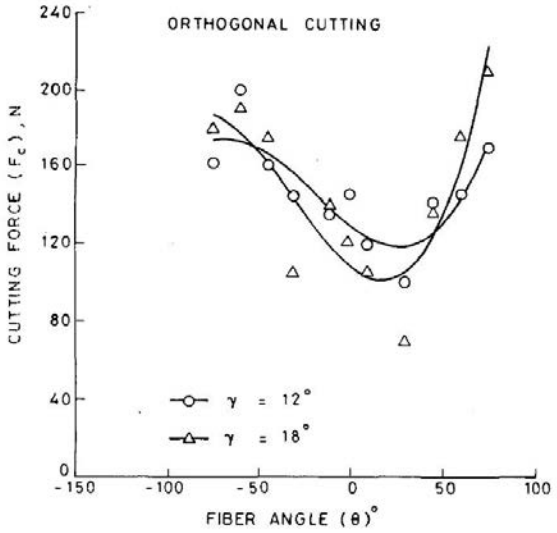

Figure 3-9. Variation of cutting force with fiber angle (θ) for different rake angles (γ) [22]

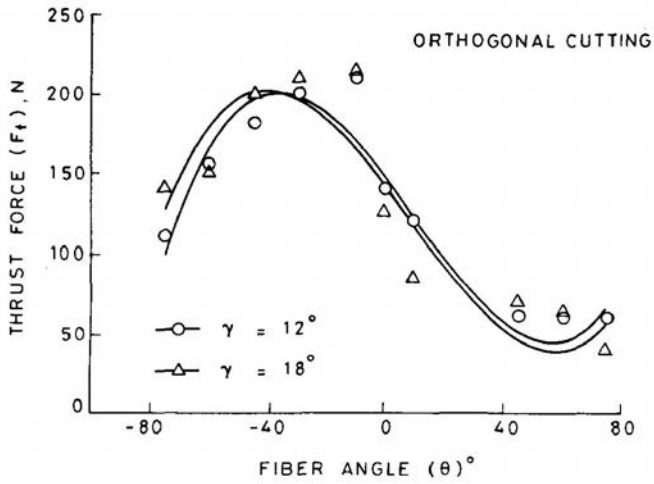

Figure 3-10. Variation of thrust force with fiber angle (θ) for different rake angles (γ) [22]

Bhatnagar et al. also observed from the force data that the friction conditions at the rake face depend on the fiber orientation, and the rake angle did not show a significant effect on friction at the tool-chip interface (Figure 3-11).

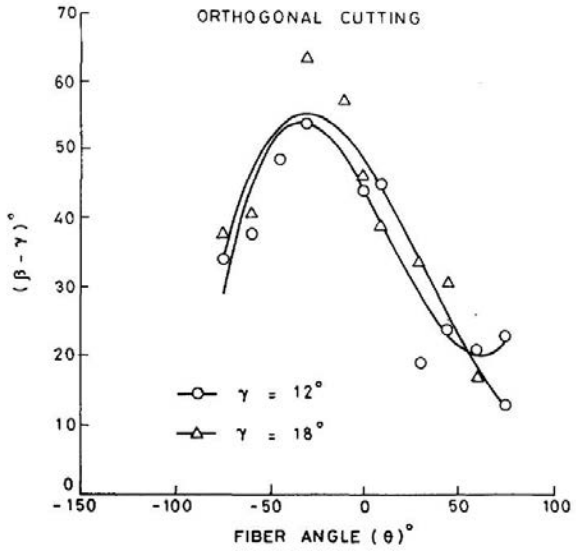

Figure 3-11. Variation of $(\beta - \gamma)$ with fiber angle (θ) from orthogonal cutting tests for different rake angles (γ) [22]

The requirement of determining in-plane shear strength by experiment, varying the friction angle, which in turn depends on the fiber orientation, the workpiece material, and tool geometry, is one of the drawbacks of this model. In addition, the model is not valid for the fiber orientations less than 90° since the chip formation mechanism is different. They also did not consider the fiber fracture as one of the factors affecting the machining forces. However, in this model the effect of fiber growth along the fiber orientation was considered. It is evident from the Figure 3-12 that the model is not valid for the higher positive fiber orientation angles, as the chip formation mechanism differs drastically [4].

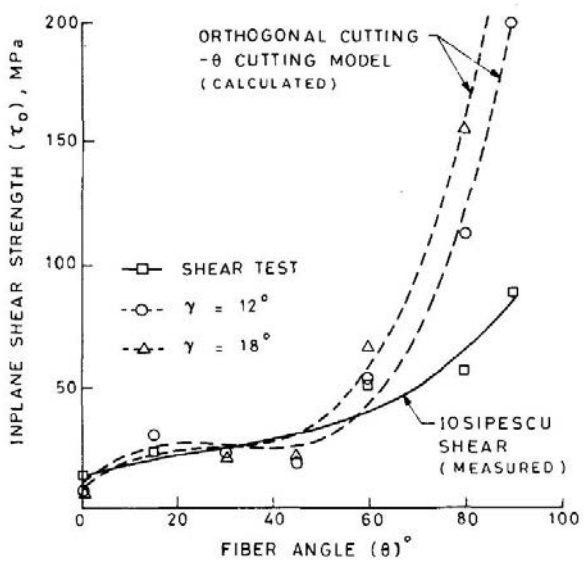

Figure 3-12. Variation of inplane shear strength with fiber angle (θ) from orthogonal cutting tests and Iosipescu shear tests [22]

3.5.2. Finite Element Models

Arola and Ramulu [27] from the visual observation of experiments realized that the removal of material in the machining of composites occurred through a series of fracture events and was clearly discontinuous. To simulate the fracture and nodal debonding, they did not use cohesive elements in the finite element modeling. Instead, they used a stress criterion to model the fracture in machining FRP. Chip formation during the primary fracture, as shown in Figure 3-13, was achieved using a nodal debond criterion on a plane corresponding to the trim plane. In each fiber angle, the trim plane ahead of the tool tip was double-noded. Debonding was permitted for each pair of nodes when the nodal stress approached either a predefined maximum normal or shear stress. The authors found that the chip formation in orthogonal trimming of FRP depends on fiber orientation and tool geometry. The cutting forces obtained from experiments agreed well with their finite

element model; however, the variation of thrust force was incorrect. The reason for the inconsistency of the numerical results with the measurement is the difficulty in properly defining the fracture plane. In addition, predictions for the principal cutting forces using Tsai-Hill criterion are more in agreement with the experimental measurements than the predictions using maximum stress criterion.

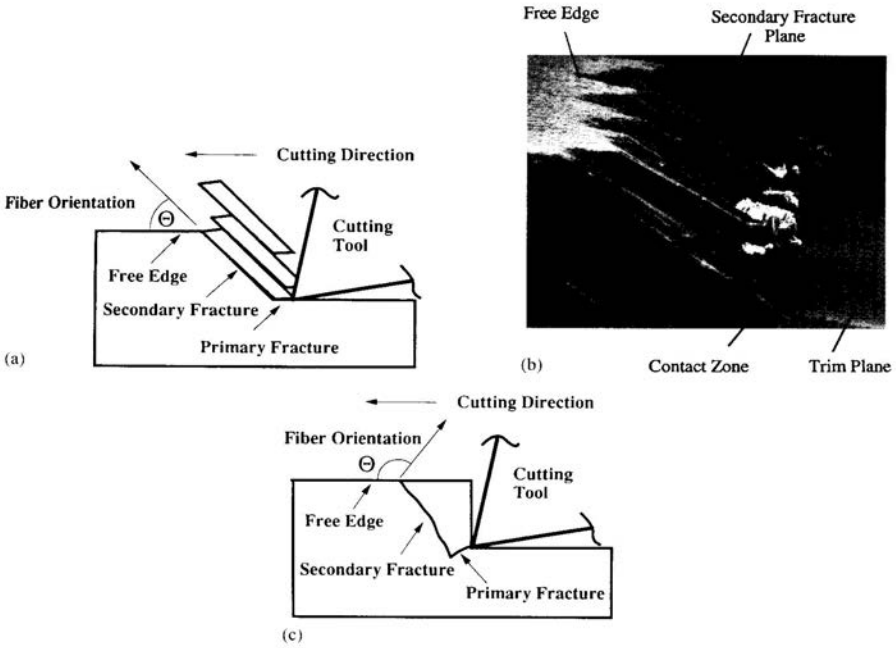

Figure 3-13. Chip formation in orthogonal trimming in unidirectional FRPs: (a); (b) chip formation fracture planes of 30 unidirectional graphite/epoxy; (c) [27]

Bhatnagar et al. [28] used a numerical method and experiments to predict the cutting forces, contact pressure, and frictional shear at the tool-fiber interface in the machining of unidirectional glass fiber-reinforced polymer (UD-GFRP). Both the thrust and cutting forces of their numerical simulation matched well with the experimental results.

Mahdi and Zhang [29] used the fiber and matrix mechanical properties to obtain an equivalent homogeneous anisotropic material (EHAM) to predict the cutting force. In

addition, they used Tsai-Hill (or maximum work) criterion to simulate the material separation and therefore chip formation. This criterion for a plane-stress condition is

$$\frac{\sigma_{11}^2}{X_1^2} - \frac{\sigma_{11}\sigma_{22}}{X_1^2} + \frac{\sigma_{22}^2}{X_2^2} + \frac{\sigma_{12}^2}{S^2} \geq 1 \qquad (3\text{-}23)$$

where X_1 and X_2 are the tensile (or compressive) failure strength in the 1 and 2 directions, and S is the shear failure strength. The model predictions agreed with the experimental results. They also showed that the tool rake angle, varying from 0° to 20°, does not have a significant effect on the cutting force.

Several numerical and analytical models for cutting and trimming of composites have been proposed since the introduction of composites, but each of them works for a certain range of fiber orientation.

3.5.3. Non-Traditional Machining

3.5.3.1. Abrasive-Waterjet Machining

Hashish [30] has presented extensive research on the machining of composites with abrasive waterjets. He studied metal matrix composites (such as magnesium boron carbide and aluminum silicon carbide), laminated thermoset composites (such as carbon-epoxy resins, fiber-reinforced thermoplastic composites), and ceramic composites (such as silicon carbide and aluminum oxide systems) in different machining processes, including linear cutting, milling, turning, and drilling of small diameter holes. He claimed that machining with an abrasive waterjet is significantly more dependent on the matrix material than the reinforcement particulate or whisker material. He also found that abrasive-waterjet machining is faster in removing material compared to many composite machining

techniques; however, dimensional accuracy is still low and needs further work. In addition, excessive water pressure can cause the water to penetrate between fibers and cause the laminates to separate [31]. Figure 3-14 shows a schematic view of an abrasive-waterjet nozzle.

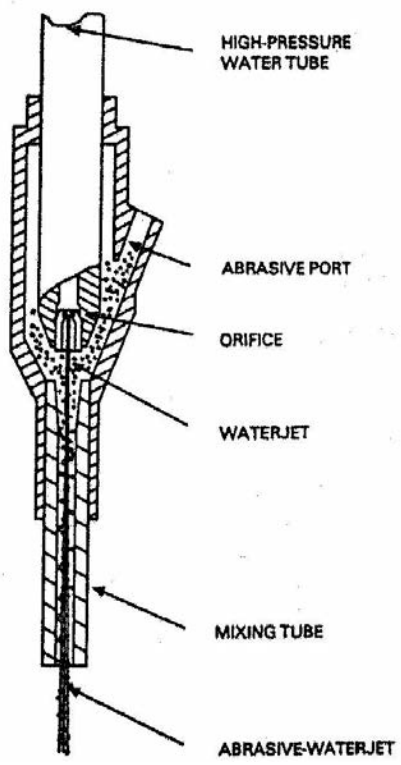

Figure 3-14. Abrasive-waterjet nozzle [30]

As is known, delamination is a major problem in the machining of composites. Several researchers have investigated the quality and machinability of composites using waterjet and abrasive-waterjet methods [30, 32-38]. It was found that crack tips are generated by the shock wave impact of the waterjet at the primary cutting stage, while delamination along the fiber-matrix interface is a result of water penetration into the crack tips that creates water-wedging and the embedment of abrasives [35]. These delamination

mechanisms are shown in Figure 3-15. Figure 3-16 shows an abrasive-waterjet cutting system.

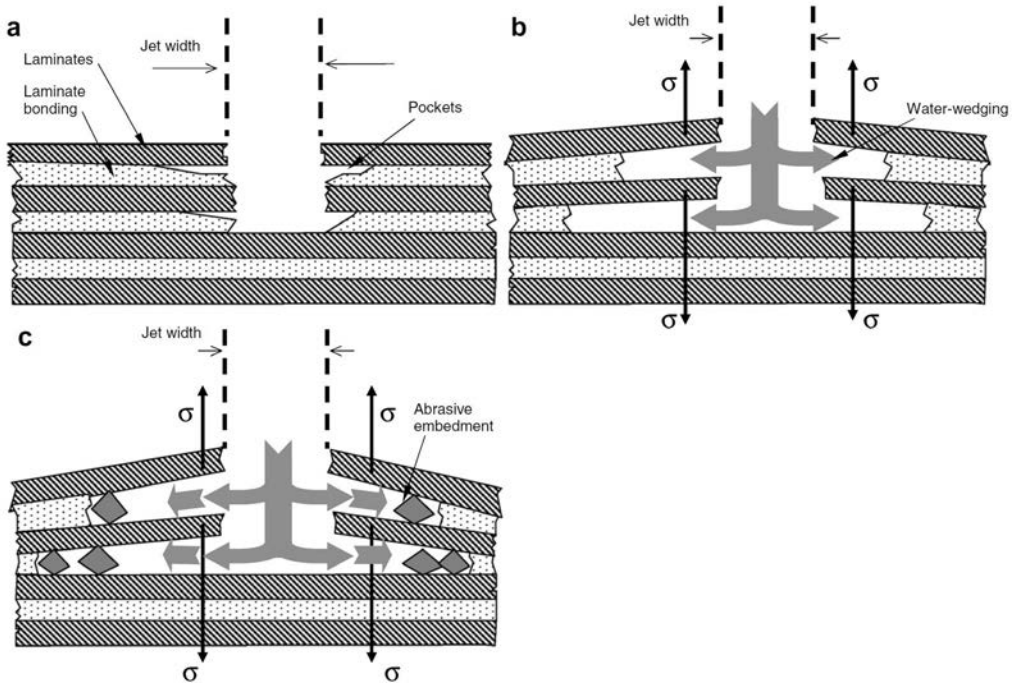

Figure 3-15. Mechanisms of delamination: (a) fracture initiation, (b) water-wedging and (c) abrasive embedment [35]

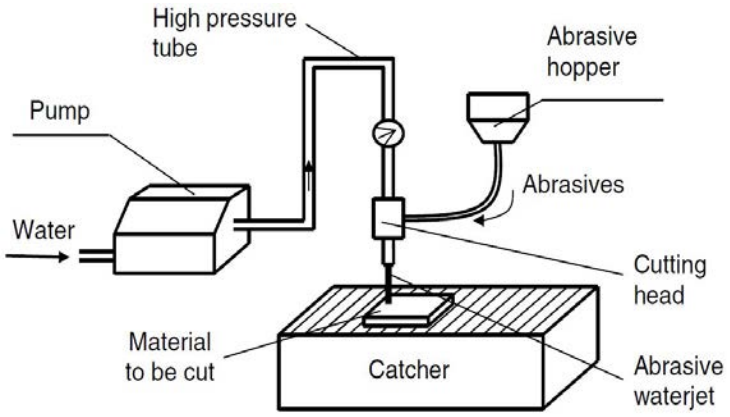

Figure 3-16. Schematic of AWJ cutting system [35]

Shanmugam et al. [35] also compared the quality of the cutting with a pure waterjet, an abrasive waterjet, and a delayed abrasive waterjet. They found that the cutting quality and performance using abrasive waterjet without any delay in the abrasive mass flow is much better comparing to pure waterjet and waterjet with delayed abrasive flow. Figure 3-17 compares the quality of the cuttings performed with waterjet and abrasive waterjet methods.

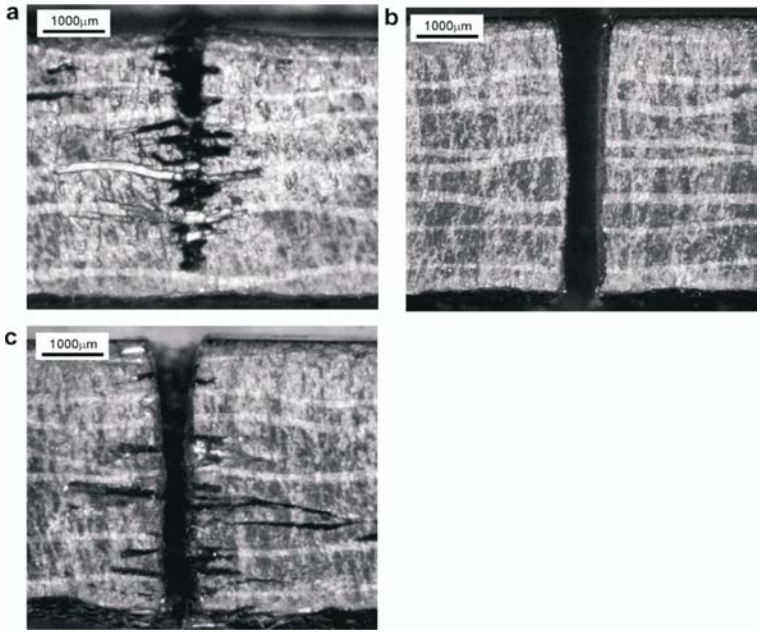

Figure 3-17. Cross sections of workpieces performed by cutting at P = 210 MPa: (a) using pure waterjet, (b) using AWJ at $\dot{m} = 3\ g/s$, and (c) using AWJ at $m = \dot{3}\ g/s$ and particles introduced after a delay time of 3 s [35]

3.5.3.2. Laser Cutting

Laser trimming cured graphite/epoxy laminates with an acceptable heat-affected zone (HAZ) has proven to be extremely difficult. The carbon fibers have a high thermal conductivity, and the material fibers and matrix do not simultaneously reach their vaporization temperatures [39].

Currently, there are two industrial lasers being used for cutting composites, $Nd{:}YAG$ and CO_2. The $Nd{:}YAG$ laser efficiently cuts metallic composites since its wavelength is effectively absorbed by most metallic compounds; however, if used for cutting organic materials, it can decompose the organic resin, since its wavelength is not effectively absorbed by this type of material. The CO_2 laser operates at a wavelength that is effectively absorbed by most organic materials.

Mello [31] successfully cut Kevlar/graphite/epoxy and Kevlar/epoxy composites with a three-axis laser work station. The cut exhibited no signs of fraying, and the edge was smooth. Cutting tests using high-quality electrically pulsed $Nd{:}YAG$ lasers have yielded smaller HAZ results compared to cuts with a continuous wave CO_2 laser. A smaller HAZ is the result of using Q-switching modulation in an electrically pulsed beam. The key to effectively trimming graphite/epoxy laminates with an acceptable HAZ is to minimize the amount of heat added to the cut edge. The combined use of high-beam quality $Nd{:}YAG$ lasers and pulsing techniques appears to be of benefit [39].

Laser processing of non-metallic composites has proven to be a practical approach as a machining method; however, several precautions need to be taken. Hazardous fumes can be generated once the laser interacts with the workpiece, especially in the presence of assist gas.

CHAPTER 4

FORCE PREDICTION MODEL FOR CUTTING UNIDIRECTIONAL FIBER-REINFORCED PLASTICS

Zhang et al. proposed a mechanics model for orthogonal machining of unidirectional composites [23]. They observed that three distinct deformation regions exist in the cutting zone, as shown in Figure 4-1, when the fiber orientation θ varies between $0^{\circ}$and 90°. The first region is in front of the rake face, resulting in a chip, which is called a chipping region or Region 1. Fracture occurs at the cross-sections of the fibers and along the fiber-matrix interfaces. The chipping along an overall shear plane, as shown in Figure 4-1, is the result of a zigzag cracking of the fibers perpendicular to the fiber axes and the fiber-matrix interface debonding in the fiber-axis direction. The second distinct deformation region takes place under the tool nose, where the nose pushes down the workpiece material. For convenience, it is called the pressing region or Region 2. The last region, called the bouncing region or Region 3, involves primarily the bouncing back of the workpiece material, which happens under the clearance face of the cutting tool. When the fiber orientation is larger than 90°, more deformation mechanisms take place. As illustrated in Figure 4-2, both the fiber-matrix debonding and fiber bending contribute significantly to the deformation and removal of material. Because of the debonding, the depth of the subsurface damage becomes much greater, as shown in Figure 4-3. The bending of the fibers makes the breakage point of a fiber vary with the movement of the cutting tool, and as demonstrated in Figure 4-3, the quality of a machined surface becomes much poorer.

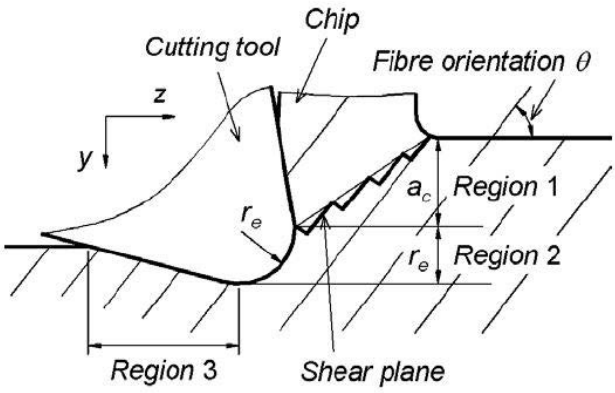

Figure 4-1. Definitions of cutting variables and deformation zones when fiber orientation is smaller than 90° [23]

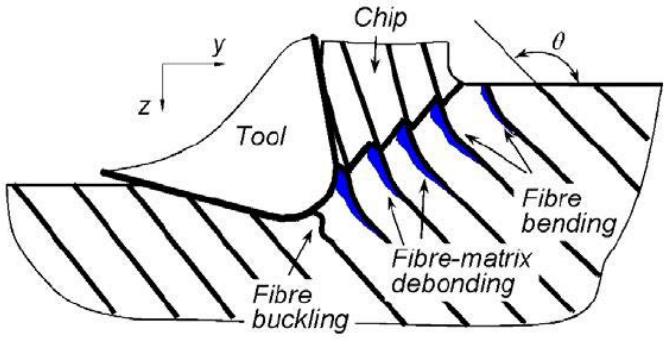

Figure 4-2. Fiber-bending and fiber-matrix debonding during cutting when fiber orientation is larger than 90° [23]

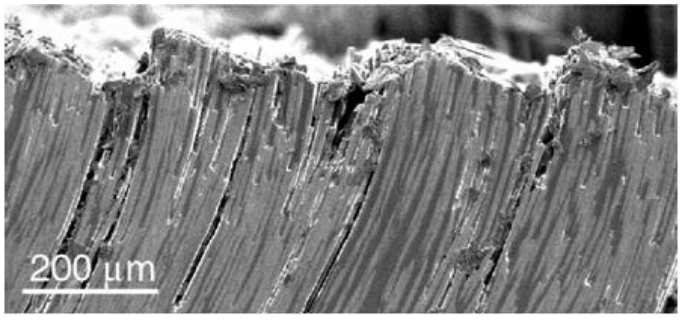

Figure 4-3. Effect of fibre orientation (F593 panels); microstructure in the subsurface (fibre orientation = 120°, depth of cut = 0.100mm, rake angle = 0°) [23]

4.1. Modeling of Orthogonal Cutting of Unidirectional Fibers

Based on an understanding of the above, the mechanics of modeling of cutting need to be conducted differently when $\theta \leq 90^{\circ}$ or when $\theta > 90^{\circ}$.

4.1.1. Modeling of orthogonal cutting of unidirectional fibers for $\theta \leq 90^{\circ}$

4.1.1.1. Region 1 – Chipping

Zhang et al. [23] shows the total shear force F_s in Region 1 can be calculated by

$$F_s = \frac{\tau_1 . h . a_c}{\frac{\tau_1}{\tau_2}\cos(\theta - \phi)\sin\theta - \sin(\theta - \phi)\cos\theta} \tag{4-1}$$

and F_{y_1} and F_{z_1}, which are thrust and cutting forces, respectively, in Region 1 can be calculated using the following equations:

$$\begin{cases} F_{z_1} = \tau_1 . h . a_c . \dfrac{\sin\phi\tan(\phi + \beta - \gamma) + \cos\phi}{\frac{\tau_1}{\tau_2}\cos(\theta - \phi)\sin\theta - \sin(\theta - \phi)\cos\theta} \\ F_{y_1} = \tau_1 . h . a_c . \dfrac{\cos\phi\tan(\phi + \beta - \gamma) + \cos\phi}{\frac{\tau_1}{\tau_2}\cos(\theta - \phi)\sin\theta - \sin(\theta - \phi)\cos\theta} \end{cases} \tag{4-2}$$

To calculate the forces using equation (4-2), ϕ needs to be determined. According to the general cutting mechanics

$$\tan\phi = \frac{r_c\cos\gamma}{1 - r_c\sin\gamma} \tag{4-3}$$

where γ is the rake angle of the tool and

$$r_c = \frac{a_c}{a_0} \tag{4-4}$$

where a_0 is the chip thickness and r_c is the cutting ratio. Because an FRP during cutting behaves like a typical brittle material [40], it is reasonable to let $r_c = 1$. Therefore,

$$\phi \approx \tan^{-1}\left(\frac{\cos\gamma}{1-\sin\gamma}\right) \tag{4-5}$$

4.1.1.2. Region 2 – Pressing

The deformation in Region 2 is caused by the tool nose, which can be viewed as the deformation under a cylindrical indenter, as shown in Figure 4-4 as Wang et al. [23] proposed.

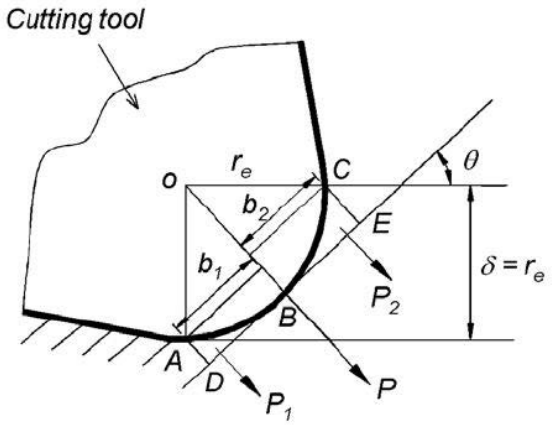

Figure 4-4. Contact between tool nose and the workpiece material in Region 2 [23]

Wang et al. shows that the total cutting forces in Region 2 become

$$\begin{cases} F_{y_2} = P_{real}\,(\cos\theta - \mu\sin\theta) \\ F_{z_2} = P_{real}\,(\sin\theta + \mu\cos\theta) \end{cases} \tag{4-6}$$

$$P_{real} = K.P \tag{4-7}$$

where P_{real} is the real resultant force in Region 2, where the coefficient K is a function of fiber orientation, i.e., $K = f(\theta)$, to be determined by the experiment.

P can be calculated using the following equations [41]:

$$\begin{cases} P_1 = \frac{1}{2}\frac{b_1^2.\pi.E^*.h}{4.r_e} \\ P_2 = \frac{1}{2}\frac{b_2^2.\pi.E^*.h}{4.r_e} \end{cases} \tag{4-8}$$

where

$$\begin{cases} b_1 = r_e \sin\theta \\ b_2 = r_e \cos\theta \end{cases} \tag{4-9}$$

in which

$$E^* = \frac{E}{1-\nu^2} \tag{4-10}$$

$$P = P_1 + P_2 \tag{4-11}$$

4.1.1.3. Region 3 – Bouncing

The contact force between the clearance face and the workpiece material is caused by the bouncing back of the workpiece material in this region [23].

The cutting forces in the “Bouncing Region” (Region 3) are

$$\begin{cases} F_{y_3} = \frac{1}{2}.r_e.E_3.H.(1-\mu\cos\alpha\sin\alpha) \\ F_{z_3} = \frac{1}{2}.r_e.E_3.H\cos^2\alpha \end{cases} \quad (4\text{-}12)$$

One can use contact mechanics between a wedge and a half-space to calculate the normal contact force N, shown in Figure 4-5 [42]:

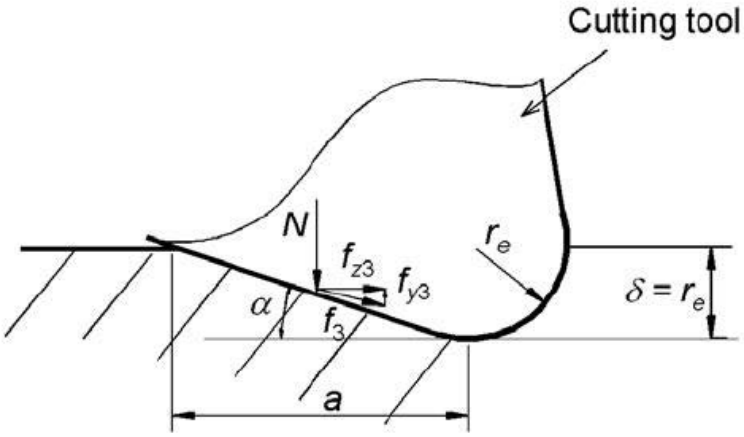

Figure 4-5. Contact in Region 3

$$N = \frac{1}{2}.a.E_3.\tan\alpha.h$$
$$a = \frac{r_e}{\tan\alpha} \quad (4\text{-}13)$$

4.1.1.4. Total Cutting Forces

The total machining forces, F_z and F_y, are the summation of the corresponding components from the above three regions.

$$\begin{cases} F_y = F_{y_1} + F_{y_2} + F_{y_3} \\ F_z = F_{z_1} + F_{z_2} + F_{z_3} \end{cases} \quad (4\text{-}14)$$

4.1.2. Modeling of Orthogonal Cutting of Unidirectional Fibers for $\theta > 90^{\circ}$

When the fiber orientation is greater than 90°, a cutting involves other deformation mechanisms, as shown in Figure 4-2. Two methods will be presented in this study, the finite element method (FEM) and the analytical method.

4.1.2.1. Finite Element Modeling of Debonding

Finite element analysis (FEA) was conducted using a commercial package, Abaqus/Explicit, to measure the fiber-matrix debonding length. The material was modeled at the microscopic level to better understand the delamination mechanism. Fiber and matrix materials were modeled separately, bonded together using cohesive elements. Abaqus provides a type of element, which is primarily intended for bonded interfaces where the thickness is negligibly small. The constitutive response of this element can be directly expressed in terms of traction versus separation. In the case of finite thickness of the cohesive element and availability of the macroscopic properties of the adhesive material, it may be more appropriate to model the response using the conventional material model. For the purpose of this study, the cohesive element for the interface with the traction-separation response was used. Cohesive behavior, defined in terms of the traction-separation law, has several advantages:

- Can be used to model the delamination at interfaces in composites directly in terms of traction versus separation.

- Allows specification of material data, such as the fracture energy as a function of the ratio of normal to shear deformation (mode mix) at the interface.
- Assumes a linear elastic traction-separation law prior to damage.
- Assumes that failure of the elements is characterized by progressive degradation of the material stiffness, which is driven by a damage process.
- Allows multiple damage mechanisms.
- Can be used with a user subroutine UMAT in Abaqus/Standard or VUMAT in Abaqus/Explicit to specify user-defined traction-separation laws.

4.1.2.1.1. Fiber Material Modeling

Carbon fiber shows orthotropic properties [43]; however, in this study, to compare the analytical solution with the FEM model, an isotropic model was used to model the carbon fibers. The summary of the properties of an isotropic carbon fiber is available in Table 4-1 [43].

TABLE 4-1

CARBON FIBER MECHANICAL PROPERTIES

Diameter, μm	6.9
Axial modulus of elasticity (E_{11}), GPa	186
Axial tensile strength, GPa	3.6
Axial shear modulus, GPa	76.9
Flexural strength, GPa	4.0
Axial Poisson's ratio	0.3

Linear elasticity in an orthotropic material can be defined by providing the nine independent elastic stiffness parameters, as functions of temperature and other predefined fields, if necessary. In this case, the stress-strain relations are of the form [44]

$$\begin{Bmatrix}\sigma_{11}\\ \sigma_{22}\\ \sigma_{33}\\ \sigma_{12}\\ \sigma_{13}\\ \sigma_{23}\end{Bmatrix} = \begin{bmatrix} D_{1111} & D_{1122} & D_{1133} & 0 & 0 & 0 \\ & D_{2222} & D_{2233} & 0 & 0 & 0 \\ & & D_{3333} & 0 & 0 & 0 \\ & & & D_{1212} & 0 & 0 \\ & sym & & & D_{1313} & 0 \\ & & & & & D_{2323} \end{bmatrix} \begin{Bmatrix}\epsilon_{11}\\ \epsilon_{11}\\ \epsilon_{11}\\ \epsilon_{11}\\ \epsilon_{11}\\ \epsilon_{11}\end{Bmatrix} \tag{4-15}$$

where the engineering constants are calculated using the following equations [44]:

$$\begin{aligned} D_{1111} &= E_1(1-\nu_{23}\nu_{32})\Upsilon \\ D_{2222} &= E_2(1-\nu_{13}\nu_{31})\Upsilon \\ D_{3333} &= E_3(1-\nu_{12}\nu_{21})\Upsilon \\ D_{1122} &= E_1(\nu_{21}+\nu_{31}\nu_{23})\Upsilon = E_2(\nu_{12}+\nu_{32}\nu_{13})\Upsilon \\ D_{1133} &= E_1(\nu_{31}+\nu_{21}\nu_{32})\Upsilon = E_3(\nu_{13}+\nu_{12}\nu_{23})\Upsilon \\ D_{2233} &= E_2(\nu_{32}-\nu_{12}\nu_{31})\Upsilon = E_3(\nu_{23}+\nu_{21}\nu_{13})\Upsilon \\ D_{1212} &= G_{12} \\ D_{1313} &= G_{13} \\ D_{2323} &= G_{23} \end{aligned} \tag{4-16}$$

where $$\Upsilon = \frac{1}{1-\nu_{12}\nu_{21}-\nu_{23}\nu_{32}-\nu_{31}\nu_{13}-2\nu_{21}\nu_{32}\nu_{13}} \tag{4-17}$$

When the material stiffness parameters (the D_{ijkl}) are given directly, Abaqus imposes the constraint $\sigma_{33} = 0$ for the plane stress case to reduce the material's stiffness matrix as required.

4.1.2.1.1.1. Stress-Based Failure Theories

Several stress-based failure theories for an orthotropic material that can be used to model fiber failure are available. The input to these theories are X_t and X_c, which are tensile and compressive stress limits in the 1-direction, Y_t and Y_c, in the 2-direction, and shear strength S in the $x - y$ plane.

Maximum Stress Theory

Maximum Stress Theory criterion states that the material will not fail if [44]

$$I_F = \max\left(\frac{\sigma_{11}}{X}, \frac{\sigma_{22}}{Y}, \left|\frac{\sigma_{12}}{S}\right|\right) < 1.0 \tag{4-18}$$

In this criterion, if $\sigma_{11} > 0, X = X_t$; otherwise, $X = X_c$. If $\sigma_{22} > 0, Y = Y_t$; otherwise, $Y = Y_c$.

Tsai-Hill Theory

In the Tsai-Hill Theory [44], X and Y take their values in the same way as described in the "Maximum Stress Theory."

$$I_F = \frac{\sigma_{11}^2}{X^2} - \frac{\sigma_{11}\sigma_{22}}{X^2} + \frac{\sigma_{22}^2}{Y^2} + \frac{\sigma_{12}^2}{S^2} < 1.0 \tag{4-19}$$

Tsai-Wu Theory

The Tsai-Wu Theory failure criterion requires that [44]

$$I_F = F_1\sigma_{11} + F_2\sigma_{22} + F_{11}\sigma_{11}^2 + F_{22}\sigma_{22}^2 + F_{66}\sigma_{12}^2 + 2F_{12\sigma_{11}\sigma_{22}} < 1.0$$

$$F_1 = \frac{1}{X_t} + \frac{1}{X_c}, F_2 = \frac{1}{Y_t} + \frac{1}{Y_c}, F_{11} = -\frac{1}{X_t X_c}, F_{22} = -\frac{1}{Y_t Y_c}, F_{66} = \frac{1}{S^2} \quad (4\text{-}20)$$

$$F_{12} = 1/2\sigma_{biax}^2 [1 - \left(\frac{1}{X_t} + \frac{1}{X_c} + \frac{1}{Y_t} + \frac{1}{Y_c}\right)\sigma_{biax} + \left(\frac{1}{X_t X_c} + \frac{1}{Y_t Y_c}\right)\sigma_{biax}^2$$

otherwise

$$F_{12} = f^*\sqrt{F_{11}F_{22}} \quad (4\text{-}21)$$

where $-1.0 \leq f^* \leq 1.0$. the default value of f^* is zero.

Azzi-Tsai-Hill Theory

The Azzi-Tsai-Hill Theory [44] failure criterion is very similar to the Tsai-Hill Theory, except that the absolute value of the cross product term is taken as

$$I_F = \frac{\sigma_{11}^2}{X^2} - \frac{|\sigma_{11}\sigma_{22}|}{X^2} + \frac{\sigma_{22}^2}{Y^2} + \frac{\sigma_{12}^2}{S^2} < 1.0 \quad (4\text{-}22)$$

The difference between these two criterions takes effect only when σ_{11} and σ_{22} have opposite signs.

Output Variables

In Abaqus/Standard, history output can also be requested for the individual stress theories with output variables MSTRS, TSAIH, TSAIW, and AZZIT and for the strain theory with output variable MSTRN.

4.1.2.1.2. Matrix Material Modeling

Matrix material was modeled as isotropic with elastic-plastic behavior [45] and shear damage failure criterion. A summary of the matrix properties is shown in Table 4-2 [43].

TABLE 4-2

EPOXY RESIN MECHANICAL PROPERTIES

Modulus of elasticity (E), GPa	2.5
Tensile strength, MPa	70
Shear modulus, GPa	1.37
Shear strength, MPa	146
Poisson's ratio	0.3

4.1.2.1.2.1. Damage Initiation for Ductile Material

4.1.2.1.2.1.1. Shear Criterion

*SHEAR FAILURE [44] was used to predict the onset of damage in epoxy. This damage initiation model should be used in conjunction with *PLASTIC [44] material model. The model assumes that the equivalent plastic strain at the onset of damage $\bar{\epsilon}_S^{pl}$ is a function of shear stress ration and strain rate

$$\bar{\epsilon}_S^{pl}\left(\theta_s, \dot{\bar{\epsilon}}^{pl}\right) \tag{4-23}$$

where θ_s is the shear stress ratio

$$\theta_s = \frac{q + k_s p}{\tau_{max}} \tag{4-24}$$

τ_{max} is the maximum shear stress, and k_s is the material parameter. The material fails when the following criterion is met [44]:

$$\omega_S = \int \frac{d\bar{\epsilon}^{pl}}{\bar{\epsilon}_S^{pl}\left(\theta_s, \dot{\bar{\epsilon}}^{pl}\right)} = 1 \tag{4-25}$$

where ω_s is a state variable that increases monotonically with plastic deformation that is proportional to the incremental change in equivalent plastic strain. At each increment during the analysis, the incremental increase in ω_s is computed as

$$\Delta\omega_s = \frac{\Delta\bar{\epsilon}^{pl}}{\bar{\epsilon}_S^{pl}\left(\theta_s, \dot{\bar{\epsilon}}^{pl}\right)} \geq 0 \tag{4-26}$$

4.1.2.1.3. Fiber-Matrix Interface Modeling

The interface was defined by the cohesive section with the *TRACTION SEPARATION [44] law. The onset of damage was based on the *QUADS [44] function, which specifies that damage initiation is based on the quadratic traction-integration law for cohesive elements. The damage evolution of the cohesive section is then based on the strain energy release rate and is defined by *ENERGY [44]. The fiber-matrix interface properties are given in Table 4-3 [43].

TABLE 4-3

FIBER-MATRIX INTERFACE PROPERTIES

Normal strength, MPa	160
Shear strength, MPa	34
Strain energy release rate, J/m^2	50

4.1.2.1.3.1. Linear Elastic Traction-Separation Behavior

It is possible to write the elastic constitutive matrix that relates the nominal stresses to nominal strains across the interface, in which the nominal stresses are the force components divided by the original area at each integration point; while the nominal strains are the separation of nodes at the interface divided by the original thickness at the integration point. The default value of the original constitutive thickness is 1.0 for traction-separation response, which ensures that nominal strain is equal to the relative displacements of the top and bottom faces. The elastic behavior in terms of tractions and separations can be written as [44]

$$\epsilon_n = \frac{\delta_n}{T_0}, \quad \epsilon_s = \frac{\delta_s}{T_0}, \quad \epsilon_t = \frac{\delta_t}{T_0} \tag{4-27}$$

$$t = \begin{Bmatrix} t_n \\ t_s \\ t_t \end{Bmatrix} = \begin{bmatrix} K_{nn} & K_{ns} & K_{nt} \\ K_{sn} & K_{ss} & K_{st} \\ K_{nt} & K_{st} & K_{tt} \end{bmatrix} \begin{Bmatrix} \epsilon_n \\ \epsilon_s \\ \epsilon_t \end{Bmatrix} = K\epsilon \tag{4-28}$$

where t is the traction vector consisting of three components, t_n represents the traction along the normal direction (3-local direction), and t_s and t_t represent two shear tractions along the local 1- and 2-directions in three-dimensional problems. In two-dimensional problems, t_n will be in the local 2-direction, and t_s will be in the local 1-direction. T_0 denotes the original thickness of the cohesive element, and δ_n, δ_s, and δ_t represent the separations corresponding to each traction vector [44].

To formulate the estimation for the parameters required for modeling the traction-separation behavior of an interface in terms of the material properties of the blank adhesive material, the cohesive layer thickness should be considered. If T_c is the cohesive

layer thickness, and E_c and ρ_c are adhesive material stiffness and density, the stiffness of the interface (relating the nominal traction to the displacement) is given by $K_c = (E_c/T_c)$, and the density of interface is given by $\bar{\rho}_c = (\rho_c T_c)$ [44].

4.1.2.1.3.2. Damage Modeling

Each failure mechanism consists of three ingredients: a damage initiation criterion, a damage evolution law, and a choice of element removal when the damage state is completely reached. Four damage initiation criterions are available for the traction-separation material response in Abaqus.

4.1.2.1.3.2.1. Damage Initiation

Damage is assumed to initiate when the maximum nominal stress ratio reaches a value of one or [44]

$$\max\left\{\frac{\langle t_n \rangle}{t_n^0}, \frac{t_s}{t_s^0}, \frac{t_t}{t_t^0}\right\} = 1 \tag{4-29}$$

where, t_n^0, t_s^0, and t_t^0 represent the peak values of the nominal stress when the deformation is either purely normal to the interface or purely in the first or second shear direction, respectively.

$$\max\left\{\frac{\langle \epsilon_n \rangle}{\epsilon_n^0}, \frac{\epsilon_s}{\epsilon_s^0}, \frac{\epsilon_t}{\epsilon_t^0}\right\} = 1 \tag{4-30}$$

$$\left\{\frac{\langle t_n \rangle}{t_n^0}\right\}^2 + \left\{\frac{t_s}{t_s^0}\right\}^2 + \left\{\frac{t_t}{t_t^0}\right\}^2 = 1 \tag{4-31}$$

$$\left\{\frac{\langle \epsilon_n \rangle}{\epsilon_n^0}\right\}^2 + \left\{\frac{\epsilon_s}{\epsilon_s^0}\right\}^2 + \left\{\frac{\epsilon_t}{\epsilon_t^0}\right\}^2 = 1 \quad (4\text{-}32)$$

Equations (4-30) to (4-32) show the "maximum nominal strain criterion," "quadratic nominal stress criterion," and "quadratic nominal strain criterion," respectively, in which, $\epsilon_n^0, \epsilon_s^0$, and ϵ_t^0 represent the peak values of the nominal strain when the deformation is either purely normal to the interface or purely in the first or the second shear direction.

4.1.2.1.3.2.2. Damage Evolution

The damage evolution law describes the rate at which the material stiffness is degraded once the corresponding initiation criterion is reached. A scalar variable, D, represents the damage in the material and takes the effect of all active damage mechanisms. The interval of D is from 0 to 1. Two components define the evolution of damage. The first component is either the effective displacement at complete failure δ_m^f, relative to the effective displacement at the initiation of damage δ_m^0, or the dissipated failure energy G^C [44]:

$$\delta_m = \sqrt{\langle \delta_n \rangle^2 + \delta_s^2 + \delta_t^2} \quad (4\text{-}33)$$

The second component to the definition of damage evolution is the evolution law, and consequently, damage variable, D, between the damage initiation and the material's final failure. Figure 4-6 shows a linear softening law.

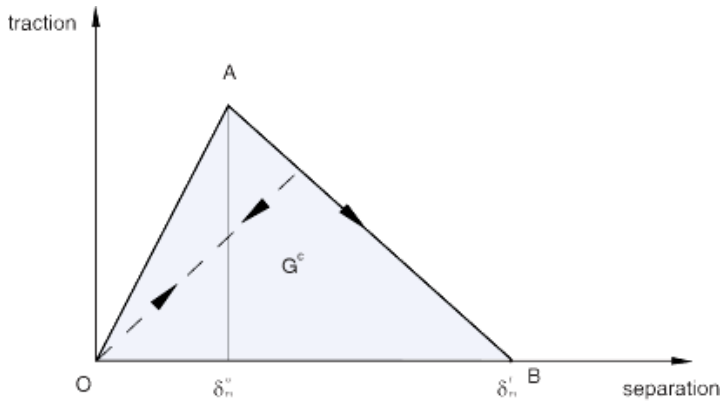

Figure 4-6. Linear damage evolution [43]

Two of the most used damage evolutions are the "power law" and "Benzeggagh-Kenane (BK)," which define the dependency of the fracture energy on the mode mix. Equation (4-34) shows the power law interaction of the energies required to cause failure in the individual (normal and two shear) modes:

$$\left\{\frac{G_n}{G_n^C}\right\}^\alpha + \left\{\frac{G_s}{G_s^C}\right\}^\alpha + \left\{\frac{G_t}{G_t^C}\right\}^\alpha = 1 \tag{4-34}$$

where G_n, G_s, and G_t refer to the work done by the traction and its conjugate relative displacement in the normal, first-, and second-shear directions, respectively, and G_n^C, G_s^C, and G_t^C are the critical fracture energies that should be specified as input.

Equation (4-35) shows the BK fracture criterion, which is particularly useful when the critical fracture energies during deformation purely along the first and second shear directions are the same, i.e., $G_s^C = G_t^C$:

$$G_n^C + (G_s^C - G_n^C)\left\{\frac{G_S}{G_T}\right\}^{\eta} = G^C \tag{4-35}$$

where

$$\begin{aligned} G_S &= G_s + G_t \\ G_T &= G_n + G_S \end{aligned} \tag{4-36}$$

and η is the material parameter [44].

Figure 4-7 schematically represents how damage initiation and evolution depend on the mode mix for a traction-separation response with isotropic shear behavior.

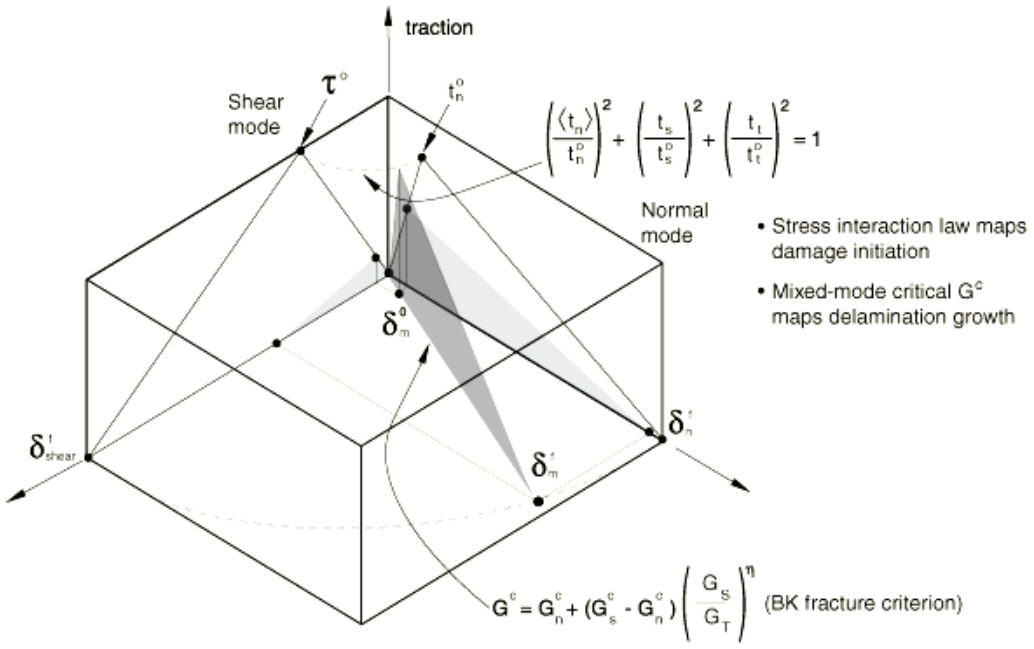

Figure 4-7. Illustration of mixed-mode response in cohesive elements [43]

4.1.2.1.4. Simulation Procedure

Conventionally, in the machining of homogeneous material, a plane strain analysis is used, but due to out-of-plane displacements in the machining of FRPs, the plane stress analysis should be used [27, 46-47].

Finite element analysis was studied using Abaqus/Explicit. The tool was modeled as a 2D planar discrete rigid. The workpiece was modeled with four different zones: fiber, matrix, equivalent homogeneous material (EHM), and fiber-matrix interface. The objective of this analysis was to find the fiber-matrix debonding length when the tool is cutting the material. The workpiece dimensions were $2000\mu m \times 1000\mu m$ with two fibers. There was a matrix layer between each fiber and a cohesive material zone as the fiber-matrix interface. The rest of the workpiece was modeled as EHM by an equivalent transversely isotropic homogeneous single-phase material with properties (E_{11}, E_{22}, G_{12}, and ν_{12}), determined from the rule of mixtures [1, 48], equations (4-37) to (4-40). Figure 4-8 shows a schematic finite element model used as workpiece.

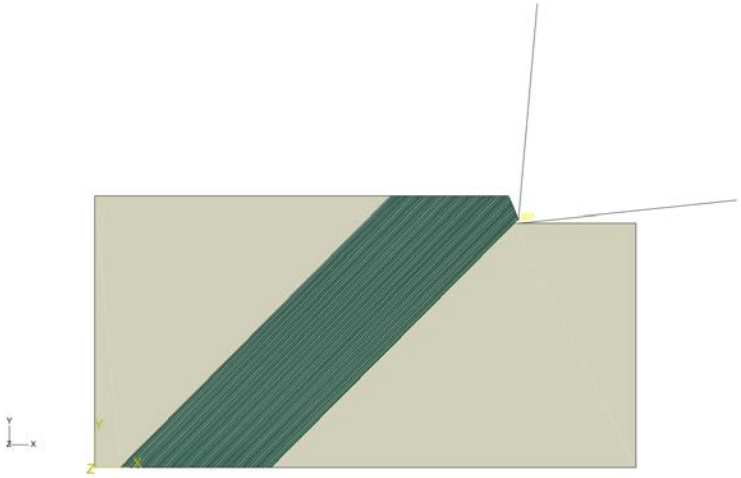

Figure 4-8. Schematic view of the fiber, matrix and EHM zones used in FEM for the case of 135° fiber orientation and %60 fiber volume fraction

$$E_{11} = v_f E_f + v_m E_m \tag{4-37}$$

$$E_{22} = \frac{E_f E_m^{'}}{v_f E_m^{'} + v_m E_f} \qquad E_m^{'} = \frac{E_m}{1 - v_m^2} \tag{4-38}$$

$$G_{12} = \frac{G_f G_m}{v_f G_m + v_m G_f} \tag{4-39}$$

$$\nu_{12} = v_f \nu_f + v_m \nu_m \tag{4-40}$$

Carbon fiber was modeled with isotropic material properties. Since EHM zones are not isotropic, material orientation should be defined for each zone. If an orthotropic model is used for carbon fibers, they can share the same coordinate system with EHM zones.

4.1.2.1.5. Element Selection

Fully integrated elements in Abaqus/Standard and Abaqus/Explicit do not hourglass but may experience "locking" behavior: both shear and volumetric [44]. Shear locking occurs in first-order, fully integrated elements (in Abaqus, CPS4, CPE4, C3D8, etc.) that are subjected to bending; however, using a reduced integration will solve this problem. The numerical formulation of the elements causes shear strains that do not really exist. Therefore, these elements are too stiff in bending, particularly if the element length is of the same order of magnitude as or greater than the wall thickness.

Volumetric locking takes place in fully integrated elements when the material behavior is (almost) incompressible. Unrealistic pressure stresses develop at the integration points, resulting in stiff behavior of the element against deformations that

should cause no volume changes. For almost incompressible materials (elastic-plastic materials for which the plastic strains are incompressible), second-order and fully integrated elements start to develop volumetric locking when the plastic strains are about the elastic strains. However, the first-order, fully integrated quadrilaterals and hexahedra elements use selectively reduced integration (reduced integration in volumetric terms). Therefore, these elements do not lock with almost incompressible materials. Reduced-integration, second-order elements develop volumetric locking for almost incompressible materials, only after significant straining occurs. In this case, volumetric locking often comes with a mode that looks like hourglassing. Normally, this problem can be avoided by refining the mesh in regions of large plastic strain [44].

If volumetric locking is suspected, by checking the pressure stress at the integration points, it is possible to determine if any volumetric locking is occurring. If the pressure values show a checkerboard pattern that is changing significantly from one integration point to the next, then volumetric locking is occurring. Therefore, in this analysis CPS4R (reduced integration four-node element) with enhanced hourglass control was used for both matrix and fiber to avoid shear locking [44]. Increasing the number of layers does not improve the results. However, more layers are required for accurate analysis when material nonlinearities are present [49]. With reduced integration, the number of elements through the depth of in-plane bending plays a critical role. For this problem, two elements through the depth fail to maintain accurate enough results. Four elements through the depth provide acceptable results. If the idealization involves only one element through the depth, the material integration points would all lie on the neutral axis, and the bending behavior would depend entirely on the (artificial) hourglass stiffness for the case of

reduced integration. Combined with enhanced hourglass control, the CPS4R, C3D8R, and S4R elements provide excellent results, even with four elements along the depth [49].

A four-node bilinear plane stress quadrilateral element (CPS4R) with reduced integration was used for the fiber and matrix material with enhanced hourglass control to avoid shear and volumetric locking. Element deletion was activated for fibers and cohesive elements; however, the matrix material will distort without element deletion. Different material layers were generated by partitioning; therefore, no contact was defined between fiber, matrix, and interface. In this case, matrix element deletion may result in penetration of the fiber elements into the matrix. Another approach would be to model each layer separately and then assemble the layers. For the latest approach, the side boundaries of each layer should be included in the contact definition. The advantage of using this method is the ability to activate element deletion for the matrix material; however, as the number of fibers and matrix layers increases, it is more difficult to use this approach. Moreover, if the material undergoes a complete damage, element deletion removes the element from analysis. This may result in inaccurate results.

4.1.2.1.6. Cohesive Response Using Penalty Stiffness

According to section 4.1.2.1.3.1, as the thickness of the cohesive element gets closer to zero, the stiffness of the cohesive element tends to infinity. One way to avoid any adverse effect on the stable time increment is to choose material property such that $\Delta t_c = \Delta t_e$, where Δt_c is the time increment of the cohesive element, and Δt_e is that of neighboring elements.

For constitutive response defined in terms of traction versus separation, the ratio of the stable time increment of the cohesive elements to that for the other elements is given by [44]

$$\frac{\Delta t_c}{\Delta t_e} = \sqrt{\left(\frac{\bar{\rho}_c}{\bar{\rho}_e}\right)\left(\frac{\mathrm{K_e}}{\mathrm{K_c}}\right)} \tag{4-41}$$

where subscripts "c" and "e" correspond to the cohesive elements and the surrounding elements, respectively.

The surrounding elements properties can be used to calculate the stiffness and density of the cohesive elements.

$$K_c = \frac{E_c}{T_c} = \frac{1}{10}\frac{E_e}{T_e} = 0.1K_e \tag{4-42}$$

$$\bar{\rho}_c = \rho_c T_c = \frac{1}{10}\rho_e T_e = 0.1\bar{\rho}_e \tag{4-43}$$

where T_e represents the characteristic length of the neighboring non-cohesive elements. By choosing $K_c = 0.1K_e$, the stiffness in the cohesive layer relative to the surrounding elements will be similar to the default stiffness used by penalty contact in Abaqus/Explicit. The cohesive element stiffness in this approach is different from the measured stiffness of the interface; however, if the peak strength and the fracture energy remain unchanged, the global response will not be affected significantly in many cases [44].

The stiffness of the cohesive elements in this study was calculated based on the traction-separation law.

4.1.2.1.7. Finite Element Analysis of Debonding Length Predictions

The finite element analysis was run on a unidirectional material with mechanical properties given in Table 4-1, Table 4-2, and Table 4-3. Figure 4-9, Figure 4-10, and Figure 4-11 show sample pictures of the cutting simulation with Abaqus.

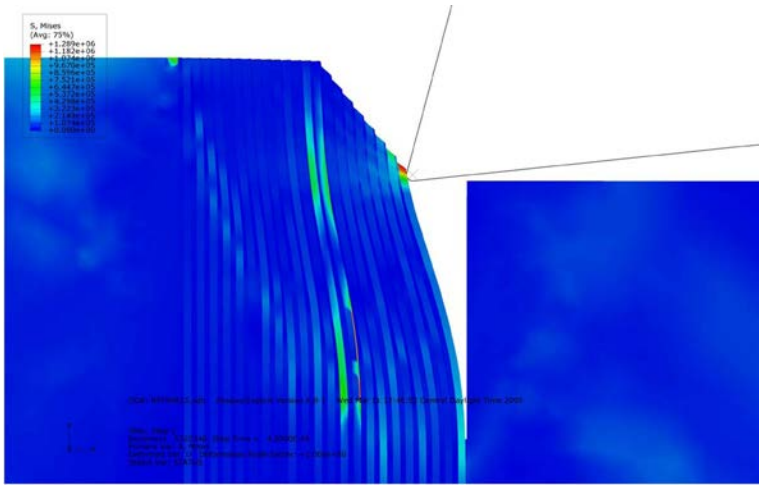

Figure 4-9. Abaqus model of fiber bending for $\theta = 90°$ and $\gamma = 15°$

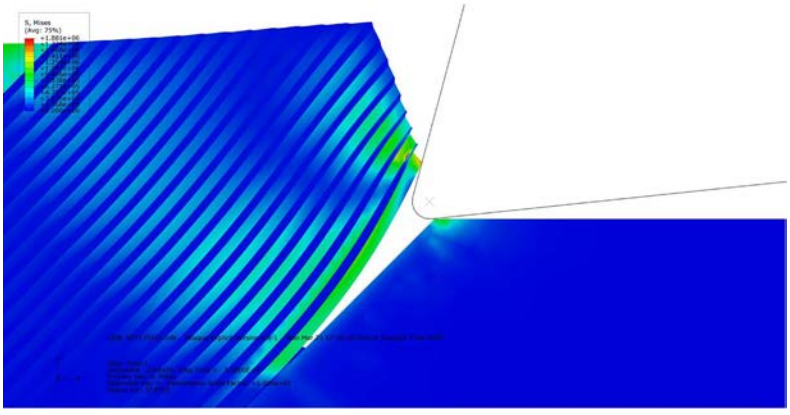

Figure 4-10. Abaqus model of fiber bending for $\theta = 135°$ and $\gamma = 15°$

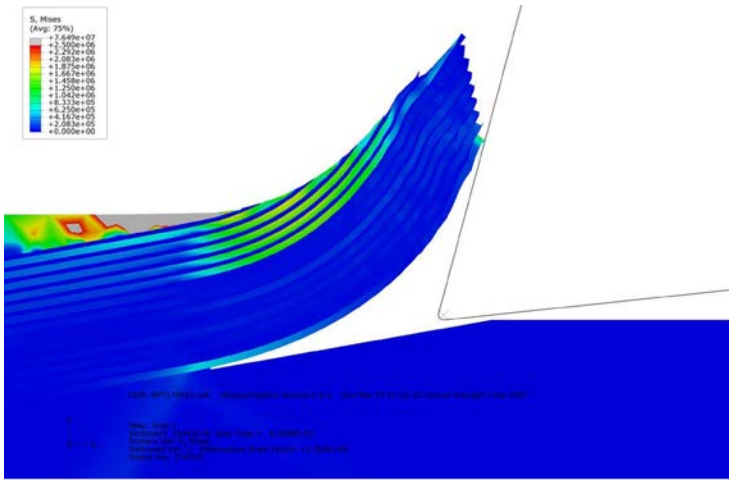

Figure 4-11. Abaqus model of fiber bending for $\theta = 170°$ and $\gamma = 15°$

The length at which the fibers break due to excessive normal force can be measured using the Abaqus post-processer. The failure criterion is the maximum in-plane principal stress, and it is assumed that the fiber fails if any element meets the criterion. This length was measured for different combinations of fiber orientations and tool rake angles, and the results are shown in Figure 4-12.

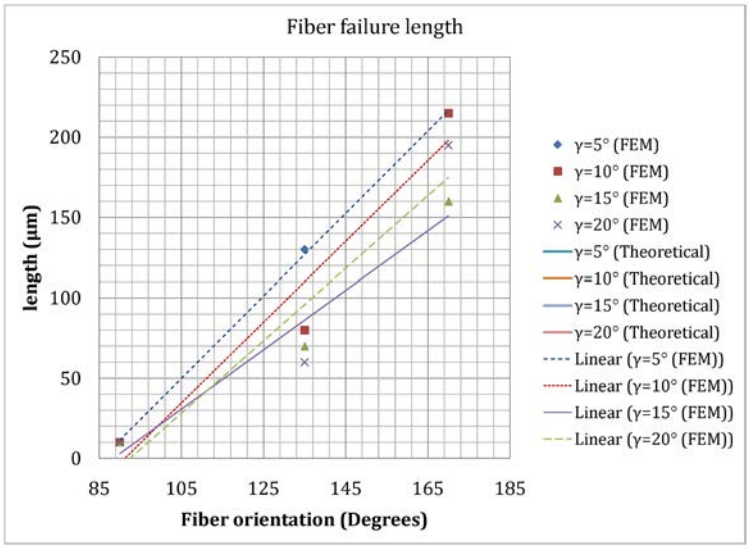

Figure 4-12. Lengths at which fibers break due to excessive normal stress

4.1.2.2. Analytical Method – Thrust Force

4.1.2.2.1. Region 1 – Fiber Microbuckling

4.1.2.2.1.1. Model 1 – Perfectly Aligned Fibers with Aligned Axial Force

The compressive failure characteristics of a fiber can be studied by embedding it in a resin casting [50]. Fiber microbuckling can be studied in both two- and three-dimensional models. The study of each case depends on the status of stress in the material. In the orthogonal cutting of composites, the plane stress analysis should be used [27, 46-47]. Equations (4-44) and (4-45) represent the predicted stress that causes buckling in composites in the extension and shear modes, respectively, as shown in (Figure 4-13) [51].

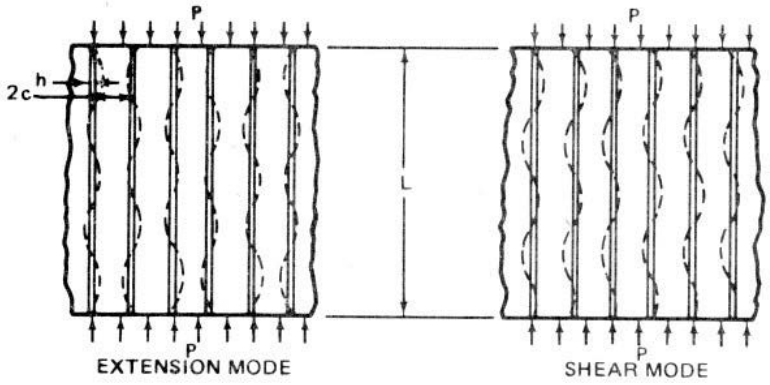

Figure 4-13. Possible buckling patterns for unidirectional composites [51]

$$\sigma_{CE} = \frac{\pi^2 E_f h^2 k}{12L^2}\left[m^2 + \frac{24L^4 E_m}{\pi^4 c h^3 E_f}\left(\frac{1}{m^2}\right)\right] \tag{4-44}$$

$$\sigma_{CS} = \frac{G_m}{(1-k)} + \frac{\pi^2 E_f k}{12}\left(\frac{mh}{L}\right)^2 \tag{4-45}$$

where E_f is the Young modulus of the fiber, k is the volume fraction of the reinforcement, L is the length of composite specimen, m is the number of buckle waves, h is the thickness of

reinforcement or laminas, $2c$ is the thickness of matrix between laminas, and G_m is the shear modulus of the matrix.

Equations (4-44) and (4-45) were derived for simply supported ends of the individual laminas. If the laminas are not simply supported, then equation (4-46) should be used, in which λ depends on the end boundary condition of the individual lamina and gives the values of λ as a function of $L/2R$, where L is the specimen length, and R is the radius of the end of the lamina [51].

$$\sigma_{CS} = \frac{G_m}{1-k} + \lambda \frac{\pi^2 E_f k}{12} \left(\frac{mh}{L}\right)^2 \tag{4-46}$$

For a square-ended lamina, $R = \infty$, and according to Table 4-4, $\lambda = 4$, which corresponds to the fixed-end condition. Table 4-4 shows that $1 \leq \lambda \leq 4$, depending on the rounded-end radius. For $R = 0$, $\lambda = 1$, which corresponds to laminates with simply supported ends.

TABLE 4-4

END FIXITY PARAMETER λ AS A FUNCTION OF $L/2R$ [51]

$\frac{L}{2R}$	0	1	2	4	6	8	10	15	20	30	40	50	∞
λ	4	3.17	2.45	1.69	1.42	1.30	1.23	1.15	1.11	1.07	1.05	1.04	1

For a composite made of a given combination of materials, the composite stress σ_{CE} and σ_{CS} must be minimized with respect to the number of buckle waves m to minimize the valus of σ_{CE} and σ_{CS}. For any given k, the smaller value of σ_{CE} or σ_{CS} is the governing stress.

Generally, for $k \leq 0.1$, equation (4-44) gives a lower microbuckling stress, whereas for $k \geq 0.1$, the governing equation for the minimum stress is given by equation (4-45).

In the edge trimming of FRPs, when $90° \leq \theta \leq 180°$, it is assumed that the cutting process causes microbuckling of the fibers due to the tool nose radius. Knowing the critical stress causing microbuckling and fiber volume fraction (v_f), it is possible to estimate the thrust force, assuming that all of the thrust force causes fiber microbuckling.

For a more complicated case of microbuckling analysis, which is especially useful in the oblique machining of composites, a circular fiber-reinforced composites model can be used. When this type of composite is subjected to compressive loading aligned with the fiber direction, two types of microbuckling mechanisms can cause failure: microbuckling in the extension mode and microbuckling in the shear mode [52]. Both failure modes are shown in Figure 4-13. According to the literature on microbuckling analysis of laminate-reinforced composites, the first mode (extension mode) will take place if the fiber volume fraction of the composite is less than 0.1, ($k \leq 0.1$), whereas microbuckling in the shear mode will take place at higher fiber volume fractions ($k \geq 0.1$). An approximate solution for the latter problem was obtained using the energy method.

If force P is being applied on a composite coupon, the change in the strain energy of the fiber ΔV_f and the matrix ΔV_m must be equal to the work done by the external compressive force P, or [52]

$$\Delta V_f + \Delta V_m = \Delta T \tag{4-47}$$

Assuming the shear mode buckling of fibers with sinusoidal deformation, displacement in the transverse direction can be written in the following series for v [52]:

$$v = \sum_{n=1}^{n=\infty} a_n \sin\frac{n\pi x}{L} \tag{4-48}$$

and the strain energy of bending of the fiber is [52]

$$\Delta V_f = \frac{E_f I_f}{2} \int_0^L \left(\frac{d^2 v}{dx^2}\right)^2 \tag{4-49}$$

$$dx = \frac{\pi^4 E_f I_f}{4L^3} \sum_{n=1}^{n=\infty} n^2 a_n^2 \tag{4-50}$$

The work done by the compressive force P acting on a fiber can be calculated as [52]

$$\Delta T = \frac{P\pi^2}{4L} \sum_{n=1}^{n=\infty} n^2 a_n^2 \tag{4-51}$$

Assuming there is no shear deformation in the fiber, the changes in the strain energy associated with extensional stresses in the matrix can be written as [52]

$$\Delta V_m = \frac{1}{2} \int_V \tau_{xym}\ \gamma_{xym}\ dV \tag{4-52}$$

and the integration extends over a repeating volumetric element of composite. Now, a relation between the shear stress τ_{xym}, shear strain γ_{xym} in the matrix and the deformation of the composite and its microstructure should be established.

In the case of circular fiber-reinforced composites the above-mentioned quantities are assumed to be a function of both x and z:

$$\tau_{xym}\,, \gamma_{xym} = f(x, z) \tag{4-53}$$

It can be said that if an external axial load is being applied on the composite, then the conditions of symmetry require that lines *ab*, *bc*, *cd*, and *da* (Figure 4-14) in a deformed repeating element remain parallel to the corresponding lines in the undeformed material. The following relation can now be established between the displacement of the fiber and shear strain in the matrix at any point z on the boundary of the repeating element based on the assumption in equation (4-53).

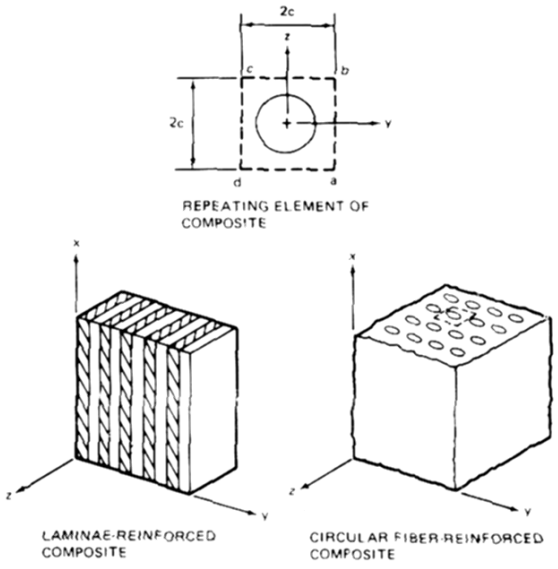

Figure 4-14. Laminae and circular fiber-reinforced composites [52]

Equations (4-54) and (4-55) apply to the square fiber packing of circular fibers [52]:

$$\gamma_{xym} \approx \left(\frac{1}{1-k_z}\right)\left(\frac{dv}{dx}\right) \tag{4-54}$$

$$k_z = \left[\frac{4k}{\pi} - \left(\frac{z}{c}\right)^2\right]^{\frac{1}{2}} \tag{4-55}$$

where k is the fiber volume fraction of the composite, z is a variable, and c is defined in Figure 4-14.

For a given shear strain in the matrix, the shear stress is

$$\tau_{xym} = G_m \gamma_{xym} \tag{4-56}$$

and equation (4-52) becomes

$$\Delta V_m = \frac{G_m}{2}\int_V \left(\frac{\frac{dv}{dx}}{1-k_z}\right)^2 dV \tag{4-57}$$

where differentiation of equation (4-48) with respect to x and substitution for dv/dx and integration of the resultant equation over the wavelength L yields [52]

$$\Delta V_m = \frac{cG_m\pi^2}{2L}\sum_{n=1}^{n=\infty} n^2 a_n^2 \int_{-c}^{c} \frac{dz}{1-k_z} \tag{4-58}$$

Using equations (4-47), (4-50), (4-52), and (4-58) and solving for P yields [52]

$$P = \left[2cG_m \sum_{n=1}^{n=\infty} n^2 a_n^2 \int_{-c}^{c} \frac{dz}{1-k_z} + \frac{\pi^2 E_f I_f}{L^2} \sum_{n=1}^{n=\infty} n^4 a_n^2\right] / \sum_{n=1}^{n=\infty} n^2 a_n^2 \tag{4-59}$$

and the critical value of the load P can be expressed as [52]

$$P_{cr} = 2cG_m \int_{-c}^{c} \frac{dz}{1-k_z} + \frac{\pi^2 E_f I_f}{L^2} m^2 \tag{4-60}$$

where m is the number of buckle waves corresponding to P_{cr}.

The critical compressive fiber stress is [52]

$$\sigma_{f_{cr}} = \frac{2cG_m}{\pi r^2} \int_{-c}^{c} \frac{dz}{1-k_z} + \frac{\pi^2 E_f}{4} \left(\frac{rm}{L}\right)^2 \tag{4-61}$$

where, for the square fiber packing,

$$c = r\left(\frac{\pi}{4k}\right)^{\frac{1}{2}} \tag{4-62}$$

and L/m represents the buckle wavelength.

$$G_{LT} = \frac{1}{2c} \int_{-c}^{c} \left(\frac{G_m}{1-k_z}\right) dz \tag{4-63}$$

where G_{LT} is the shear modulus of a circular fiber-reinforced composite [53].

Plugging equations (4-62) and (4-63) into equation (4-61), minimizing this with respect to m, and making use of relationship $\sigma_{f_{cr}} k = \sigma_{c_{cr}}$, the final equation for microbuckling stress of a composite with simply supported fibers at the end becomes [52]

$$\sigma_{c_{cr}} = G_{LT} + \left(\frac{\pi^2 E_f k}{4}\right)\left(\frac{r}{L}\right)^2 \tag{4-64}$$

For the fixed ends fibers, the equation will be [52]

$$\sigma_{c_{cr}} = G_{LT} + \pi^2 E_f k \left(\frac{r}{L}\right)^2 \tag{4-65}$$

For a plane stress analysis, equation (4-53) can be used to compute the microbuckling stress. To minimize the value of σ_{CS}, the value of m, which represents the number of buckling waves, should be equal to one. In addition, the fiber volume fraction can be written in terms of the matrix and reinforcement lamina thickness, where λ depends on the end fixed condition of the fibers, which, for the case of edge trimming, is the clamped-free condition. However, there is not such a condition in Table 4-4. From the mechanics of the material, a column with a clamped-free boundary condition can be replaced by a simply supported column at both ends with an effective length of $L/2$. Therefore [52],

$$k = \frac{h}{2c + h}, \;\; \lambda = 1 \tag{4-66}$$

$$\sigma_{CS} = \frac{(2c + h)}{2c} G_m + \frac{\pi^2 E_f h}{12(2c + h)}\left(\frac{2h}{L}\right)^2 \tag{4-67}$$

where L in equation (4-67), is the length of the composite specimen, which, in this case, is the fiber-matrix debonding length that was computed using FEM in section 4.1.2.1.

To calculate the buckling force, the microbuckling stress in equation (4-67) should be multiplied by the area of the tool nose, which contributes to microbuckling. The red face (Face 1) shown in Figure 4-15 causes fiber microbuckling since, according to the cutting direction, the fibers undergoing the red area will fail due to microbuckling and the ones contacting the blue area (Face 2) will be conducted to the rake face of the tool, thus generating no thrust force. The distribution of force along Face 1 is not linear, and for each infinitesimal area, the force is calculated using equation (4-68) and then integrated over the total arc angle. It is assumed that the resultant force at Region 1 is along the fibers, thus causing microbuckling. The resultant force then can be projected along the horizontal and vertical directions to determine the thrust and cutting force.

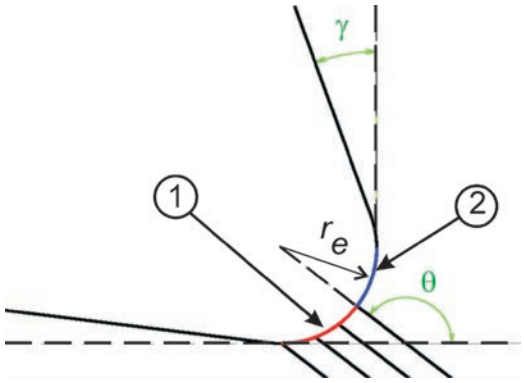

Figure 4-15. Tool nose area causing fiber microbuckling

$$dF = \sigma_{CS} dA = \sigma_{CS} r_e d\phi \tag{4-68}$$

$$dF_n = dF \cos\left(\theta - \phi - \frac{\pi}{2}\right) = r_e \sigma_{CS} \cos\left(\theta - \phi - \frac{\pi}{2}\right) d\phi \tag{4-69}$$

$$dF_n = -dF \sin\left(\theta - \phi - \frac{\pi}{2}\right) = -r_e \sigma_{CS} \sin\left(\theta - \phi - \frac{\pi}{2}\right) d\phi \tag{4-70}$$

Figure 4-16 shows a schematic picture of forces acting on the part of the tool nose compressing the fibers.

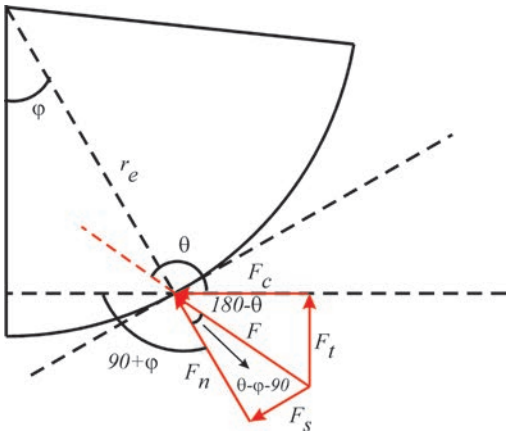

Figure 4-16. Tool nose force diagram

Simplifying equations (4-69) and (4-70)

$$dF_n = r_e \sigma_{CS} \sin(\theta - \varphi)\, d\phi \tag{4-71}$$

$$dF_s = r_e \sigma_{CS} \cos(\theta - \varphi) d\phi \tag{4-72}$$

According to Figure 4-17, dF_c and dF_t can be written as

$$dF_c = -dF \cos(\pi - \theta) = -dF \cos\theta = -\sigma_{CS} r_e \cos\theta\, d\phi \tag{4-73}$$

$$dF_c = -dF \sin(\pi - \theta) = -dF \sin\theta = -\sigma_{CS} r_e \sin\theta\, d\phi \tag{4-74}$$

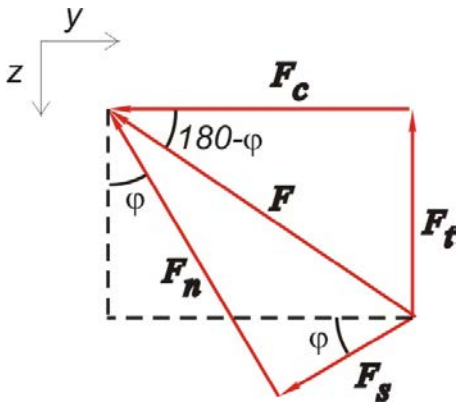

Figure 4-17. Angles of forces acting on nose of cutting tool

The total thrust force and the portion of cutting force causing by the tool nose radius can be calculated by integrating equations (4-73) and (4-74) over the angle of region one shown in Figure 4-15.

$$F_{c_1} = \int_0^{\theta-\frac{\pi}{2}} -\sigma_{CS} r_e \cos\theta d\phi = -\sigma_{CS} r_e \left(\theta - \frac{\pi}{2}\right)\cos\theta \tag{4-75}$$

$$F_{t_1} = \int_0^{\theta-\frac{\pi}{2}} -\sigma_{CS} r_e \sin\theta d\phi = -\sigma_{CS} r_e \left(\theta - \frac{\pi}{2}\right)\sin\theta \tag{4-76}$$

Substituting from equation (4-67)

$$F_{c_1} = -\left[\frac{(2c+h)}{2c} G_m + \frac{\pi^2 E_f h}{3(2c+h)}\left(\frac{h}{L}\right)^2\right] r_e \left(\theta - \frac{\pi}{2}\right)\cos\theta \tag{4-77}$$

$$F_{t_1} = -\left[\frac{(2c+h)}{2c} G_m + \frac{\pi^2 E_f h}{3(2c+h)}\left(\frac{h}{L}\right)^2\right] r_e \left(\theta - \frac{\pi}{2}\right)\sin\theta \tag{4-78}$$

Experiments show that the values of the thrust force are much lower than the ones calculated from equation (4-78), which is due to the assumption of the model. This model

assumes that the fibers are perfectly aligned with each other and with the compressive axial force, which is not valid in reality. Any waviness of lateral force on the fibers significantly reduces the microbuckling stress. This can be corrected by considering an initial deformation in the fibers with lateral force acting on it.

The above-mentioned method is more accurate if the tool nose radius is significantly bigger than the fiber diameter; however, if it is smaller than the fiber diameter, the following method will better predict the contribution of the tool nose to the cutting and thrust forces.

$$F_{c_1} = -\left[\frac{(2c+h)}{2c}G_m + \frac{\pi^2 E_f h}{3(2c+h)}\left(\frac{h}{L}\right)^2\right]\pi r^2 \frac{H}{c+2r}\cos\theta \tag{4-79}$$

$$F_{t_1} = -\left[\frac{(2c+h)}{2c}G_m + \frac{\pi^2 E_f h}{3(2c+h)}\left(\frac{h}{L}\right)^2\right]\pi r^2 \frac{H}{c+2r}\sin\theta \tag{4-80}$$

4.1.2.2.1.2. Model 2 – Undulating Fiber Model

Model 2 is same as Model 1; however, in this model, it is assumed that the resultant force acting on the unidirectional composite at the tool nose is aligned with the fibers. Figure 4-18 shows a schematic picture of fibers with initial waviness, and the forces and moments acting on an infinitesimal element of the fiber surrounding by the matrix material. The importance of initial fiber curvature has been pointed out and incorporated in the model by many investigators [54-58].

The initial waviness of the fibers can be shown in a *sine* form function as [59]

$$v_0 = B_0 \sin\frac{\pi x}{L} \tag{4-81}$$

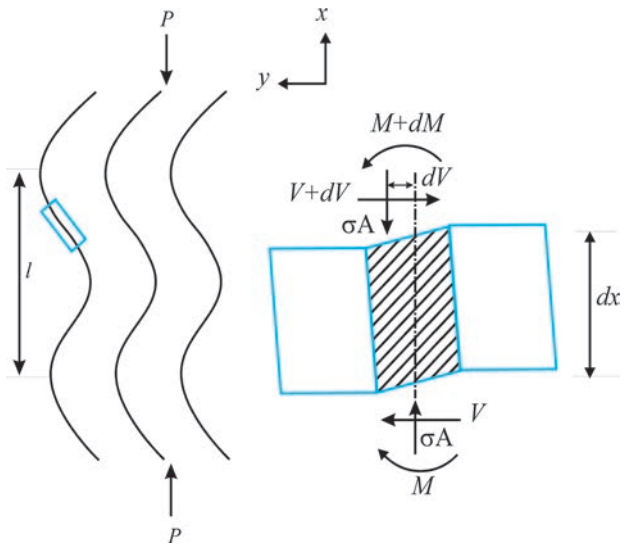

Figure 4-18. Schematic picture of fibers with initial waviness

where, v_0 is the equation of initial fiber wave, and B_0 and L are the amplitude and the wavelength of the *sine* form function, respectively.

The resulting fiber wave equation after loading can be written in the same manner as [59]

$$v = B \sin\frac{\pi x}{L} \tag{4-82}$$

The equation of moment equilibrium for the infinitesimal fiber element shown in Figure 4-18 is [59]

$$-M + (M + dM) + \sigma A dv - \frac{V dx}{2} - (V + dV)\frac{dx}{2} = 0 \tag{4-83}$$

where σ is the average stress on the element, A is the fiber cross-sectional area, and M and V are the internal resultants.

Ignoring the small terms (second-order differentiations) and dividing by dx yields [59]

$$\frac{dM}{dx} + \sigma A \frac{dv}{dx} - V = 0 \tag{4-84}$$

$$M = E_f I_f \frac{d^2}{dx^2}(v - v_0) \tag{4-85}$$

Assuming small axial displacement, the shear strain in the matrix can be approximately written as [59]

$$\gamma_{xym} = \frac{d}{dx}(v - v_0) \tag{4-86}$$

Since shear is dominated by the matrix [59],

$$V = AG_{LT} \frac{d}{dx}(v - v_0) \tag{4-87}$$

where, G_{LT} is the shear modulus of composites. Substituting equations (4-85) and (4-87) into equation (4-84) and evaluating at $x = L$ yields [59]

$$\sigma A\, B = \left(E_f I_f \frac{\pi^2}{L^2} + A.G_{LT}\right)(B - B_0) \tag{4-88}$$

By letting B_c be the waviness amplitude at failure, the critical composite strength can be written as [59]

$$\sigma_c = \left(\frac{E_f I_f \pi^2}{AL^2} + G_{LT}\right)\left(1 - \frac{B_0}{B_c}\right) \tag{4-89}$$

The term $E_f I_f \pi^2 / AL^2$ in equation (4-89) can be neglected since it is very small in comparison to G_{LT}. Therefore, the equation can be rewritten as [59]

$$\sigma_c = G_{LT}\left(1 - \frac{B_0}{B_c}\right) \tag{4-90}$$

where B_c can take two values depending on the failure mode: one associated with fiber bending and the other associated with matrix or interface shear failure. Failure is controlled by shear. This failure occurs when the shear stress in composites reaches the critical shear strength of the matrix of the fiber-matrix interface. The maximum shear in the matrix can be calculated from equation (4-87) as [59]

$$\tau_{xym} = G_{LT}\frac{\pi}{L}(B - B_0) \tag{4-91}$$

The matrix material fails when $B = B_c$ and $\tau_{xym} = \tau_c$. The term τ_c is the shear strength of matrix or the fiber-matrix interface. Therefore, the critical value of the waviness amplitude can be written as [59]

$$B_c^{shear} = \frac{\tau_c}{G_{LT}}\frac{L}{\pi} + B_0 \tag{4-92}$$

A composites buckling strength in the shear mode can be determined by substituting B_c^{shear} from equation (4-92) into equation (4-90) or [59]

$$\sigma_c^{shear} = \frac{G_{LT}}{1 + \pi \frac{B_0}{L} \frac{G_{LT}}{\tau_c}} \tag{4-93}$$

Here, failure is controlled by the bending of the fiber.

In this failure mode, when the flexural stress in the fiber reaches its flexure strength, the composite fails. From equation (4-85), the flexural strength of the fiber can be written as [59]

$$X_c^f = E_f r \frac{\pi^2}{l^2} (B_c^{bend} - B_0) \tag{4-94}$$

where X_c^f is the flexure strength of fiber, and r is the fiber radius. Solving the above equation for B_c^{bend} [59]

$$B_c^{bend} = \frac{X_c^f}{E_f} \frac{L^2}{\pi^2 r} + B_0 \tag{4-95}$$

and the composites strength in the fiber bending mode is [59]

$$\sigma_c^{bend} = \frac{G_{LT}}{1 + \pi^2 \left(\frac{B_0}{2L^2}\right) \left(\frac{2rE_f}{X_c^f}\right)} \tag{4-96}$$

Failure that is controlled by matrix shear and failure that is controlled by bending of fiber result in two different buckling stresses whereby the minimum of these failure modes gives the composites strength in compression. The undulated fiber model gives a better estimate of the critical buckling stress compared to the perfectly aligned fibers composites, since it considers the fibers waviness defect, which has a big impact on the compressive strength [59]. Equation (4-96) is likely to be applicable to Kevlar/epoxy composites, because the flexural strength of Kevlar fibers is very low [60].

The orthogonal edge trimming thrust force and the contribution of tool nose to the cutting force can be calculated using equations (4-75) and (4-76), based on the shear failure mode:

$$F_{c_1} = -\frac{G_{LT}}{1+\pi\frac{B_0}{L}\frac{G_{LT}}{\tau_c}} r_e \left(\theta - \frac{\pi}{2}\right)\cos\theta \tag{4-97}$$

$$F_{t_1} = -\frac{G_{LT}}{1+\pi\frac{B_0}{L}\frac{G_{LT}}{\tau_c}} r_e \left(\theta - \frac{\pi}{2}\right)\sin\theta \tag{4-98}$$

and for the failure mode controlled by the bending of fibers, equations (4-99) and (4-100) can be used:

$$F_{c_1} = -\frac{G_{LT}}{1+\pi^2\left(\frac{B_0}{2L^2}\right)\left(\frac{2rE_f}{X_c^f}\right)} r_e \left(\theta - \frac{\pi}{2}\right)\cos\theta \tag{4-99}$$

$$F_{t_1} = -\frac{G_{LT}}{1+\pi^2\left(\frac{B_0}{2L^2}\right)\left(\frac{2rE_f}{X_c^f}\right)} r_e \left(\theta - \frac{\pi}{2}\right)\sin\theta \tag{4-100}$$

For smaller fiber radii, equations (4-101) and (4-102) give a better prediction:

$$F_{c_1} = -\frac{G_{LT}}{1 + \pi^2 \left(\frac{B_0}{2L^2}\right)\left(\frac{2rE_f}{X_c^f}\right)} \pi r^2 \frac{H}{c + 2r} \cos\theta \tag{4-101}$$

$$F_{t_1} = -\frac{G_{LT}}{1 + \pi^2 \left(\frac{B_0}{2L^2}\right)\left(\frac{2rE_f}{X_c^f}\right)} \pi r^2 \frac{H}{c + 2r} \sin\theta \tag{4-102}$$

4.1.2.2.1.3. Model 3 – Buckling Considering Lateral Force

The presence of lateral force acting on the fibers significantly affects the axial buckling force. In this model, it is assumed that the lateral force *s* is acting at the tip of the fiber. This model can be used in the analysis of the cutting thrust force considering the friction. Figure 4-19 shows a schematic view of a single fiber under axial and lateral forces *P* and *s*.

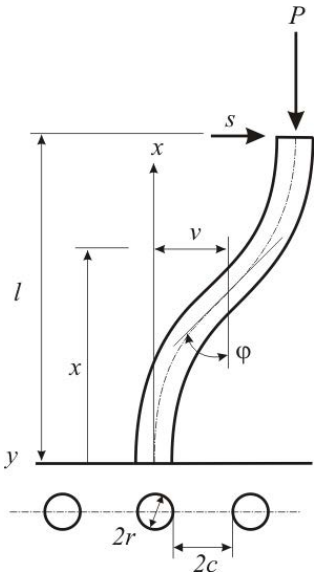

Figure 4-19. Single fiber under axial and lateral force surrounded by matrix material (r = fiber radius; 2c = fiber spacing)

Assumptions for this model include the following [59]:

- Two-dimensional deformation.
- Fiber that cannot shear.
- A matrix that does not elongate/contract, therefore, the only deformation mechanism in the matrix being pure shear.
- Normal stresses in the fiber that produce no mechanical work during deformation, i.e.,

$$\sigma = \frac{P}{A} + \frac{My}{I_f} \approx \frac{My}{I_f} \tag{4-103}$$

Shear stress in the matrix can be written using Hook's law.

$$\tau_{xym} = G_m \gamma_{xym} \tag{4-104}$$

or, according to Figure 4-19,

$$\gamma_{xym} = \left(\frac{c+r}{c}\right)\frac{dv}{dx} \tag{4-105}$$

In addition, total energy in the element is [59]

$$U = -\frac{P}{2}\int_0^L \left(\frac{dv}{dx}\right)^2 dx - \int_0^L s\left(\frac{dv}{dx}\right)dx + \frac{1}{2}\int_0^L E_f I_f \left(\frac{d^2v}{dx^2}\right)^2 dx + \frac{1}{2}\int_0^L A_m \tau_{xym}\gamma_{xym}\, dx \tag{4-106}$$

in which the first two terms are the external work done by external forces P and s, and the last two terms are the internal deformation energy.

According to Figure 4-20, the axial displacement of the free end of the beam can be calculated using equation (4-107) [61]. This displacement is used to find the external work done by the axial force P only.

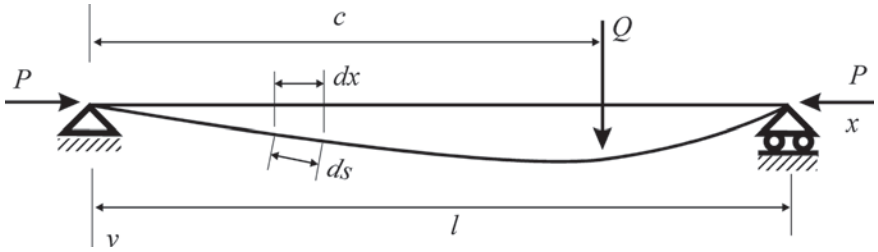

Figure 4-20. A beam under axial force

$$ds - dx = dx\sqrt{1 + \left(\frac{dv}{dx}\right)^2} - dx \approx \frac{1}{2}\left(\frac{dv}{dx}\right)^2 dx \tag{4-107}$$

Using the principal of virtual work and equation (4-106) [62-63]

$$\begin{aligned}\delta U = E_f I_f \int_0^L \left(\frac{d^2v}{dx^2}\right)\left(\frac{d^2}{dx^2}\delta v\right) dx \\ + \left(-P + A_m\left(1 + \frac{r}{c}\right)^2 G_m\right)\int_0^L \left(\frac{dv}{dx}\right)\left(\frac{d}{dx}\delta v\right) dx - \int_0^L s\delta v\end{aligned} \tag{4-108}$$

$$
\begin{aligned}
\delta U = E_f I_f & \left[\left(\frac{d^2v}{dx^2}\right)\left(\frac{d}{dx}\delta v\right)\right]_0^L \\
& - E_f I_f \int_0^L \left(\frac{d^3v}{dx^3}\right)\left(\frac{d}{dx}\delta v\right) dx \\
& + \left(-P + A_m\left(1+\frac{r}{c}\right)^2 G_m\right)\left[\left(\frac{dv}{dx}\right)\delta v\right]_0^L \\
& - \left(-P + A_m\left(1+\frac{r}{c}\right)^2 G_m\right)\int_0^L \left(\frac{d^2v}{dx^2}\delta v\right) dx - \int_0^L s\delta v \\
& = E_f I_f \left[\left(\frac{d^2v}{dx^2}\right)\left(\frac{d}{dx}\delta v\right)\right]_0^L - E_f I_f \left[\frac{d^3v}{dx^3}\delta v\right]_0^L \\
& + E_f I_f \int_0^L \left(\frac{d^4v}{dx^4}\delta v\right) dx \\
& + \left(-P + A_m\left(1+\frac{r}{c}\right)^2 G_m\right)\left[\left(\frac{dv}{dx}\right)\delta v\right]_0^L \\
& + \left(P - A_m\left(1+\frac{r}{c}\right)^2 G_m\right)\int_0^L \left(\frac{d^2v}{dx^2}\delta v\right) dx - [s\delta v]_0^L
\end{aligned}
\tag{4-109}
$$

$$
\begin{gathered}
E_f I_f \frac{d^4v}{dx^4} + \left(P - G_m A_m\left(1+\frac{r}{c}\right)^2\right)\frac{d^2v}{dx^2} = 0 \\
\frac{d^3v}{dx^3} + \frac{s}{E_f I_f} = 0
\end{gathered}
\tag{4-110}
$$

Applying the following boundary conditions [59]:

$$
\begin{aligned}
x = 0: &\qquad v = 0 \qquad \frac{dv}{dx} = 0 \\
x = L: &\qquad \frac{d^2v}{dx^2} = 0 \\
& E_f I_f \frac{d^3v}{dx^3} = -s
\end{aligned}
\tag{4-111}
$$

Depending on the sign of A in the following equation, the solution for v may vary.

$$A = P - A_m G_m \left(1 + \frac{r}{c}\right)^2 \tag{4-112}$$

If $A < 0$

$$v = \frac{s}{E_f I_f B_1^3} [\sinh B_1 L \cosh B_1 x - \cosh B_1 L \sinh B_1 x - \sinh B_1 L + B_1 x \cosh B_1 L] \tag{4-113}$$

$$B_1^2 = -\frac{A}{E_f I_f}$$

If $A > 0$

$$v = \frac{s}{E_f I_f B_2^3} [\sin B_2 L \cos B_2 x - \cos B_2 L \sin B_2 x - \sin B_2 L + B_2 x \cos B_2 L] \tag{4-114}$$

$$B_2^2 = \frac{A}{E_f I_f}$$

The composite will fail if the shear stress in the matrix is greater than its shear strength.

$$A < 0: \quad \tau_c = \frac{s G_m \left(1 + \frac{r}{c}\right)}{2 E_f I_f B_1^2} [\sinh(B_1 L) \sinh(B_1 n L) - \cosh(B_1 L) \cosh(B_1 n L) + \cosh(B_1 L)] \tag{4-115}$$

4.1.2.2.2. Region 2 – Fiber-Matrix Debonding

Fiber matrix debonding is based on shearing in the matrix or the fiber-matrix interface. Figure 4-21, generated from FEM analysis, shows the shear strain in the matrix material during material deformation. Ramesh et al. [64] claimed that the dominant failure mechanism in FRP is by matrix shearing. It can be assumed that crack development occurs along the fiber and matrix interface. In this study, it is assumed that the fiber does not shear.

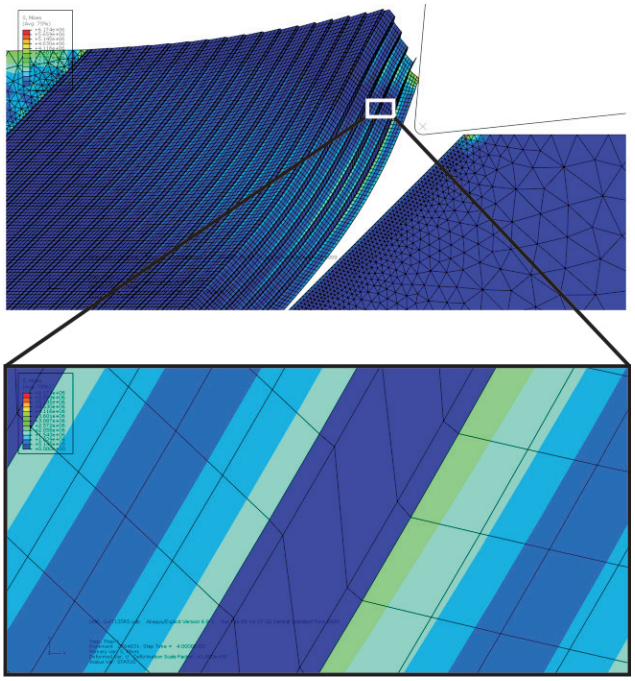

Figure 4-21. Matrix shearing during cutting process

The matrix material flow is such that after flowing, it slips on the rake face of the tool. Therefore, there is a change in the matrix material orientation because of shearing. This model does not consider friction between the chip and the rake face.

A more complicated model is one that reflects the effect of friction.

4.1.2.3. Analytical Model – Cutting Force

The cutting force is caused by two factors: tool nose radius and resistance of the fibers against bending. Each of these factors will be considered to calculate the cutting force. Knowing the force to calculate a single fiber, it is possible to determine the total force to bend a certain number of fibers.

Depending on fiber orientation, tool rake angle, and the workpiece material properties, three different models were proposed for the fiber bending.

$$\theta - 90 \leq \gamma$$

$$\theta - 90 \geq \gamma$$

Damage occurs due to fiber breakage rather than matrix shearing.

4.1.2.3.1. Bending Force When $\theta - 90 \leq \gamma$

When the fiber orientation relative to the rake angle of the tool falls into the range of $\theta - 90 \leq \gamma$, the fibers undergo bending due to the exerted cutting force. In this model, it is assumed that the chip forms by the tool nose before it slips onto the rake face of the tool. This means that the force applied by the tool bends the fibers and then the surrounding matrix shears. Figure 4-22 shows a schematic view of fibers bent as the result of cutting force.

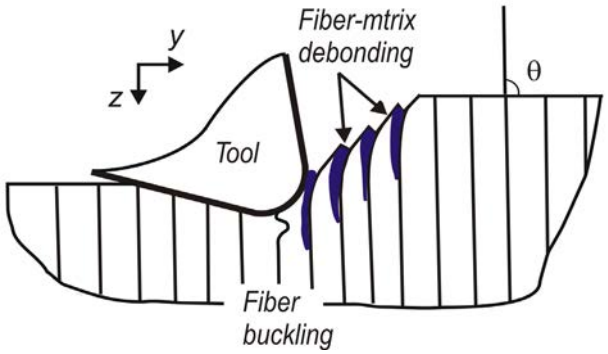

Figure 4-22. Fibers bending when $\theta - 90 \leq \gamma$

Two different factors produce the cutting force:

- Resistance of the fibers against bending.
- Microbuckling of the fibers due to the tool nose radius.

No force as the result of bouncing back of material was considered in this model, since this effect has already been reflected in fiber microbuckling calculations. The contribution of each of the above-mentioned factors depends on the tool geometry, material properties, fiber orientation, and machining parameters, such as depth of cut.

Consider a single fiber as shown in the Figure 4-23. If the lateral force *s* acts on this fiber, the deflection of the fiber is such that the total potential energy is minimized.

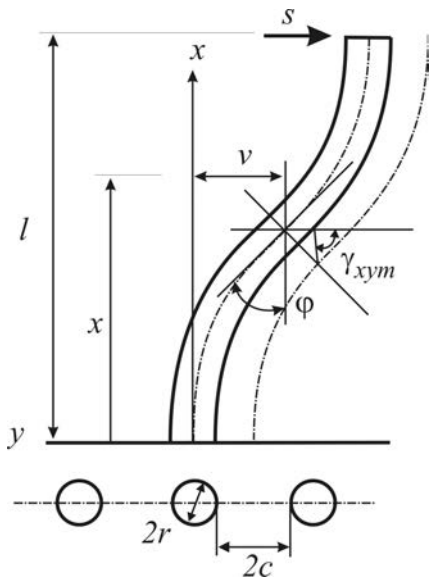

Figure 4-23. Schematic figure of single fiber under lateral force

This analysis is based on the following assumptions [59]:

- Two-dimensional deformation.
- No shear in the fiber.
- No matrix extension or compression.

- Normal stress in the fiber that produces no mechanical work during its deformation.

Under these assumptions and with reference to Figure 4-23,

$$\gamma_{xym}\, c = \frac{dv}{dx}(r + c) \tag{4-116}$$

$$\gamma_{xym} = \left(\frac{c + r}{c}\right)\frac{dv}{dx} \tag{4-117}$$

Following the same procedure as mentioned in section 4.1.2.2.1.3, the fiber deflection will be

$$\begin{aligned} v = \frac{s}{E_f I_f B_1^3}[&\sinh B_1 L \cosh B_1 x \\ &- \cosh B_1 L \sinh B_1 x - \sinh B_1 L + B_1 x \cosh B_1 L] \end{aligned} \tag{4-118}$$

$$B_1^2 = -\frac{A}{E_f I_f}$$

where

$$A = -A_m G_m \left(1 + \frac{r}{c}\right)^2 \tag{4-119}$$

The energy balance for a single fiber surrounded by the matrix material can be written as

$$U = -\int_0^L s\left(\frac{dv}{dx}\right)dx + \frac{1}{2}\int_0^L E_f I_f \left(\frac{d^2 v}{dx^2}\right)^2 dx + \frac{1}{2}\int_0^L A_m \tau_{xym}\, \gamma_{xym}\, dx \tag{4-120}$$

where the first term is the external work done by the lateral force s, the second term corresponds to the strain energy stored in the fiber, and the last term represents the strain energy stored in the matrix corresponding to one fiber.

If the debonding length L in equation (4-120) is known, then the bending force s for a single fiber can be calculated by solving the equation $U = 0$. However, the debonding length is unknown, and therefore another equation must be solved simultaneously with the energy equation.

It can be assumed that the composite material fails due to the excessive shear stress in the matrix material; however, for the chip to form, the material failure is not enough. When the chip forms, both fiber and matrix fail.

The following equation can be used to calculate the shear stress in the matrix at any given x coordinate along the fiber axis.

$$\tau_{xym} = G_m \left(1 + \frac{r}{c}\right) \frac{dv}{dx} \tag{4-121}$$

where v is the fiber deflection and can be calculated using equation (4-118).

The fiber deflection is such that it takes the maximum deflection and slope at the free end. On the other hand, there is a specific point along the fiber at which both the deflection and the slope are zero. If the distance of the point to the free end of the fiber along the fiber axis is L, then the shear stress at this point can be calculated using equation (4-121). The fiber can take a deflection such that the shear stress in the fixed point reaches the matrix shear strength. This deflection is cause by a lateral force s. Therefore, solving equations (4-120) and (4-121) simultaneously at $x = nL$, gives the length L and the lateral

force s, which cause the debonding of fiber-matrix interface due to excessive shear stress in the matrix material.

$$U = -\int_0^L s\left(\frac{dv}{dx}\right)dx + \frac{1}{2}\int_0^L E_f I_f \left(\frac{d^2v}{dx^2}\right)^2 dx + \frac{1}{2}\int_0^L A_m \tau_{xym}\,\gamma_{xym}\,dx = 0$$
$$\tau_{xym} = G_m\left(1+\frac{r}{c}\right)\frac{dv}{dx} = \tau_c \tag{4-122}$$

Here, s can be found by solving any of the equations. Using the second equation, which represents the shear stress distribution in the matrix along the fiber,

$$s^{shear} = -\tau_c \frac{E_f I_f B_1^3}{\dfrac{d[\sinh B_1 L\cosh B_1 x - \cosh B_1 L \sinh B_1 x - \sinh B_1 L + B_1 x \cosh B_1 L]}{dx}} \cdot \frac{1}{G_m(1+\frac{r}{c})} \tag{4-123}$$

Evaluating equation (4-123) at $x = nL$ and substituting it into equation (4-122) gives

$$\frac{2\tau_c E_f I_f B_1^2}{G_m\left(1+\frac{r}{c}\right)[\sinh(B_1 L)\sinh(B_1 nL) - \cosh(B_1 L)\cosh(B_1 nL) + \cosh(B_1 L)]}\int_0^L \left(\frac{dv}{dx}\right)dx + \frac{1}{2}E_f I_f \int_0^L \left(\frac{d^2v}{dx^2}\right)^2 dx + \frac{1}{2}G_m\left(1+\frac{r}{c}\right)A_m\int_0^L \left(\frac{dv}{dx}\right)^2 dx = 0 \tag{4-124}$$

The only unknown parameter in equation (4-124) is L, which is the fiber-matrix debonding length due to shearing in the matrix. This equation can be solved numerically.

Another failure mechanism is the excessive normal stress in the fiber that will result in fiber breakage. Maximum normal stress in the matrix should not exceed the fiber flexural strength. For this mechanism, s is

$$s^{bend} = -\frac{X_f B_1 I_f}{r(-\sinh(B_1 L)\cosh(B_1 x) + \cosh(B_1 L)\sinh(B_1 x))} \tag{4-125}$$

Evaluating equation (4-125)and substituting it into equation (4-122) gives

$$\frac{X_f B_1 I_f}{r(-\sinh(B_1 L)\cosh(B_1 x) + \cosh(B_1 L)\sinh(B_1 x)} \int_0^L \left(\frac{dv}{dx}\right) dx + \frac{1}{2} E_f I_f \int_0^L \left(\frac{d^2 v}{dx^2}\right)^2 dx + \frac{1}{2} G_m \left(1 + \frac{r}{c}\right) A_m \int_0^L \left(\frac{dv}{dx}\right)^2 dx = 0 \tag{4-126}$$

Equation (4-126) can also be solved numerically for L. The calculated L from this equation gives the length that the fibers tend to break due to excessive normal stress along the fibers.

L values from equations (4-124) and (4-126) should be substituted into equations (4-123) and (4-125) to find the maximum lateral force on each fiber resulting in both fiber and matrix failure. The total cutting force for this fiber orientation interval can be estimated by knowing the total number of fibers that resist against chip formation.

If a cylindrical shape for the fibers is considered, then parameter $2c$ depends on the fiber volume fraction v_f and fiber packing. Fiber packing can be square, hexagonal, or any other packing. Figure 4-24 shows fiber spacing for square fiber packing and how parameter $2c$ can be calculated for this particular fiber packing.

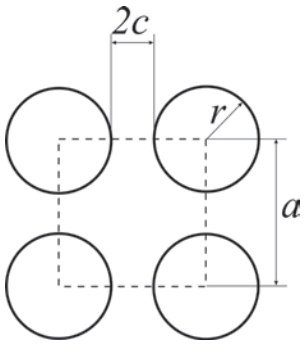

Figure 4-24. Fiber spacing for square fiber packing

$$v_f = \frac{\pi r^2}{a^2} \tag{4-127}$$

$$a = r\sqrt{\frac{\pi}{v_f}} \tag{4-128}$$

$$2c = a - 2r = r\left(\sqrt{\frac{\pi}{v_f}} - 2\right) \tag{4-129}$$

Therefore,

$$A = -A_m G_m \left(1 + \frac{r}{c}\right)^2 = -\frac{1}{2} A_m G_m \left(\frac{\sqrt{\frac{\pi}{v_f}} - 1}{\sqrt{\frac{\pi}{v_f}} - 2}\right) \tag{4-130}$$

and

$$B_1^2 = -\frac{A}{E_f I_f} \tag{4-131}$$

where

$$I_f = \frac{\pi r^4}{4} . \frac{h}{a} \tag{4-132}$$

Since the total potential energy balance should be written for the volumetric element of the material, the factor h/a in I_f takes care of the number of fibers along the thickness.

A_m in equations (4-120), (4-122), and (4-130) represents the matrix cross-sectional area associated with one fiber (Figure 4-24).

The calculated L from equations (4-124) and (4-128) along with equations (4-123) and (4-125) can be used to compute the lateral force needed to form chips:

$$A_m = a^2 - \pi r^2 \tag{4-133}$$

Comparisons show that the two-dimensional model, representing fiber and matrix as thin blocks, gives better results compared to the cylindrical model of fibers when matrix material fills the remaining space.

4.1.2.3.2. Bending Force When $\theta - 90 \geq \gamma$

When $\theta - 90 \geq \gamma$, more shearing occurs in the matrix material, and the material fails because of either extensive shear in the matrix or fiber breakage. All of the assumptions mentioned in section 4.1.2.3.1 are applicable to the case of $\theta - 90 \geq \gamma$. In addition, it is assumed that the fibers and matrix slip on the rake face of the tool after chip formation. Therefore, according to Figure 4-25, the slope at the free end of the fibers will be

$$x = L: \qquad \frac{dv}{dx} = \theta - \frac{\pi}{2} - \gamma \tag{4-134}$$

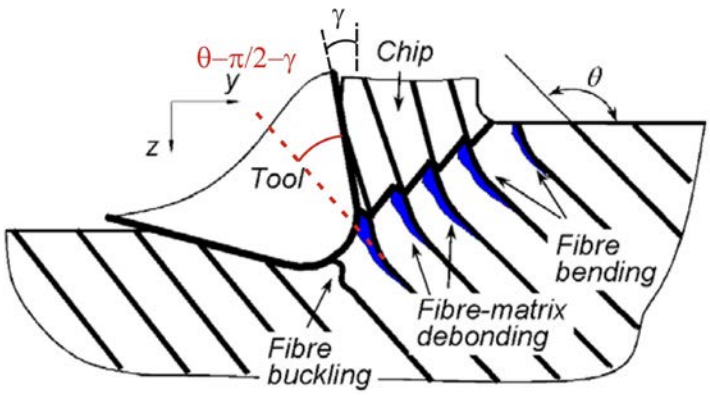

Figure 4-25. Fibers bending when

It is assumed that the matrix material behavior is elastic-perfectly plastic [65]. Therefore, the fracture stress cannot be used in the debonding length and force calculations; instead, fracture strain was used. Figure 4-26 shows the elastic-perfectly plastic behavior of the epoxy matrix used for this study.

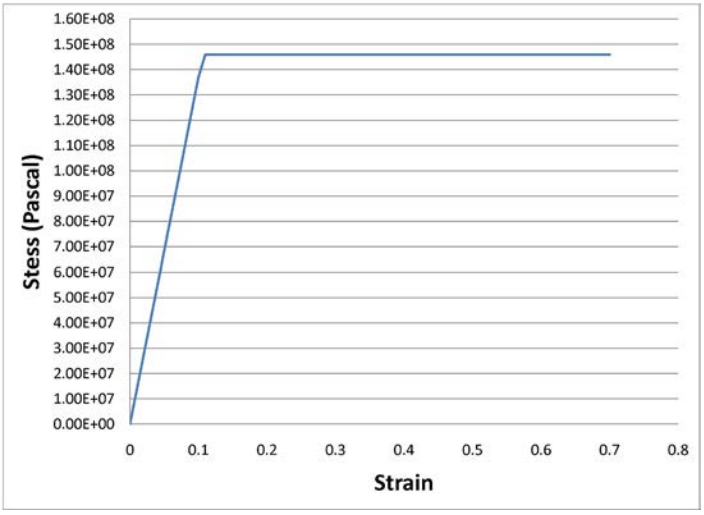

Figure 4-26. Elastic -Plastic behavior of epoxy resin

The total potential energy and the shear stress in the matrix for this case are different and are given as

$$U = -\int_0^L s^{shear}\left(\frac{dv}{dx}\right)dx + \frac{1}{2}\int_0^L E_f I_f \left(\frac{d^2v}{dx^2}\right)^2 dx + A_m\left(-\frac{L\tau_c^2}{2G_m} + \tau_c\left(1+\frac{r}{c}\right)\int_0^L \frac{dv}{dx}dx\right) = 0 \qquad (4\text{-}135)$$

Using the principal of virtual work

$$\frac{d^2}{dx^2}\left(E_f I_f \frac{d^2v}{dx^2}\right) = 0 \qquad (4\text{-}136)$$

and the following boundary conditions

$$\begin{aligned} x = 0: &\qquad v = 0 \qquad \frac{dv}{dx} = 0 \\ x = L: &\qquad \frac{dv}{dx} = \theta - \frac{\pi}{2} - \gamma \\ &\qquad E_f I_f \frac{d^3v}{dx^3} = -s^{shear} \end{aligned} \qquad (4\text{-}137)$$

From the boundary conditions above, it is clear that equation (4-122) cannot be used as the total potential energy for this case, since the generated essential boundary condition at $x = L$ will not be satisfied.

Deflection of the beam can be written as

$$v = \frac{1}{12}\frac{x^2}{LE_f I_f}\left(-2s^{shear}xL + 6\left(\theta - \frac{\pi}{2} - \gamma\right)E_f I_f + 3s^{shear}L^2\right) \qquad (4\text{-}138)$$

It is assumed that the fiber at the free end slips on the rake face of the tool. Therefore, the fiber slope at that point will be the rake angle of the tool in the fiber coordinate system. The fiber coordinate system is such that the x axis is along the fiber. Equation (4-137) shows the fiber slope at $x = L$.

Using equation (4-138), the shear strain in the matrix along the fiber can be written as

$$\gamma_{xym} = \frac{dv}{dx}\left(1+\frac{r}{c}\right) = -\frac{1}{2}\frac{x}{E_f I_f L}\left(s^{shear} xL - 2\left(\theta - \frac{\pi}{2} - \gamma\right)E_f I_f - sL^2\right)\left(1+\frac{r}{c}\right) \tag{4-139}$$

Solving the above equation for s^{shear}

$$s^{shear} = -\frac{2E_f I_f\left[-x\left(\theta - \frac{\pi}{2} - \gamma\right) + \gamma_{xym} L\left(\frac{c}{r+c}\right)\right]}{xL(x-L)} \tag{4-140}$$

Evaluating equation (4-140) at $x = nL$ and substituting it into (4-135)

$$\begin{aligned}\frac{2E_f I_f\left[n\left(\theta - \frac{\pi}{2} - \gamma\right) - \gamma_{xym}\left(\frac{c}{r+c}\right)\right]}{L^2 n(1-n)}\int_0^L \left(\frac{dv}{dx}\right)dx \\ + \frac{1}{2}\int_0^L E_f I_f\left(\frac{d^2v}{dx^2}\right)^2 dx \\ + A_m\left(-\frac{L\tau_c^2}{2G_m} + \tau_c\left(1+\frac{r}{c}\right)\int_0^L \frac{dv}{dx}dx\right) = 0\end{aligned} \tag{4-141}$$

The only unknown in equation (4-141) is L, which is the fiber-matrix debonding length due to the excessive shear strain in the matrix. The interesting characteristic of this

method is the dependency of the debonding length and cutting force on the fiber orientation as well as the tool rake angle.

As previously explained, the composite may also fail due to fiber bending and fracture. If the normal stress in a single fiber exceeds the flexural strength of the fiber material, then the fiber will break and a chip will form. Using the fiber deflection equation, it is possible to calculate normal stress in the fiber. The maximum stress along the fiber will occur at the fixed end of the fiber ($x = 0$).

$$\sigma = \frac{Mr}{I_f}$$
$$M = E_f I_f \frac{d^2 v}{dx^2} \tag{4-142}$$

Therefore, the maximum normal stress at the fiber cross section along its axis can be determined as

$$\sigma_f^{max} = -r.\left[\frac{s^{bend}\, x}{I_f} - \left(\theta - \frac{\pi}{2} - \gamma\right)\frac{E_f}{L} - \frac{s^{bend}\, L}{I_f}\right] \tag{4-143}$$

Hence, the lateral force needed to break the fiber at the fixed end can be written by substituting $x = 0$ and $\sigma_f^{max} = X_f^c$:

$$s^{bend} = \frac{2\left[-rE_f\left(\theta - \frac{\pi}{2} - \gamma\right) + X_f^c L\right] I_f}{L^2 r} \tag{4-144}$$

Equations (4-144) and (4-135) can be used to calculate the material failure due to fiber breakage as

$$-\frac{2\left[-rE_f\left(\theta-\frac{\pi}{2}-\gamma\right)+X_f^c L\right]I_f}{L^2 r}\int_0^L\left(\frac{dv}{dx}\right)dx + \frac{1}{2}\int_0^L E_f I_f\left(\frac{d^2v}{dx^2}\right)^2 dx+\frac{1}{2}LA_m G_m\left(\theta-\frac{\pi}{2}-\gamma\right)^2=0 \quad (4\text{-}145)$$

The two L values found from equations (4-141) and (4-145) should be used to calculate the corresponding lateral forces. The one resulting in the greater lateral force should be picked as the debonding length, and the corresponding force will be the cutting force perpendicular to the fiber axis. This cutting force should be projected to the cutting direction to find the contribution of fiber bending and fiber-matrix debonding in the cutting force. The concept of material failure is different from cutting. The material fails if at any point the minimum requirement for the failure is met; however, during cutting, a chip forms if all of the active failure mechanisms meet the failure criterion. This explains why the greater lateral force should be chosen as the cutting force.

4.1.2.3.3. Total Machining Forces

The cutting force determined thus far is the force generated by only one fiber. Since almost the same force is needed to form a chip, the number of fibers in one chip should be known to compute the total cutting force. As shown in Figure 4-27, fibers break due to excessive bending, and it can be assumed that their breakage occurs along a straight line that makes an angle of ϕ with the workpiece surface. In addition, since the shear force acting on the different layers of matrix is the same, it is assumed that the fiber-matrix

debonding length along the interface is the same for all affected layers. It is possible to find angle ϕ by minimizing the total potential energy with respect to ϕ.

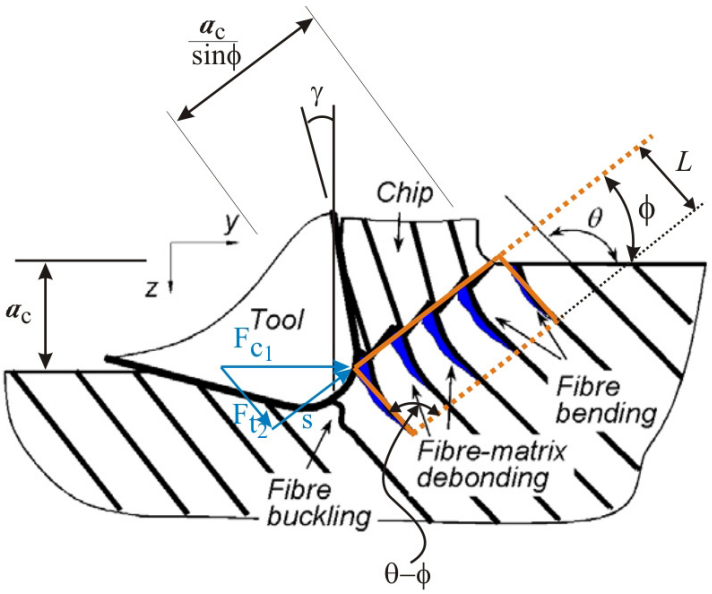

Figure 4-27. Shear stress and strain caused by machining

The number of representative volume elements (RVEs) along the shear plane is $\frac{a_c.\sin(\theta-\phi)}{r.\sin\phi}$. Therefore, the total potential energy for the whole chip will be in the form of equation (4-146).

$$U = -\int_0^L s\left(\frac{dv}{dx}\right)dx + \frac{1}{2}\frac{a_c.\sin(\theta-\phi)}{r.\sin\phi}.v_f\int_0^L E_f I_f\left(\frac{d^2v}{dx^2}\right)^2 dx + \frac{1}{2}\frac{a_c.\sin(\theta-\phi)}{r.\sin\phi}.c.t.v_m\int_0^L \tau_{xym}\gamma_{xym}\,dx \quad (4\text{-}146)$$

Minimizing U with respect to ϕ

$$\frac{dU}{d\phi} = 0 \tag{4-147}$$

Therefore,

$$\frac{d\left[\frac{\sin(\theta-\phi)}{\sin\phi}\right]}{d\phi} = 0 \tag{4-148}$$

$$\sin(\theta - 2\phi) = 0 \rightarrow \phi = \frac{\theta}{2} \tag{4-149}$$

Using equation (4-149), it is possible to find the number of RVEs in a chip:

$$n_{RVE} = \frac{a_c.\sin(\theta-\phi)}{r\sin\phi} = \frac{a_c.\sin\left(\theta-\frac{\theta}{2}\right)}{r\sin\frac{\theta}{2}} = \frac{a_c}{r} \tag{4-150}$$

Therefore, the total cutting force can be calculated by adding the cutting force caused by the tool nose radius and the cutting force caused by fiber bending and matrix shearing:

$$F_c = F_{c_1} + F_{c_2} + F_{c_3} \tag{4-151}$$

$$F_{c_1} = -G_{LT} r_e \left(\theta - \frac{\pi}{2}\right)\cos\theta \tag{4-152}$$

$$F_{c_2} = \frac{\max(|s^{shear}|, |s^{bend}|)}{\cos\gamma}.n_{RVE}$$
$$= \frac{\max\left(\left|-\frac{2E_f I_f\left[-x\left(\theta-\frac{\pi}{2}-\gamma\right)+\gamma_{xym}L\left(\frac{c}{r+c}\right)\right]}{xL(x-L)}\right|, \left|\frac{2\left[-rE_f\left(\theta-\frac{\pi}{2}-\gamma\right)+X_f^c L\right]I_f}{L^2 r}\right|\right)}{\cos\gamma}.n_{RVE} \quad (4\text{-}153)$$

$$F_{c_3} = F_{c_2}.\mu.\sin\gamma \quad (4\text{-}154)$$

The total cutting force will be

$$F_c = -G_{LT}r_e\left(\theta-\frac{\pi}{2}\right)\cos\theta$$
$$+\frac{\max\left(\left|-\frac{2E_f I_f\left[-x\left(\theta-\frac{\pi}{2}-\gamma\right)+\gamma_{xym}L\left(\frac{c}{r+c}\right)\right]}{xL(x-L)}\right|, \left|\frac{2\left[-rE_f\left(\theta-\frac{\pi}{2}-\gamma\right)+X_f^c L\right]I_f}{L^2 r}\right|\right)}{\cos\gamma}.n_{RVE}.(1$$
$$+\mu.\sin\gamma) \quad (4\text{-}155)$$

Figure 4-28 proves that the shear plane takes approximately the angle predicted by equation (4-149). In addition, looking at the high extreme of the fiber orientation angle of 180°, it can be confirmed that according to the same equation, the number of RVEs in a chip should be a_c/r, which is true for that orientation.

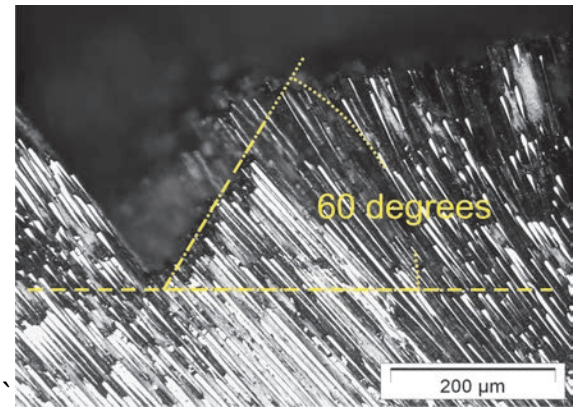

Figure 4-28. Shear plane for fiber orientation $\theta = 135°$, Rake angle = 10°, and Relief angle = 6°

The same method will be used to calculate the total machining forces for the case of $\theta - 90 < \gamma$. The shear plane angle will take the angle of $\theta/2$, and the total cutting force considering the friction will be

$$F_c = -G_{LT} r_e \left(\theta - \frac{\pi}{2}\right) \cos\theta + \max(|s^{shear}|, |s^{bend}|) \, . \, n_{RVE} \tag{4-156}$$

where s^{shear} and s^{bend} can be calculated form equations (4-123) and (4-125), respectively.

The friction force on the rake face and tool nose affects the thrust force computed from equation (4-98). The total thrust force is as follows:

For $\theta - 90 < \gamma$:

$$F_t = F_{t_1} + \mu F_c = G_{LT} r_e \left(\theta - \frac{\pi}{2}\right) \sin\theta - \mu \left(-G_{LT} r_e \left(\theta - \frac{\pi}{2}\right) \cos\theta + \max(|s^{shear}|, |s^{bend}|) \, . \, n_{RVE}\right) \tag{4-157}$$

For $\theta - 90 \geq \gamma$:

$$F_t = G_{LT} r_e \left(\theta - \frac{\pi}{2}\right) \sin\theta - \max(|s^{shear}|, |s^{bend}|) \tan\gamma \, n_{RVE}$$

$$= G_{LT} r_e \left(\theta - \frac{\pi}{2}\right) \sin\theta$$

$$- \max\left(\left| -\frac{2E_f I_f \left[-x\left(\theta - \frac{\pi}{2} - \gamma\right) + \gamma_{xym} L \left(\frac{c}{r+c}\right)\right]}{xL(x-L)} \right| , \left| \frac{2\left[-rE_f\left(\theta - \frac{\pi}{2} - \gamma\right) + X_f^c L\right] I_f}{L^2 r} \right| \right) \tan\gamma \, . \, n_{RVE} \quad (4\text{-}158)$$

CHAPTER 5

EXPERIMENTAL WORK

5.1. Setup

A $2\frac{1}{2}$ inch $\times$ 9 inch unidirectional carbon fiber composite strip was used for the experiments in this research. The composite coupon was securely fixed on a swivel-based vise, which was attached to a KISTLER 9272 dynamometer. An adaptor was designed and used to attach the vise to the dynamometer.

The dynamometer readings were transferred to a National Instruments (NI) data acquisition (DAQ) card after being amplified by 5010B KISTLER dual-mode amplifiers. VILogger LabVIEW 8.0 registered the received signals with a frequency of 500 Hz. The DAQ card used was NI–6023E. Before using the DAQ card for the experiments, it was calibrated. The calibration had two steps: one for calibrating the voltage readings and the other to convert the voltage to the desired physical quantity. Thrust and cutting forces were calibrated with standard weights and hanging scale, respectively, and the torque was calibrated with a precise torque wrench [66-69]. Figure 5-1 shows the setup used for the experiments. The orientation of the cutting and thrust forces respect to the dynamometer coordinate system is shown in Figure 5-2.

5.2. Methodology

A customized tool was designed to use for the experiments on a CNC milling machine. All of the cutting edges had the same geometry. The tool was attached to the spindle of the machine using a tool holder. Because the purpose here was to do an orthogonal cutting on a CNC milling machine, it was important that the tool not rotate. This

was achieved using an M19 code on the CNC machine. This code provides feedback control for the spindle in order to keep it stationary. It also reorients the spindle in the same direction any time the code is run. Hence, to maintain the desired rake and relief angles relative to the cutting direction, the tool should be fit in the tool holder with the correct orientation.

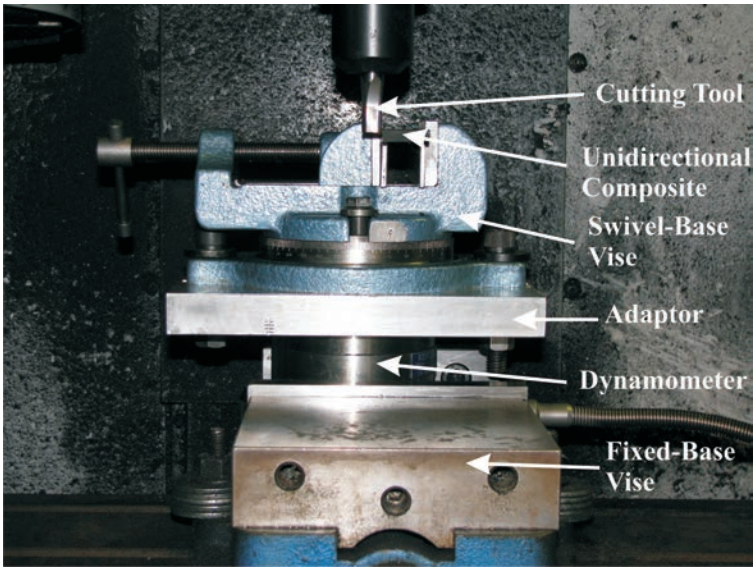

Figure 5-1. Setup used for the experiments

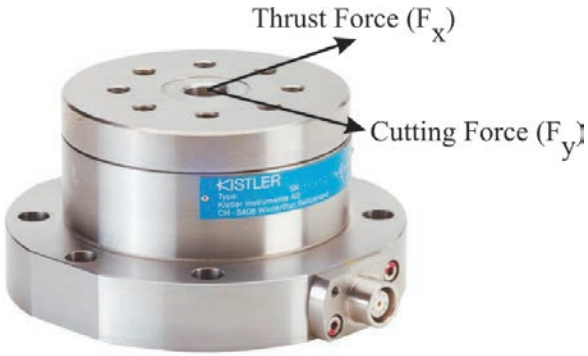

Figure 5-2. Cutting and thrust force orientations respect to the dynamometer coordinate system [68]

Figure 5-3 shows the spindle orientation after using the CNC milling machine M19 code.

Figure 5-3. Spindle reorientation with M19 code

Figure 5-4 shows how the cutting tool should be oriented in the tool holder to maintain the desired rake and relief angles for the orthogonal cutting experiments. According to the figure, the white lines connecting the tool corners should be parallel to either the x or y axis of the machine.

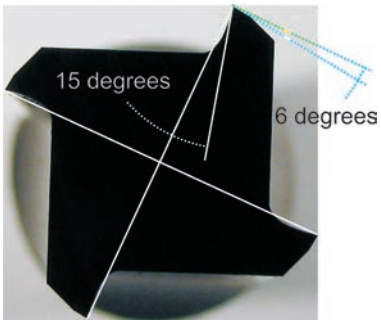

Figure 5-4. Customized tool used for experiments

Another important point is to maintain constant depth of cut along both the x and y axes. Changing the depth of cut can significantly affect the machining forces. Therefore,

each time the experiment is run, the top and side of the workpiece should be controlled using a dial indicator to ensure that they are parallel to the machine axes (Figure 5-5). It is assumed that there was no damage in the composite coupon each time the machining experiment was run. In addition, the tool nose radius was assumed to remain unchanged during the experiments. The experimental test matrix is shown in Table 5-1.

Figure 5-5. Controlling top of workpiece using dial indictor

TABLE 5-1

EXPERIMENTAL TEST MATRIX

Fiber Orientation (θ)	Tool Rake Angle (γ)	Fiber orientation (θ)	Tool Rake Angle (γ)
90°	5°	**90°**	15°
115°	5°	**115°**	15°
135°	5°	**135°**	15°
170°	5°	**170°**	15°
90°	10°	**90°**	20°
115°	10°	**115°**	20°
135°	10°	**135°**	20°
170°	10°	**170°**	20°

Feed rate was kept the same, at 5.9 mm/sec for all of the experiments. In addition, in-plane depth and width of the cut was 0.1 mm and 1.0 mm, respectively for the tests (Figure 5-6).

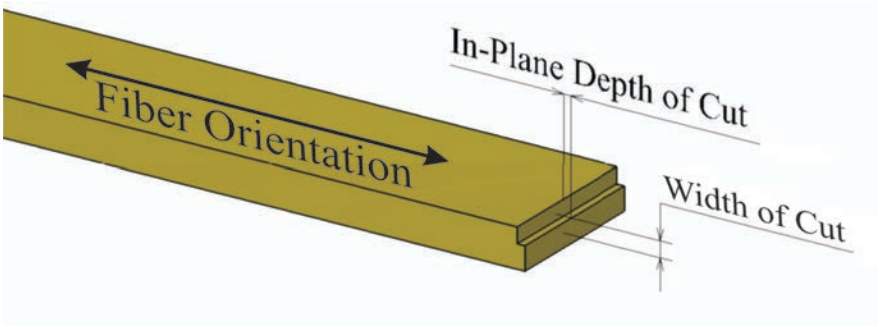

Figure 5-6. Width and in-plane depth of cut definitions

Figure 5-7 shows a sample of measured machining forces in orthogonal cutting of a composite coupon when $\theta = 170°$.

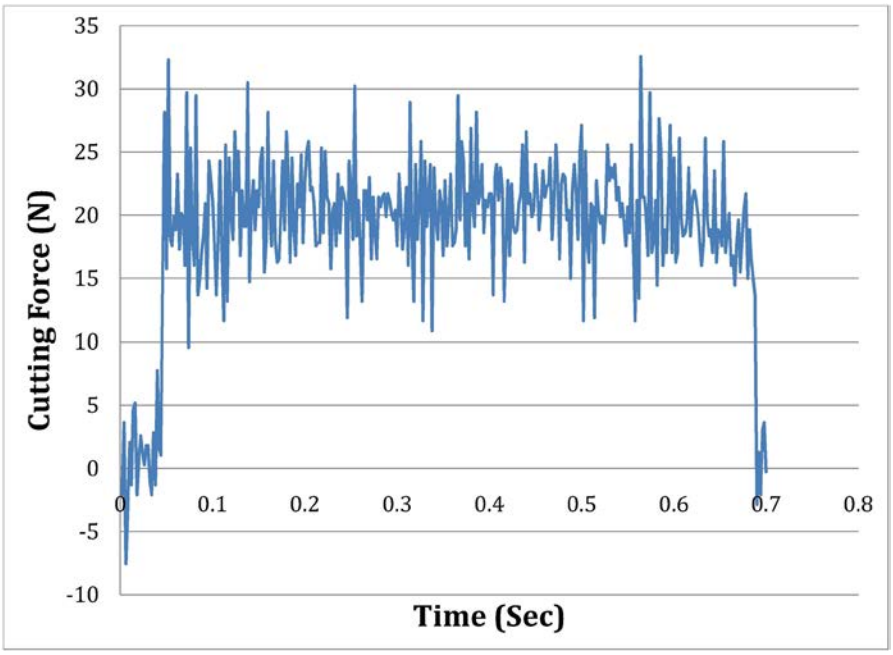

Figure 5-7. Sample of measured cutting force for $\theta = 170°$, $\gamma = 5°$, and $\alpha = 9°$

CHAPTER 6

ANALYTICAL PREDITIONS OF THRUST AND CUTTING FORCES

In this chapter, the predicted forces and debonding lengths from the analytical model are compared to those obtained from the FEM model and the literature. In addition, using a different material, the calculated force from the analytical model is compared to the experimental results. In order to use the proposed analytical model, several input parameters of the material, cutting tool, and machining condition should be provided. The parameters needed are listed in Table 6-1.

TABLE 6-1

FACTORS AFFECTING MACHINING QUALITY

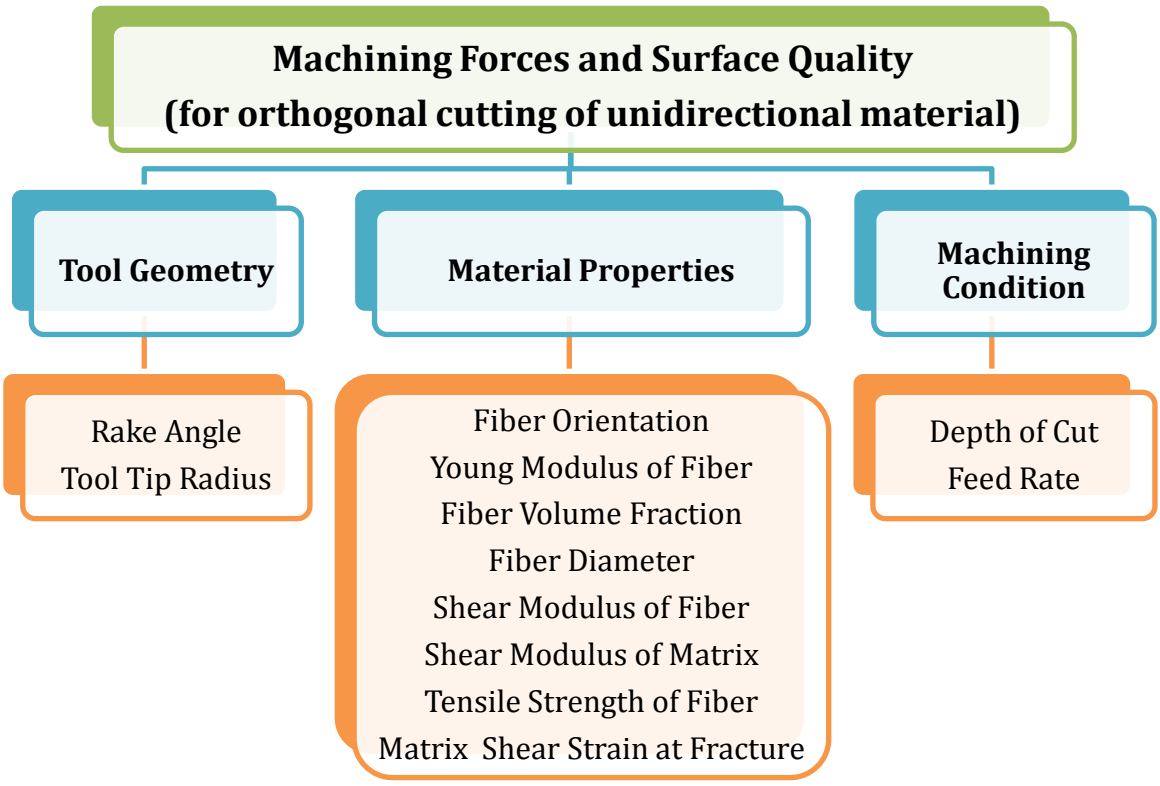

6.1. Material Properties

Most of the material properties listed in Table 6-1 are not available as individual properties of either the fiber or the matrix and should be calculated using the apparent mechanical properties of the composite. Fiber volume fraction is one essential parameter that must be determined in order to calculate the mechanical properties of the components. This can be found by looking at the cross section of the composite material under microscope.

The composite material used in this research was NCT 321/G150 (NASS) Unitape [70]. Table 6-2 shows a list of apparent composite properties in 0° and 90° orientation. These properties can be used to calculate the individual material properties.

TABLE 6-2

APPARENT PROPERTIES OF NCT 321/G150 (NASS) UNITAPE [70]

	Room Temperature Data			
	B-Basis (US Units)	Mean (US Units)	B-Basis (SI Units)	Mean (SI Units)
X_t	251.40 (ksi)	282.82 (ksi)	1.73 (GPa)	1.94 (GPa)
E_1^t	– –	17.76 (Msi)	– –	122.5 (Gpa)
ν_{12}	– –	0.321	– –	0.321
Y_t	5.95 (ksi)	7.06 (ksi)	41 (MPa)	48.6 (MPa)
E_2^t	– –	1.17 (Msi)	– –	8 (GPa)
X_c	139.20 (ksi)	165.80 (ksi)	959 (MPa)	1.14 (GPa)
E_1^c	– –	17.73 (Msi)	– –	122 (GPa)
Y_c	28.30 (ksi)	32.37 (ksi)	195 (MPa)	223 (MPa)
E_2^c	– –	1.63 (Msi)	– –	11.2 (GPa)
S_{12}	19.76 (ksi)	21.02 (ksi)	136 (MPa)	145 (MPa)
G_{12}	– –	0.55 (Msi)	– –	3.79 (GPa)
S_{13}	12.59 (ksi)	13.12 (ksi)	86.7 (Mpa)	90 (MPa)

Figure 6-1 shows the cross section of the composite used. The fiber volume fraction of the material was calculated by taking the average of three different measurements from different positions.

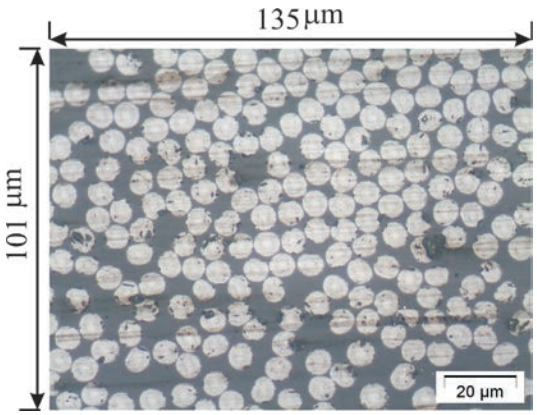

Figure 6-1. Cross section of composite material used to calculate fiber volume fraction

The other individual material mechanical properties can be calculated as shown below, using the data provided by Newport Adhesives and Composites, Inc. [71].

The v_f for this material is 0.65. Therefore, using rule of the mixtures and considering the fiber direction as direction 1

$$E_1 = v_f E_f + v_m E_m$$
$$17.76 = 0.65E_f + 0.35E_m \tag{6-1}$$

$$E_2 = \frac{E_f E_m^{'}}{v_f E_m^{'} + 0.35E_f}$$

$$E_m^{'} = \frac{E_m}{1 - v_m^2} \tag{6-2}$$

$$1.17 = \frac{E_f E_m}{0.65E_m + 0.35(1 - 0.35^2)E_f} = \frac{E_f E_m}{0.65E_m + 0.3E_f}$$

Calculating E_f and E_m using equations (6-1) and (6-2)

$$E_f = 27.12\ Msi = 186\ GPa$$
$$E_m = 0.36\ Msi = 2.5\ GPa \tag{6-3}$$

From the mechanics of material, it is known that

$$G_f = \frac{E_f}{2(1+\nu)} \approx \frac{186\ GPa}{2(1+0.3)} = 71.5\ GPa \tag{6-4}$$

and G_m can be calculated using the rule of the mixtures:

$$3.79 = \frac{71.5G_m}{71.5 \times 0.35 + 0.65G_m}$$
$$G_m = 1.37\ GPa \tag{6-5}$$

A list of material properties used for both matrix and fiber is shown in Table 6-3. These values are estimated mechanical properties based on the composite's apparent properties.

TABLE 6-3

LIST OF MATERIAL PROPERTIES USED FOR ANALYTICAL CALCULATIONS [71]

Width of cut (H)	$1\ mm$	Fiber flexural strength (X_f)	$4.0\ GPa$
In-plane depth of cut (t)	$0.1\ mm$	Matrix fracture strain (ϵ_m)	0.10
Fiber diameter (d_f)	$6.9\ \mu m$	Matrix shear strength (S_m)	$146\ MPa$
Fiber volume fraction (v_f)	0.65	Matrix shear modulus (G_m)	$1.37\ GPa$
Fiber Young modulus (E_f)	$186\ GPa$		

To find the fiber and matrix strength, the rule of mixtures can be used [72]:

$$X_t = v_f F_b + v_m \bar{\sigma}_m$$
$$2 \times 10^9 = 0.65 F_b + 0.35 \bar{\sigma}_m \tag{6-6}$$

In equation (6-6), $\bar{\sigma}_m$ is the average matrix stress and can be ignored. Therefore, the approximate fiber bundle strength will be

$$F_b \approx \frac{2 \times 10^9}{0.65} = 3\ GPa \tag{6-7}$$

The fiber strength is much higher than the bundle strength, especially when the fiber length is very small. This is because there are fewer imperfections in fiber that are smaller in length [73]. In this study, the fiber flexural strength was assumed to be at least 2.5 times the fiber bundle strength. The matrix shear strength was estimated to be the same as the composite shear strength, since it can be assumed that the fiber does not shear.

6.2. Machining Forces

Figure 6-2 shows the predicted machining forces using the analytical method for $\gamma = 5°$. As can be seen, there is a discontinuity in the cutting force, which is due to the change in the deformation mechanism. As discussed previously, when the fiber orientation is greater than 90°, the fiber slips on the tool rake face; however, for the smaller fiber orientations, the free end boundary condition is different.

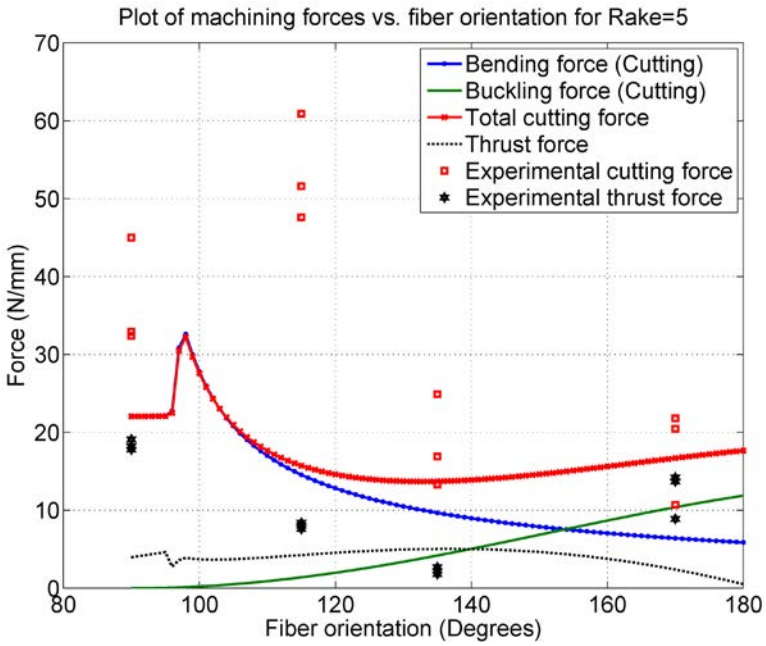

Figure 6-2. Predicted and experimental cutting and thrust forces using material properties of tested composite listed in Table 6-3

Any force value in Table 6-4 and Table 6-5 indicates an average over the time for a single experiment with corresponding fiber orientation and tool rake angle.

TABLE 6-4

CUTTING FORCE VALUES FROM EXPERIMENTS (ALL FORCE VALUES IN [N])

Rake Angle / Orientation	5°	10°	15°	20°
90°	32.5, 32.9, 45.3	20.9, 25.8, 42.3	35.0, 29.8, 43.0	25.9, 41.0, 32.9
115°	51.6, 60.9, 47.6	47.2, 48.9, 61.4	53.3, 58.7, 33.8	56.9, 52.0, 43.6
135°	13.3, 16.9, 24.9	12.9, 17.8, 15.6	16.8, 21.3, 16.0	15.1, 16.8, 19.1
170°	10.7, 20.5, 21.8	15.6, 18.7, 17.8	9.8, 14.4, 17.4	11.1, 13.3, 12.9

In Figure 6-2, *bending force* represents the portion of the cutting force caused by the bending of the fibers and fiber-matrix debonding, and the *buckling force* is an additional part of the cutting force due to the tool nose radius. The summation of these two forces represents the total cutting force.

TABLE 6-5

THRUST FORCE VALUES FROM EXPERIMENTS (ALL FORCE VALUES ARE IN [N])

Rake Angle / **Orientation**	**5°**	**10°**	**15°**	**20°**
90°	17.8, 18.2, 19.1	10.7, 12.9, 14.7	11.4, 9.9, 9.9	16.9, 16.2, 10.4
115°	8.4, 8.0, 7.6	4.9, 4.0, 5.3	3.6, 3.1, 2.7	3.1, 3.1, 3.1
135°	2.2, 1.8, 2.7	2.2, 2.2, 2.7	1.8, 2.2, 1.9	1.3, 1.0, 1.2
170°	8.9, 13.8, 14.2	10.2, 2.2, 11.6	6.2, 8.2, 9.2	8.4, 9.1, 10.2

Figure 6-3 shows the predicted cutting and thrust forces for $\gamma = 10°$. Here, the predicted values and the experiments are in a good agreement, and the trend of predicted forces is the same as experimental values. Figure 6-4 shows that at the higher fiber orientations (for $\gamma = 15°$), the error is more. However, the predicted bending value is very close to the experimental value. As the fiber orientation increases, the fibers will be closer to the free edges of the material. In this case, the fiber microbuckling theory will predict the values with more error.

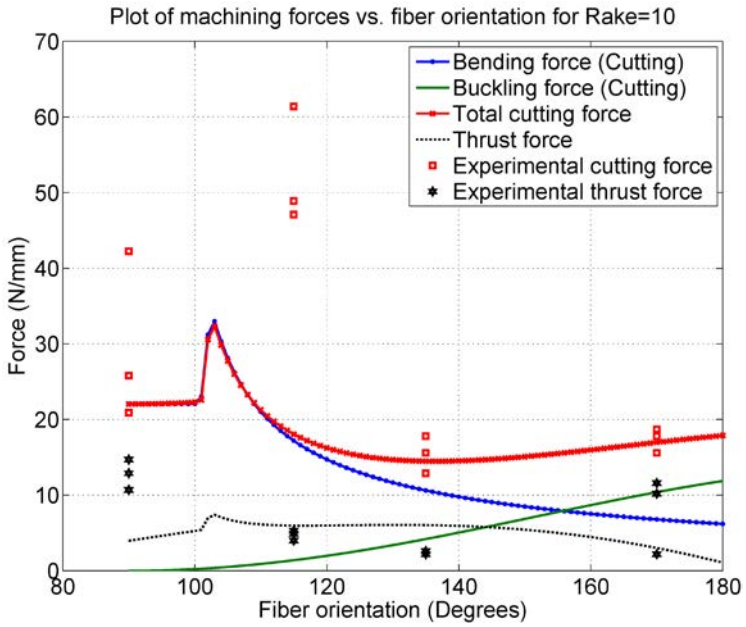

Figure 6-3. Predicted and experimental cutting and thrust forces using material properties of tested composite listed in Table 6-3

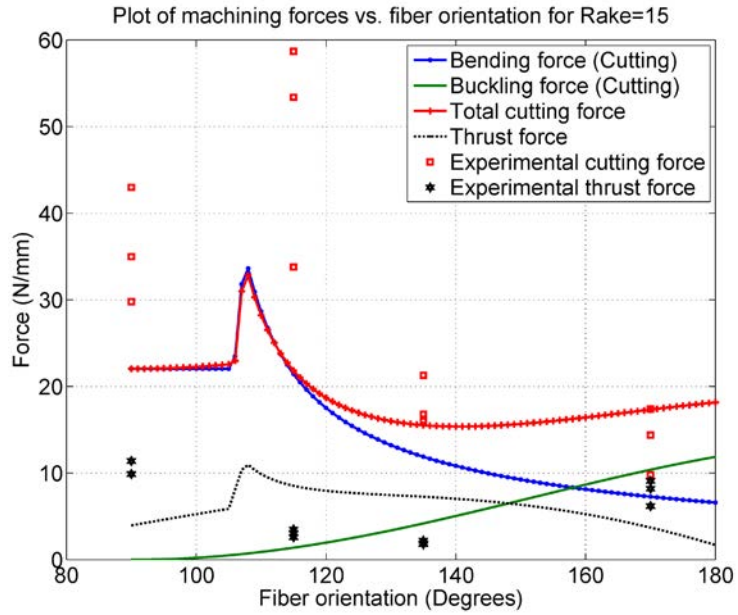

Figure 6-4. Predicted and experimental cutting and thrust forces using material properties of tested composite listed in Table 6-3

Figure 6-5 represents predicted cutting and thrust forces for $\gamma = 20°$.

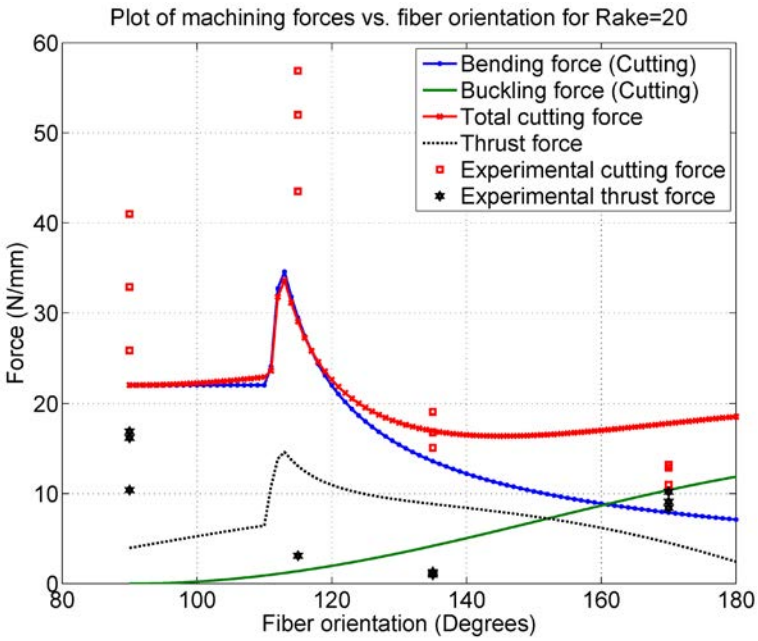

Figure 6-5. Predicted and experimental cutting and thrust forces using material properties of tested composite listed in Table 6-3

Figure 6-6 shows the effect of tool rake angle on the cutting and thrust forces. Unexpectedly, it shows the bigger the rake angle the higher machining forces. However, in meal cutting bigger rake angles generate less machining forces. This can be explained with the chip formation mechanisms for fiber orientation $0° \leq \theta \leq 90°$ which is based on matrix shearing and fiber breakage. The fibers break under lower force, when they are pushed normal to the fibers or at angles closer to that.

It is expected that as the flexural strength of the fibers gets weaker, the cutting force decreases. Figure 6-7 shows this trend as expected. As can be seen, the effect of flexural strength is greater for the smaller-fiber orientations. More cutting force results in more

friction force on the rake face, which increases that portion of the thrust force caused by friction.

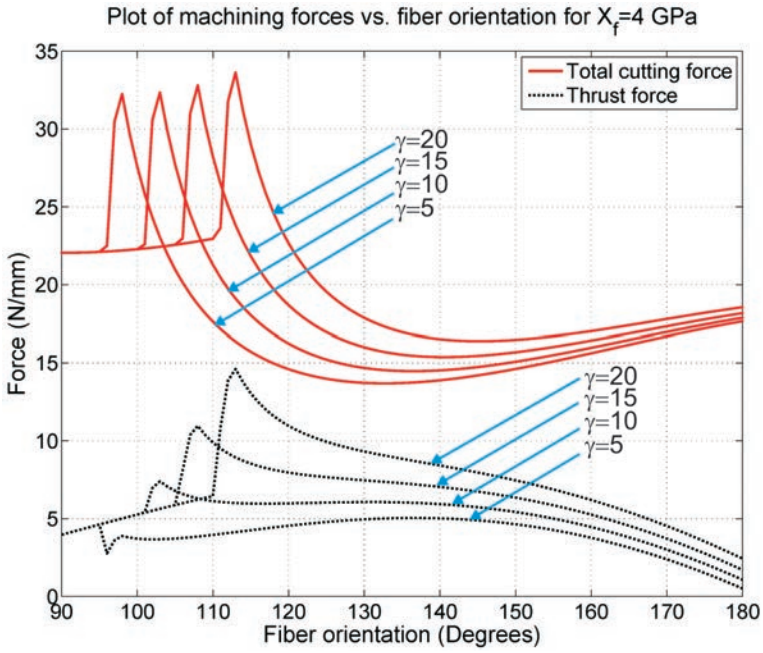

Figure 6-6. Effect of rake angle of cutting tool on cutting and thrust forces

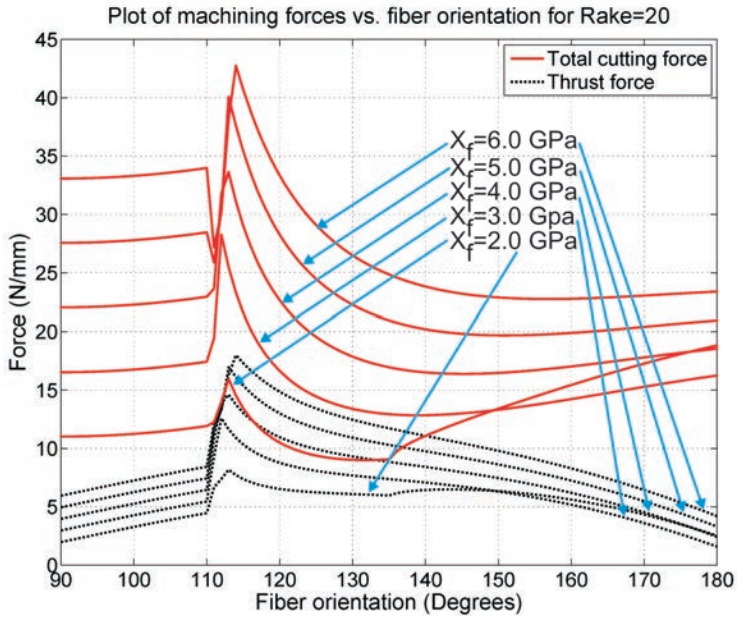

Figure 6-7. Effect of fiber flexural strength on cutting and thrust forces

According to the same graph, it can be noted that for $X_f = 2\,GPa$, another chip formation mechanism is active for fiber orientations greater than $\theta = 135°$. For this fiber orientation interval, the chip does not form by fiber breakage, but the matrix material fails due to excessive shear stress after fiber failure to form the chips. However, for the smaller fiber orientations, the sequence of failure is different, and the matrix material fails before any damage is done to the fibers. Therefore, material mechanical properties have a significant effect on the chip-formation mechanisms.

Figure 6-8 illustrates how the fiber volume fraction interacts with the cutting and thrust forces. As expected, the higher the fiber volume fraction, the higher the cutting forces.

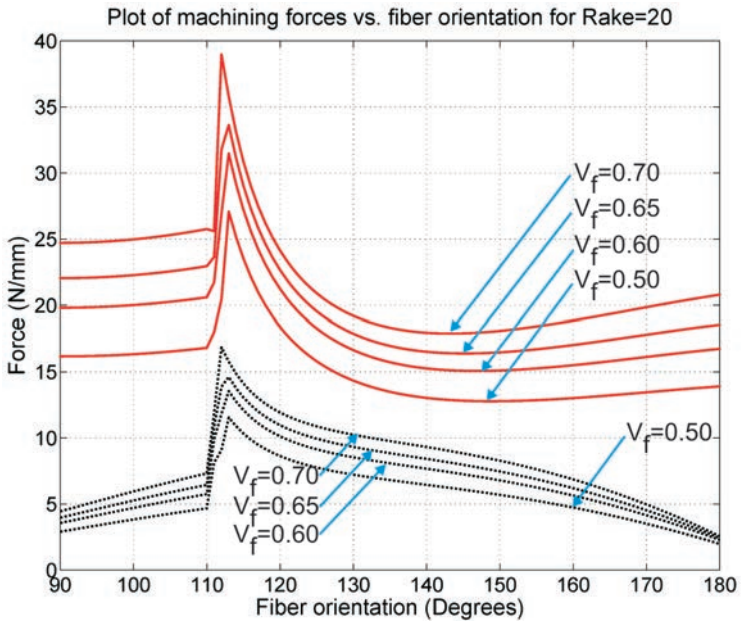

Figure 6-8. Effect of fiber volume fraction on cutting and thrust forces

Fiber flexural strength and the Young modulus are two dependent mechanical properties, and their effect on the cutting forces cannot be presented individually.

However, the effect of fiber Young modulus only on the cutting forces is presented in Figure 6-9.

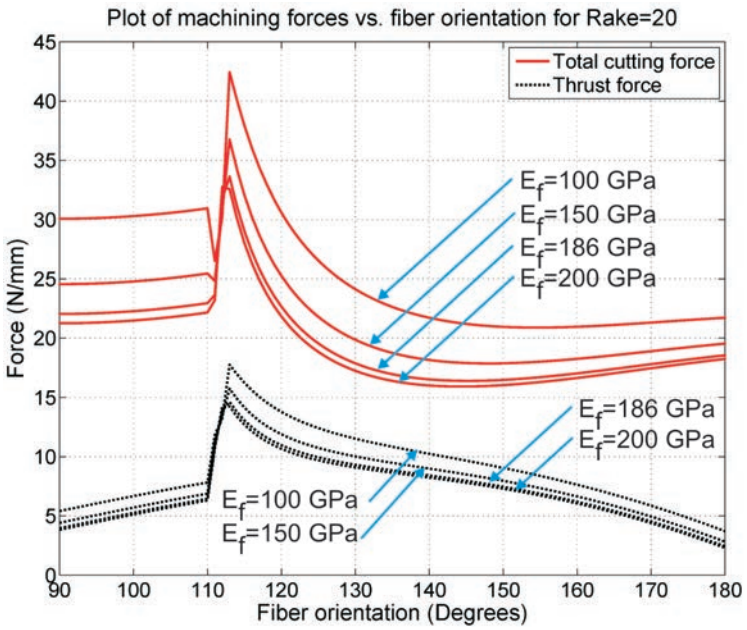

Figure 6-9. Effect of Fiber Young modulus on cutting and thrust forces

6.3. Fiber-Matrix Debonding Length

Similar to machining forces, the fiber-matrix debonding length depends on the material properties, tool geometry, and machining conditions. Figure 6-10 shows the depth of damage along the fibers in each orientation. This plot shows that as the fibers get stiffer, damage increases; however, according to Figure 6-9 the opposite effect can be seen on the machining forces. The fibers break when they reach their flexural strength. A smaller Young modulus lets the fibers bend more until they reach that point, and this will result in higher cutting forces. Figure 6-11 shows that smaller rake angles result in more fiber-matrix debonding as expected; however, smaller rake angles generate lower cutting forces.

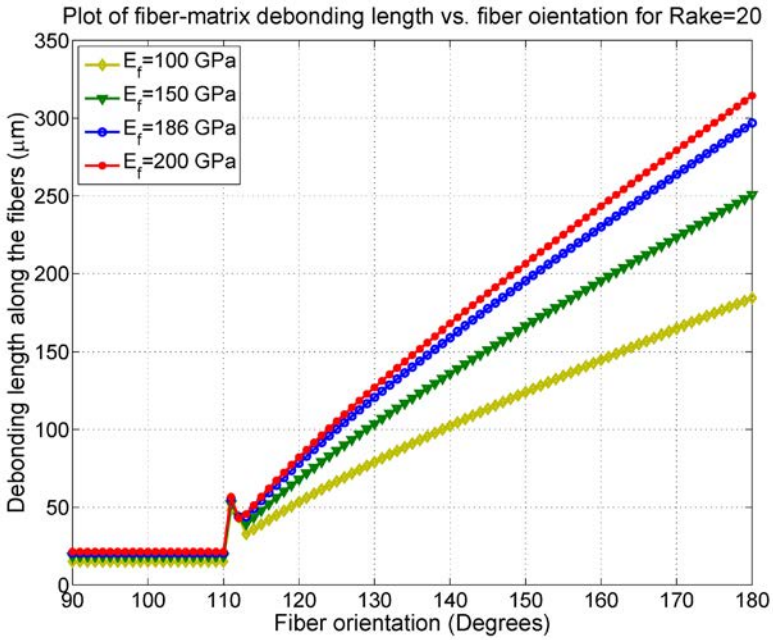

Figure 6-10. Effect of fiber Young modulus on the fiber-matrix debonding length

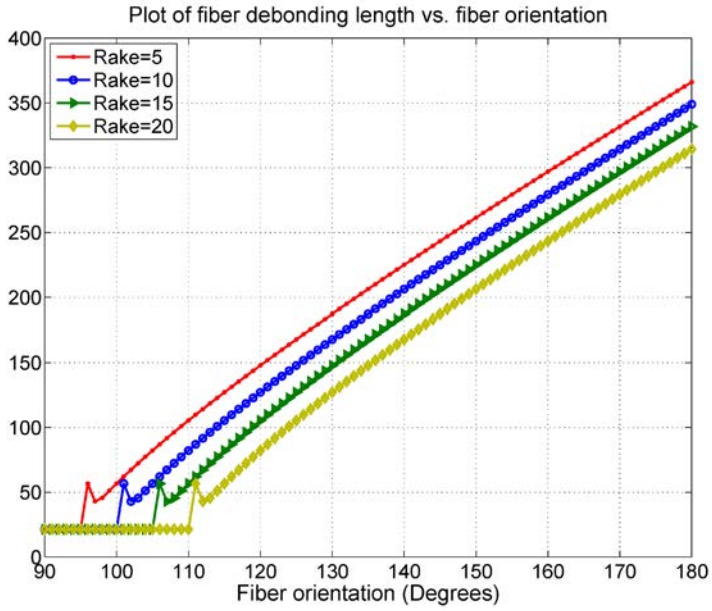

Figure 6-11. Effect of tool rake angle on the fiber-matrix debonding length

Figure 6-12 shows the comparison between the analytical and FEM results of fiber failure length along the fibers, indicating that the theoretical model and FEM are in a good agreement.

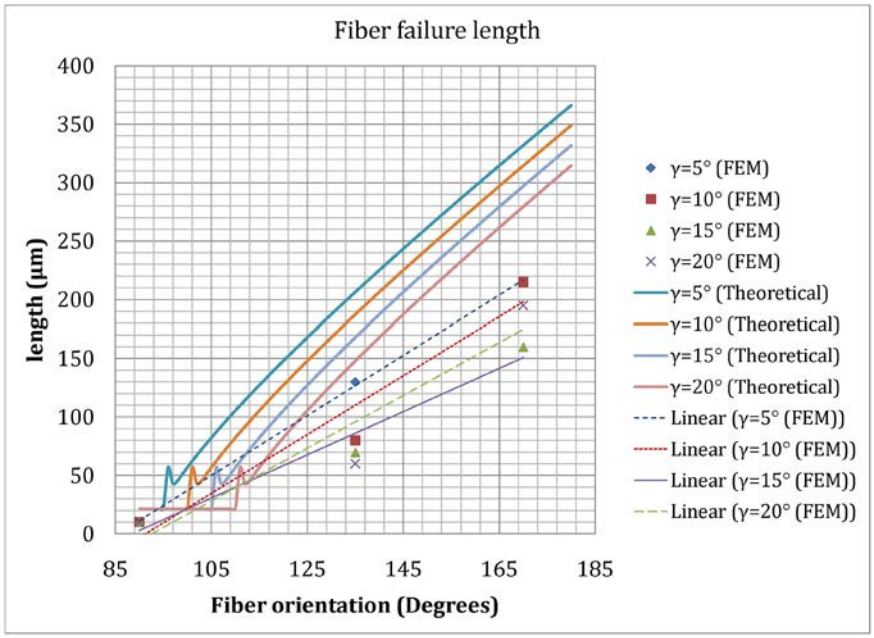

Figure 6-12. Effect of tool rake angle on fiber-matrix debonding length
(Comparison between theoretical and FEM results)

Figure 6-13 andFigure 6-14 show the effect of relief angle on cutting and thrust forces. Here, the relief angle has a minor effect on the machining forces, and as the rake angle increases, the machining forces increase.

According to Figure 6-10, depending on fiber orientation, the depth of damage may vary. Figure 6-15 shows the fiber length limited by the depth of cut and the damage length along the fiber orientation. If L is greater than $-a_c/\sin\theta$, then the composite edge will be damaged after material removal and the damage residue exists. However, if L is smaller than $-a_c/\sin\theta$, then broken fibers will be completely removed from the workpiece, and

the surface quality will be very good without any major or minor defects. Therefore, there exists a certain fiber orientation for any material and tool geometry in which no damage is left after edge trimming. This can be clearly seen in Figure 6-15.

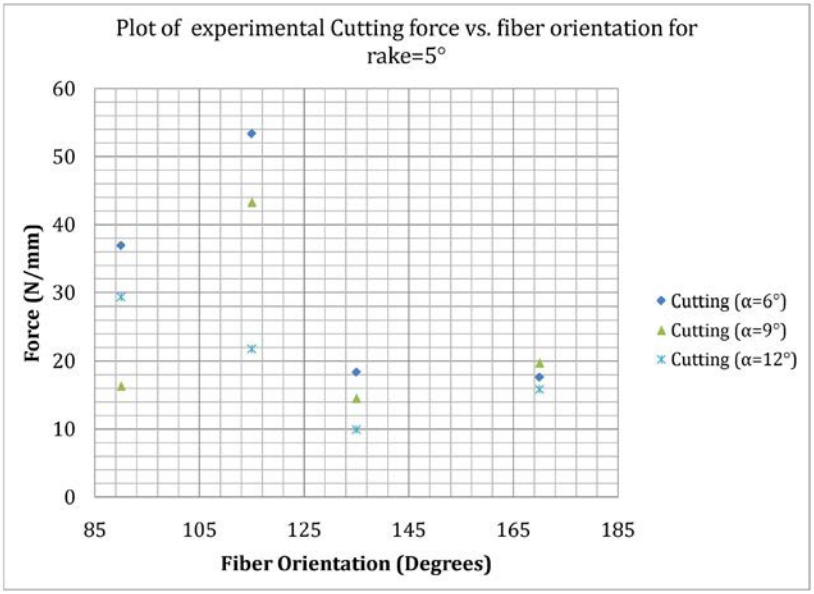

Figure 6-13. Effect of tool relief angle on cutting force (rake=5°)

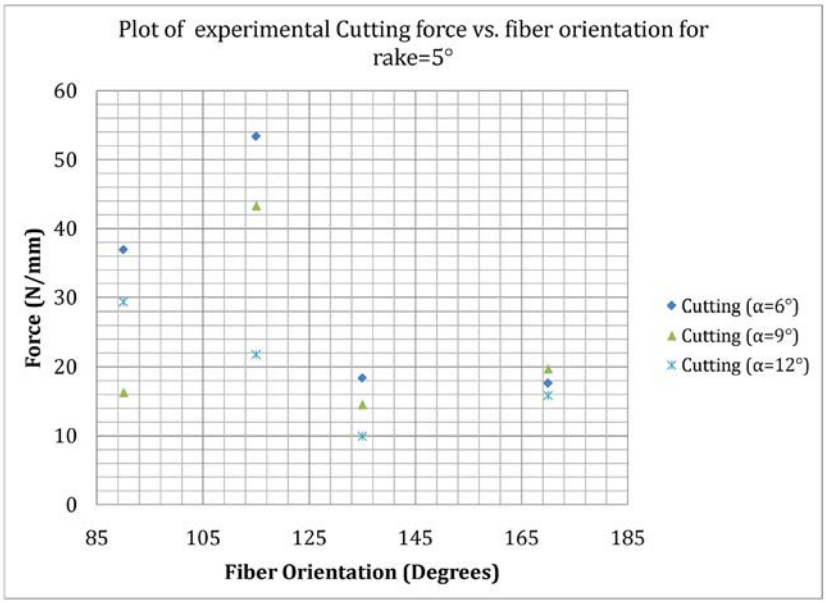

Figure 6-14. Effect of tool relief angle on thrust force (rake=5°)

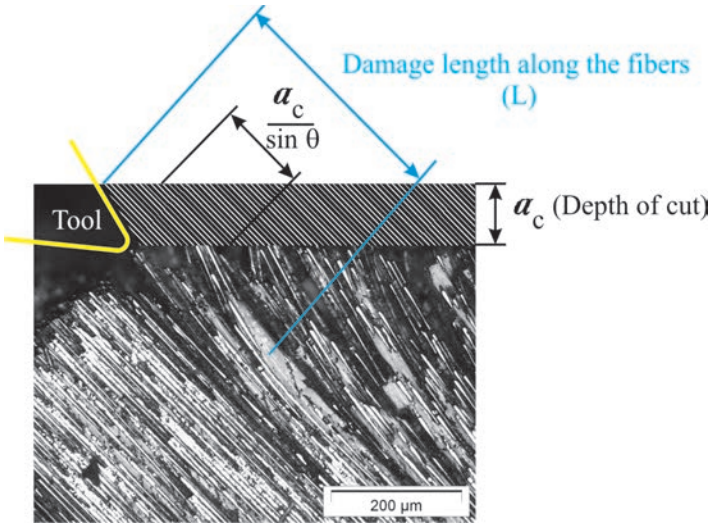

Figure 6-15. Damage residue after edge trimming of unidirectional composites

Figure 6-16,Figure 6-17,Figure 6-18, andFigure 6-19 show the effect of tool rake angle, fiber volume fraction, fiber Young modulus, and matrix shear strength on the depth of damage. These figures illustrate the angles in which damage takes place in the workpiece for various material properties and tool geometries.

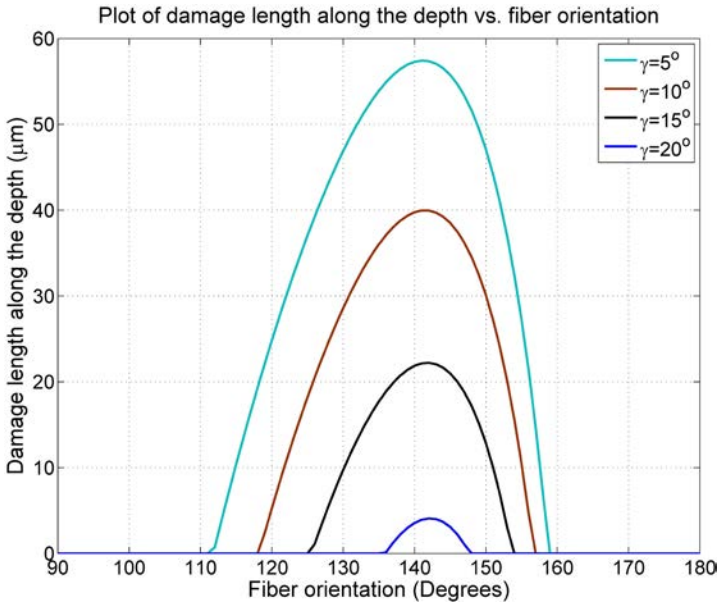

Figure 6-16. Effect of tool rake angle on the fiber-matrix depth of damage

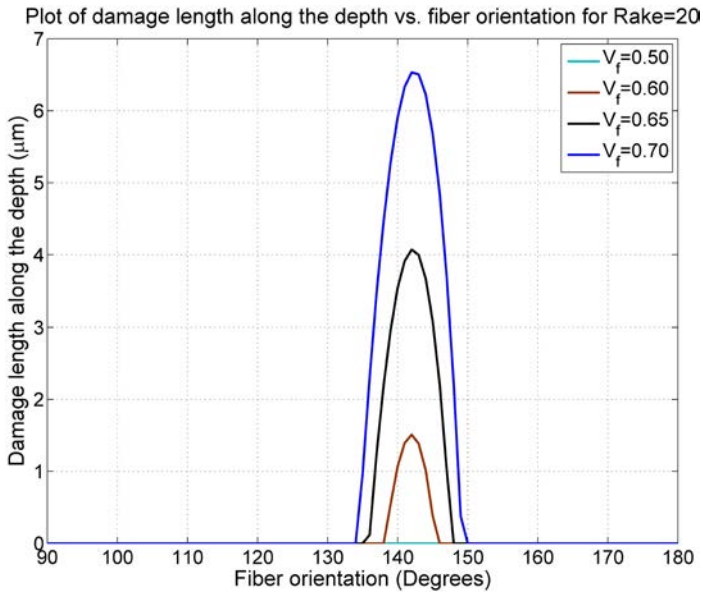

Figure 6-17. Effect of fiber volume fraction on the fiber-matrix depth of damage

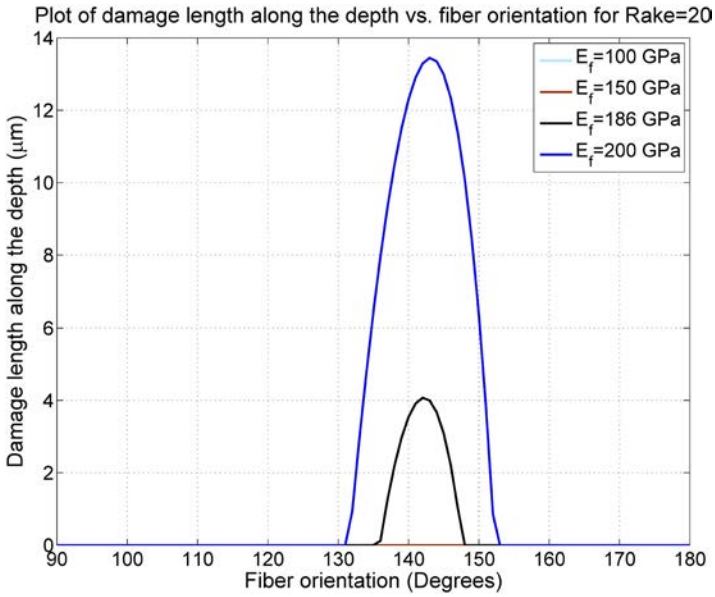

Figure 6-18. Effect of fiber Young modulus on the fiber-matrix depth of damage

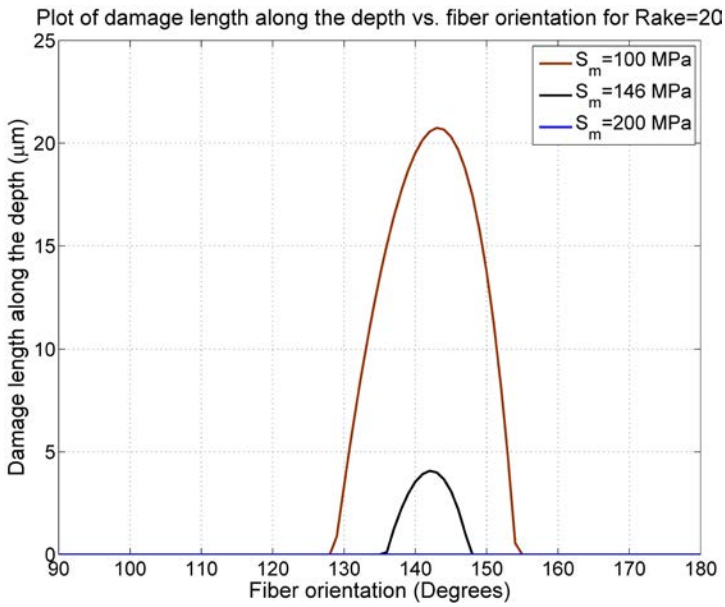

Figure 6-19. Effect of matrix shear strength on the fiber-matrix depth of damage

Figure 6-20 shows the subsurface damage when the fiber orientation $\theta = 90°$ and $\gamma = 5°$. As can be seen from Figure 6-10, the damage along the fiber direction is predicted to be, at most, 20 μm. Since the fiber orientation is 90°, the damaged material will be removed from the cut edge, leaving minor broken fibers or debonded material. Figure 6-21, Figure 6-22, andFigure 6-23 also show the cut material with the same fiber orientation but different rake angles. As predicted, there is minor fiber-matrix debonding.

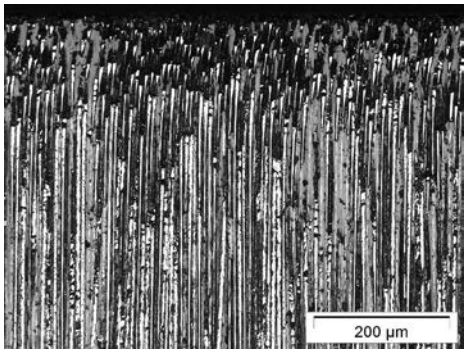

Figure 6-20. Microstructure in subsurface
(fiber orientation = 90°, depth of cut = 0.100mm, rake angle = 5°, relief angle = 6°)

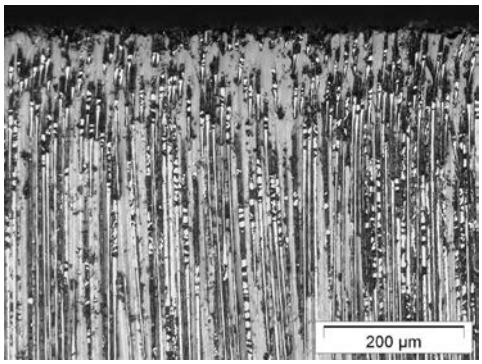

Figure 6-21. Microstructure in subsurface
(fiber orientation = 90°, depth of cut = 0.100mm, rake angle = 10°, relief angle = 6°)

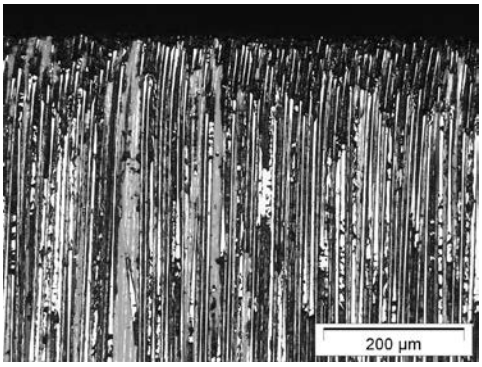

Figure 6-22. Microstructure in subsurface
(fiber orientation = 90°, depth of cut = 0.100mm, rake angle = 15°, relief angle = 6°)

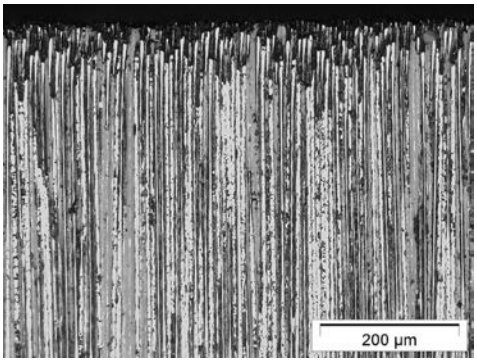

Figure 6-23. Microstructure in subsurface
(fiber orientation = 90°, depth of cut = 0.100mm, rake angle = 20°, relief angle = 6°)

Experiments on the studied material revealed that at $\theta = 135°$, the length of damage exceeds $-a_c / \sin\theta$, and the surface quality after the trimming is poor. Figure 6-24, Figure 6-25, Figure 6-26, and Figure 6-27 show the subsurface damage for this fiber orientation.

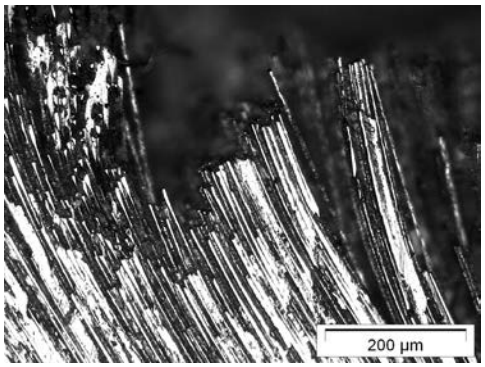

Figure 6-24. Microstructure in subsurface
(fiber orientation = 135°, depth of cut = 0.100mm, rake angle = 5°, relief angle = 6°)

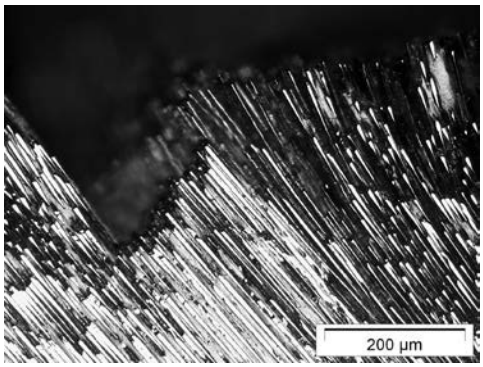

Figure 6-25. Microstructure in subsurface
(fiber orientation = 135°, depth of cut = 0.100mm, rake angle = 10°, relief angle = 6°)

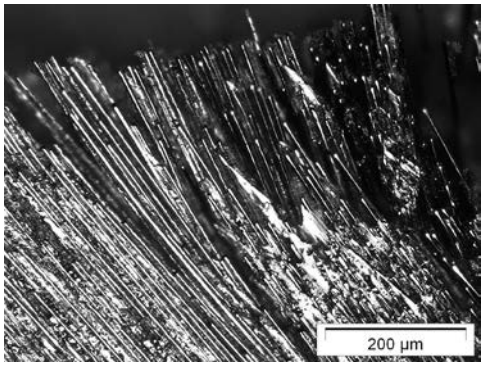

Figure 6-26. Microstructure in subsurface
(fiber orientation = 135°, depth of cut = 0.100mm, rake angle = 15°, relief angle = 6°)

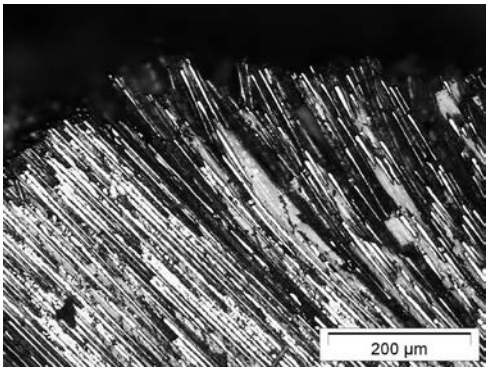

Figure 6-27. Microstructure in subsurface
(fiber orientation = 135°, depth of cut = 0.100mm, rake angle = 20°, relief angle = 6°)

Figure 6-28,Figure 6-29,Figure 6-30, andFigure 6-31 illustrate that for $\theta = 170°$, the debonded material and broken fibers will be completely removed from the trimmed edge leaving a good surface quality.

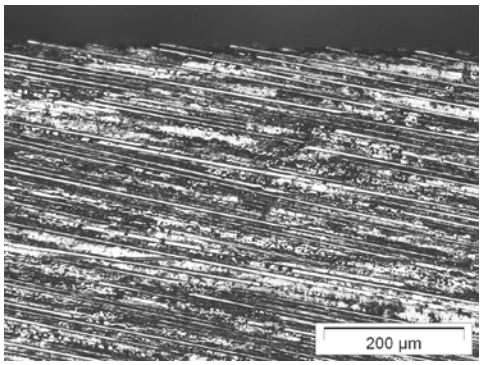

Figure 6-28. Microstructure in subsurface
(fiber orientation = 170°, depth of cut = 0.100mm, rake angle = 5°, relief angle = 6°)

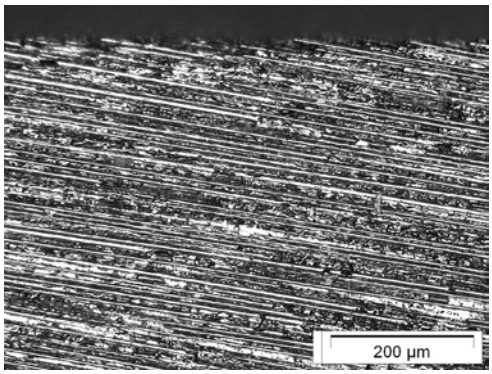

Figure 6-29. Microstructure in subsurface
(fiber orientation = 170°, depth of cut = 0.100mm, rake angle = 10°, relief angle = 6°)

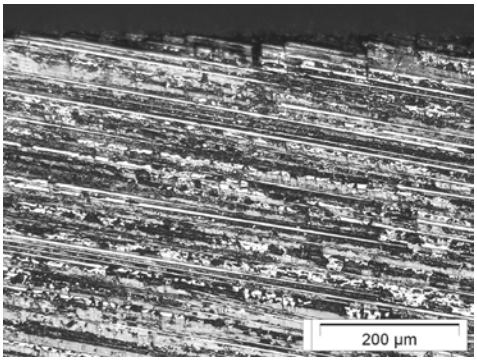

Figure 6-30. Microstructure in subsurface
(fiber orientation = 170°, depth of cut = 0.100mm, rake angle = 15°, relief angle = 6°)

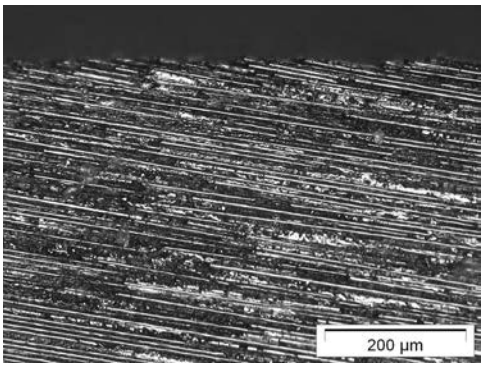

Figure 6-31. Microstructure in subsurface
(fiber orientation = 170°, depth of cut = 0.100mm, rake angle = 20°, relief angle = 6°)

CHAPTER 7

CONCLUSIONS AND FUTURE WORK

The machining of composites is a complicated process, with many parameters involved in the force generated, cutting mechanisms, and quality of the machined surface. These parameters can be divided into three categories: tool geometry, mechanical properties of the material, and machining conditions. Therefore, it is very important to understand the effect of each parameter on the quality of the surface and machining forces.

Cutting force, thrust force, and depth of damage were predicted using a completely theoretical formula for fiber orientations $90° \leq \theta \leq 180°$ and were in good agreement with the experimental results. A finite element model was presented to estimate the depth of damage along the fibers. The FEM and theoretical predictions were close.

The energy method combined with the undulating fibers model gives better force predictions than the straight fibers model.

7.1. Conclusions

Contrary to artificial neural network models, the theoretical model proposed in this study can be applied to any unidirectional fiber composites with elastic-plastic matrix properties, regardless of whether the mechanical properties of the material are comparable to what was used in the experiments in this research.

A theoretical model for machining of unidirectional composites was developed in this research. The model is based on the energy method and virtual work. The model predictions of the forces are in agreement to the experimental results.

While predicting the forces for machining of unidirectional composites, it was found that fiber orientation has a significant effect on the cutting forces and the depth of damage

along the fibers. In addition, the model shows that the bigger the rake angle, the greater the machining forces. This is due to the chip formation mechanisms for fiber orientation $0° \leq \theta \leq 90°$, which is based on matrix shearing and fiber breakage. Fibers break under lower force when they are pushed normal to the fibers or at angles closer to that.

It was also found that the effect of flexural strength is greater at smaller fiber orientations, and as the fiber flexural strength is increased, the cutting and thrust forces also increased. Fiber volume fraction shows the same trend in the machining forces. The model predicts that as the fibers get stiffer, damage along them increases; however, the cutting and thrust forces decrease.

According to the model, the machining forces proportionally increase with the width of cut; however, the effect of depth of cut is complicated.

This model holds good at all depths and widths of cut. It can be used for any rake angle and fiber orientation when $90° \leq \theta \leq 180°$.

The model reflects the effects of material properties including the fiber volume fraction, elastic modulus of the fiber, matrix shear strain strength, fiber diameter, fiber and matrix shear modulus, and fiber flexural strength. In addition to material properties, machining conditions and tool geometry affect the machining forces significantly. These factors can be summarized as the depth and width of cut for the machining conditions and tool rake angle and tool tip radius for the tool geometry. The effect of cutting speed may be considered if the matrix viscoelastic properties are included in the calculations.

Using this method, recommendations for the fiber and matrix selection can be given to minimize machining damage while maintaining the material strength in the desired range.

7.2. Future Work

As discussed, if the viscoelastic properties of the matrix are known, the effect of machining speed can be included in the calculations. The fundamentals of orthogonal cutting of composites is established in this study and can be extended to oblique machining of unidirectional and multidirectional composites using the same approach. It would be interesting to look at the chip formation using a high-speed camera to better understand the mechanisms involved in forming the chips for different fiber orientations and tool rake angles. The high-speed video recording of the machining could be run for both oblique and orthogonal cutting, and for each case, both unidirectional and multidirectional material

REFERENCES

LIST OF REFERENCES

[1] Jones R. M. and Devens K. S., *Mechanics of Composite Materials*, 2nd ed., Taylor & Francis, Inc., 1998.

[2] Reddy J. N., *Mechanics of Laminated Composite Plates: Theory and Analysis*, CRC Press, Inc, 1996.

[3] König W., Wulf Ch., Graß P., and Willerscheid H., "Machining of Fiber Reinforced Plastics," *CIRP Annals - Manufacturing Technology,* vol. 34, pp. 537-548, 1985.

[4] Kalla D. V., "Committee Neural Network Force Prediction Model in Milling of Fiber Reinforced Polymers," Ph.D. dissertation, Department of Industrial and Manufacturing Engineering, Wichita State University, Wichita, 2008.

[5] Koshal D., *Manufacturing Engineering's Reference Book*, Elsevier, 1993.

[6] *Marks' Standard Handbook for Mechanical Engineers*, 10th ed., McGraw-Hill, 1996.

[7] Boothroyd G., *Fundamentals of Metal Machining and Machine Tools*. Washington, D.C., McGraw-Hill Book Company, 1975.

[8] Merchant M. E., "Basic mechanics of the metal-cutting process," *ASME Journal of Applied Mechanics,* vol. 11, 1944.

[9] Altintas Y., *Manufacturing Automation: Metal Cutting Mechanics, Machine Tool Vibrations, and CNC Design*, Cambridge University Press, 2000.

[10] M.C. Shaw, N.H. Cook, and P.A. Smith, "The Mechanics of Three Dimensional Cutting Operations," *Transactions ASME,* vol. 74, p. 10, 1952.

[11] Armarego E. J. A. and Whitfield R. C., "Computer Based Modelling of Popular Machining Operations for Force and Power Prediction," Palermo, Italy, 1985, pp. 65-69.

[12] Kaw A. K., *Mechanics of Composite Materials*, CRC Press, 1997.

[13] Peters S. T., Ed., *Handbook of Composites*. Springer - Verlag, 1998.

[14] Sahraie-Jahromi A., Bahr B., Bassi R., and Kolhar A. S., "Effects of Slugger Drill Bits in Drilling of Composites," in *2007 ASME International Mechanical Engineering Congress and Exposition*, Seattle, WA, USA, 2007.

[15] Komanduri R., "Machining of fiber-reinforced composites," *Machining Science and Technology,* vol. 1, pp. 113-152, 1997.

[16] Koplev A., Lystrup A., and Vorm T., "Cutting Process, Chips, and Cutting Forces in Machining CFRP," *Composites,* vol. 14, pp. 371-376, 1983.

[17] Kaneeda T., "CFRP Cutting Mechanism," in *16th North American Manufacturing Research Conference*, 1989, pp. 216-221.

[18] Wang D. H., Ramulu M., and Arola D., "Orthogonal cutting mechanisms of graphite/epoxy composite. Part I: unidirectional laminate," *International Journal of Machine Tools & Manufacture,* vol. 35, p. 1623, 1995.

[19] Wang D. H., Ramulu M., and Arola D., "Orthogonal cutting mechanisms of graphite/epoxy composite. Part II: multi-directional laminate," *International Journal of Machine Tools & Manufacture,* vol. 35, p. 1639, 1995.

[20] Arola D., Ramulu M., and Wang D. H., "Chip formation in orthogonal trimming of graphite/epoxy composite," in *Composites Part a-Applied Science and Manufacturing* vol. 27A, ed, 1996.

[21] Takeyama H. and Iijima N., "Machinability of Glass Fiber Reinforced Plastics and Application of Ultrasound Machining," *Annals of the CIRP,* vol. 37, 1988.

[22] Bhatnagar N., Ramakrishnan N., Naik N. K., and Komanduri R., "On the machining of fiber reinforced plastic (FRP) composite laminates," *International Journal of Machine Tools & Manufacture,* vol. 35, pp. 701-716, 1995.

[23] Zhang L. C., Zhang H. J., and Wang X. M., "A force Prediction Model for Cutting Unidirectional Fiber-Reinforced Plastics," *Machining Science and Technology,* vol. 5, pp. 293-305, 2001.

[24] Wang X. M. and Zhang L. C., "An experimental investigation into the orthogonal cutting of unidirectional fiber reinforced plastics," *International Journal of Machine Tools and Manufacture,* vol. 43, pp. 1015-1022, 2003.

[25] Everstine G. C. and Rogers T. G., "A theory of chip formation of FRP composite materials," *J. Comp. Mater.,* vol. 5, 1971.

[26] Iosipescu N., "New accurate procedure for single shear testing of metals," *Journal of Materials,* vol. 2, pp. 537-566, Sept. 1967 1967.

[27] Arola D. and Ramulu M., "Orthogonal cutting of fiber-reinforced composites: A finite element analysis," *International Journal of Mechanical Sciences,* vol. 39, pp. 597-613, 1997.

[28] Bhatnagar N., Nayak D., Singh I., Chouhan H., and Mahajan P., "Determination of machining-induced damage characteristics of fiber reinforced plastic composite laminates," *Materials and Manufacturing Processes,* vol. 19, pp. 1009-23, 2004.

[29] Mahdi M. and Zhang L., "A finite element model for the orthogonal cutting of fiber-reinforced composite materials," *Journal of Materials Processing Technology,* vol. 113, pp. 373-377, 2001.

[30] Hashish M., "Machining of advanced composites with abrasive-waterjets," *Manufacturing Review,* vol. 2, pp. 142-150, 1989.

[31] Mello M. D., "Laser Cutting of Non-Metalic Composites," Quebec City, Que, Can, 1986, pp. 288-290.

[32] Colligan K., Ramulu M., and Arola D., "Investigation of edge quality and ply delamination in abrasive waterjet machining of graphite/epoxy," New York, NY, USA, 1993, pp. 167-185.

[33] Hamatani G. and Ramulu M., "Machinability of high temperature composites by abrasive waterjet," *Journal of Engineering Materials and Technology, Transactions of the ASME,* vol. 112, pp. 381-386, 1990.

[34] Liu H. T., "Machining honeycomb composites with abrasive-waterjets," Bedfordshire, MK43 0AJ, United Kingdom, 2006, pp. 153-166.

[35] Shanmugam D. K., Nguyen T., and Wang J., "A study of delamination on graphite/epoxy composites in abrasive waterjet machining," *Composites Part A: Applied Science and Manufacturing,* vol. 39, pp. 923-9, 2008.

[36] Wang J., "Abrasive waterjet machining of polymer matrix composites - cutting performance, erosive process and predictive models," *International Journal of Advanced Manufacturing Technology,* vol. 15, pp. 757-768, 1999.

[37] Wang J., "Machinability study of polymer matrix composites using abrasive waterjet cutting technology," *Journal of Materials Processing Technology,* vol. 94, pp. 30-35, 1999.

[38] Wang J., Kuriyagawa T., and Huang C. Z., "An experimental study to enhance the cutting performance in abrasive waterjet machining," *Machining Science and Technology,* vol. 7, pp. 191-207, 2003.

[39] Douglas L., "Laser trimming of graphite-epoxy laminates," *Annual Forum Proceedings - American Helicopter Society,* vol. 2, pp. 1766-1773, 1999.

[40] Wang X. and Zhang L., "Machining Damage in Unidirectional Fiber-Reinforced Plastics," *World Scientific,* p. 8, 1999.

[41] Zhang L. C., *Solid mechanics for engineers*, Basingstoke: Palgrave, 2001.

[42] Johnson K. L., *Contact Mechanics*, Cambridge University Press, 2008.

[43] Dandekar C. R. and Shin Y. C., "Multiphase Finite Element Modeling of Machining Unidirectional Composites: Prediction of Debonding and Fiber Damage," *Journal of Manufacturing Science and Engineering,* vol. 130, pp. 051016-12, 2008.

[44] "ABAQUS Analysis User's Manual," 6.8 ed: SIMULIA, 2008.

[45] Hobbiebrunken T., Fiedler B., Hojo M., Ochiai S., and Schulte K., "Microscopic yielding of CF/epoxy composites and the effect on the formation of thermal residual stresses," *Composites Science and Technology,* vol. 65, pp. 1626-35, 2005.

[46] Arola D., Sultan M. B., and Ramulu M., "Finite element modeling of edge trimming fiber reinforced plastics," *Journal of Manufacturing Science and Engineering, Transactions of the ASME,* vol. 124, pp. 32-41, 2002.

[47] Nayak D., Bhatnagar N., and Mahajan P., "Machining studies of UD-FRP composites. Part 2: finite element analysis," *Machining Science and Technology,* vol. 9, pp. 503-28, 2005.

[48] Venu Gopala Rao G., Mahajan P., and Bhatnagar N., "Machining of UD-GFRP composites chip formation mechanism," *Composites Science and Technology,* vol. 67, pp. 2271-2281, 2007.

[49] "ABAQUS Benchmark Manual (v6.8)," 6.8 ed: SIMULIA, 2008.

[50] Hawthorne H. M. and Teghtsoonian E., *Journal of Materials Science,* vol. 10, pp. 41-51, 1975.

[51] Greszczuk L. B., "Microbuckling of Lamina-Reinforced Composites," presented at the Composite Materials: Testing and Design (Third Conference), 1974.

[52] Greszczuk L. B., "Microbuckling failure of circular fiber-reinforced composites," *AIAA Journal,* vol. 13, pp. 1311-18, 1975.

[53] Herrmann L. R., Mason W. R., and Chan S. T. K., "Behavior of Compressively Loaded Reinforcing Wires," ed, 1998.

[54] Davis J. G., ed. Philadelphia: American Society for Testing and Materials, 1975, pp. 364-377.

[55] Wang A. S. D., "Non-Linear Microbuckling Model Predicting the Compressive Strength of Unidirectional Composites," *American Society of Mechanical Engineers (Paper),* p. 8, 1978.

[56] Budiansky B., "Micromechanics," *Computers & Structures,* vol. 16, pp. 3-12, 1983.

[57] Argon A. S., "Fracture of composites," in *Treatise on Materials Science and Technology vol.1*, ed London, UK: Academic Press, 1972, pp. 79-114.

[58] Hanasaki S. and Hasegawa Y., *Journal of Composite Materials,* vol. 8, pp. 306-309, 1974.

[59] Reifsnider K. L. and Case S. W., *Damage Tolerance and Durability of Material Systems*, John Wiley, 2002.

[60] Hahn H. T. and Williams J. G., "Compression Failure Mechanisms in Unidirectional Composites," presented at the Composite Materials: Testing and Design (Seventh Conference), ASTM STP 893, Philadelphia, 1968.

[61] Timoshenko S. P., *Theory of Elastic Instability*, 2nd edition ed., McGraw-Hill Companies, 1961.

[62] Reddy J. N., *Theory and Analysis of Elastic Plates and Shells*, CRC Press, 2006.

[63] Megson T. H. G. and Gordon Thomas Henry, *Structural and stress analysis*. London, Arnold, 1996.

[64] Ramesh M. V., Seetharamu K. N., Ganesan N., and Sivakumar M. S., "Analysis of machining of FRPs using FEM," *International Journal of Machine Tools & Manufacture,* vol. 38, pp. 1531-1549, 1998.

[65] Bhatnagar N., Rao G. V. G., and Mahajan P., "Micro-mechanical modeling of machining of FRP composites - Cutting force analysis," *Composites Science and Technology,* vol. 67, pp. 579-93, 2007.

[66] Sahraie-Jahromi A., Chennakesavelu G., Gudimani G., and Bahr B., "Study of Damaged Area in Drilling of Composites with DOE analysis," in *SAMPE 09*, Baltimore, MD, USA, 2009.

[67] (2003, *Cahrge Amplifier, Dual Mode Charge Amplifier with PIEZOTRON Operating Mode*. Available: http://www.intertechnology.com/Kistler/pdfs/ACC_5010_Charge_Amplifier.pdf

[68] (2005, *Component Dynamometer for cutting measurment in drilling*. Available: http://www.helmar.com.pl/helmar/biblioteka/pdf/9272.pdf

[69] (2003-2005, *NI 6023E/6024E/6025E Family Specifications*. Available: http://www.ni.com/pdf/manuals/370719c.pdf

[70] Tomblin J., McKenna J., Ng Y., and Raju K. S., "Basis Design Allowables for Epoxy – Based Prepreg - Newport Carbon Plain Weave Fabric 3K70P / NB321," National Institute for Aviation Research - Wichita State University, WichitaJul. 2001 2001.

[71] "Newport 321 Product Data Sheet," Newport Adhesives and Composites, Inc.

[72] Batdorf S. B., "Tensile Strength of Unidirectionally Reinforced Composites," in *Proceedings of the U.S. National Congress of Applied Mechanics*, New York, NY, USA, 1982, p. 484.

[73] Caliskan A. G., "Micromechanics-Based Approach to Predict Strength and Stifness of Composite Materials," M. S., Virginia Polytechnic Institute and State University, 1996.

APPENDIX

APPENDIX

MATLAB PROGRAM FOR THE FORCE AND DEBONDING LENGTH CALCULATIONS

```
%##########################################################################
%This MATLAB code calculates the cutting forces in machining of
%unidirectional composites for fiber orentations greater than 90 degrees
%This program is a part of Ashkan Sahraie Jahromi's PhD thesis
%##########################################################################
%Thrust force included in this code version
clear all;
clc
%--------------------------------------------------------------------------
%                             Defining constants
%--------------------------------------------------------------------------
syms l S1 S2 x phi real;
k = listdlg('PromptString','What is the working units?',...
                'SelectionMode','single',
'ListString',{'English','Metric'},...
                'Name','Unit Selector','ListSize',[180 50]);
switch k
    case 1
        disp 'English units selected'
        prompt = {'Fiber Diameter (in)','Depth of Cut (in)','Width of Cut
(in)',...
            'Fiber Volume Fraction','Fiber Young''s Modulus (psi)','Fiber
Flexural Strength (psi)',...
            'Matrix Shear Modulus (psi)','Fiber Poison''s Ratio','Matrix
Shear Strength (psi)','Matrix Ultimate Strain',...
            'Tool Rake Angle (Deg)','Tool Tip Radius (in)','Friction
Coefficient'};
        dlg_title = 'Input Machining Conditions';
        num_lines = 1;
        def = {'2.72e-4','3.94e-3','3.94e-
2','0.65','2.9e7','435113.2','198701.7','0.3','21175.5','0.1','20','7.9e-
5','0.18'};
    case 2
        disp 'Metric units selected'
        prompt = {'Fiber Diameter (m)','Depth of Cut (m)','Width of Cut
(m)',...
            'Fiber Volume Fraction','Fiber Young''s Modulus (N/m^2)','Fiber
Flexural Strength (N/m^2)',...
            'Matrix Shear Modulus (N/m^2)','Fiber Poison''s Ratio','Matrix
Shear Strength (N/m^2)',...
            'Matrix Ultimate Strain', 'Tool Rake Angle (Deg)','Tool Tip
Radius (m)','Friction Coefficient'};
        dlg_title = 'Input Machining Conditions';
        num_lines = 1;
        def = {'6.9e-6','1e-4','1e-
3','0.65','200e9','3000e6','1.37e9','0.3','146e6','0.1','20','2e-6','0.18'};
end
options.Resize='on';
options.WindowStyle='normal';
options.Interpreter='tex';
```

```
prop = str2double(inputdlg(prompt,dlg_title,num_lines,def,options));
df=prop(1);
t=prop(3);
H=prop(2);
Vf=prop(4);
Ef=prop(5);
Xf=prop(6);
Gm=prop(7);
nuf=prop(8);
Gf=Ef/(2*(1+nuf));
epsc=prop(10);
Sm=prop(9);
Rake=prop(11);
rake=Rake*pi()/180;
mu=prop(13);
Re=prop(12);
%-------------------------------------------------------------------------
%                            Evaluating Peoperties
%-------------------------------------------------------------------------
a=df/2;
Vm=1-Vf;
c=(df/2)*(Vm/Vf);
If=t*df^3/12;
% Vf=(df/2)/(c+df/2);
% Vm=c/(c+df/2);
G_LT=Gf*Gm/(Gf*Vm+Gm*Vf);
A=-Gm*c*t*(1+(df/2)/c)^2;
B1=sqrt(-A/(Ef*If));
n=0;
Forces=[0,0,0,0];
li=70e-6;
for i=90:2:180
    i
    n=n+1;
    X(n)=i;
    theta=i*pi()/180;
    gamma_m=-(theta-rake-pi()/2);
%-------------------------------------------------------------------------
%                                Equations
%-------------------------------------------------------------------------
    v1=S1*(sinh(B1*l)*cosh(B1*x)-cosh(B1*l)*sinh(B1*x)-
sinh(B1*l)+cosh(B1*l)*x*B1)/(B1^3*If*Ef);
    v2=-1/6*S2/Ef/If*x^3+1/4*(2*gamma_m*Ef*If+S2*l^2)/l/Ef/If*x^2;

U1=int(Ef*If*(diff(v1,x,2))^2,x,0,l)/2+c*t*Gm*int((diff(v1,x)^2),x,0,l)*(1+(d
f/2)/c)^2/2-int(S1*diff(v1,x),x,0,l);
    U2=int(Ef*If*(diff(v2,x,2))^2,x,0,l)/2+c*t*(-
l*(Sm^2/(2*Gm))+int(diff(v2,x),x,0,l)*Sm*(1+(df/2)/c))-
int(S2*diff(v2,x),x,0,l);
    eps1=(1+(df/2)/c)*diff(v1,x)-epsc;
    Sub_eps1=subs(eps1,x,0.001*l);
    sigma_max1=Ef*diff(v1,x,2)*df/2-Xf;
    Sub_sigma_max1=subs(sigma_max1,x,0);
    eps2=(1+(df/2)/c)*diff(v2,x)-epsc;
    Sub_eps2=subs(eps2,x,-1e-3*l);
    sigma_max2=Ef*diff(v2,x,2)*df/2-Xf;
    Sub_sigma_max2=subs(sigma_max2,x,0);
```

```
%-------------------------------------------------------------------------
%                                Solution
%-------------------------------------------------------------------------
    if (i-90) <= (Rake)
        SolS_shear=solve(Sub_eps1,S1);
        Soll_shear=subs(U1,S1,SolS_shear);
        SolS_bend=solve(Sub_sigma_max1,S1);
        Soll_bend=subs(U1,S1,SolS_bend);
        FShear = @(length_shear)[subs(Soll_shear,l,length_shear)];
        FBend = @ (length_bend)[subs(Soll_bend,l,length_bend)];
        options=optimset('Display','iter','TolFun',1e-12,'TolX',1e-
14,'NonlEqnAlgorithm','dogleg','LineSearchType','quadcubic','MaxFunEvals',70)
;
        [length_shear,Shear] = fsolve(FShear,li,options)
        [length_bend,BendStress] = fsolve(FBend,li,options)
        force_shear=subs(SolS_shear,l,length_shear)
        force_bend=subs(SolS_bend,l,length_bend)
        Energy_bend=subs(U1,{l,S1},{length_bend,force_bend})
        Energy_shear=subs(U1,{l,S1},{length_shear,force_shear})
        CForce_Debonding=(-max(abs(force_bend),abs(force_shear))*Vf*H/a);
        TForce_Friction=-CForce_Debonding*mu;
        CForce_Radius=G_LT*df^2*pi()/4*t/(2*c+df)*cos(theta);
        CForce_Total=CForce_Radius+CForce_Debonding;
        length(n)=length_bend;
    else
        SolS_shear=solve(Sub_eps2,S2);
        Soll_shear=subs(U2,S2,SolS_shear);
        SolS_bend=solve(Sub_sigma_max2,S2);
        Soll_bend=subs(U2,S2,SolS_bend);
        FShear = @(length_shear)[subs(Soll_shear,l,length_shear)];
        FBend = @ (length_bend)[subs(Soll_bend,l,length_bend)];
        options=optimset('Display','iter','TolFun',1e-12,'TolX',1e-
14,'NonlEqnAlgorithm','dogleg','LineSearchType','quadcubic','MaxFunEvals',700
);
        [length_shear,Shear] = fsolve(FShear,li,options)
        [length_bend,BendStress] = fsolve(FBend,li,options)
        force_shear=subs(SolS_shear,l,length_shear)
        force_bend=subs(SolS_bend,l,length_bend)
        Energy_bend=subs(U2,{l,S2},{length_bend,force_bend})
        Energy_shear=subs(U2,{l,S2},{length_shear,force_shear})
        CForce_Debonding=(-
max(abs(force_bend),abs(force_shear))*Vf*H/a)/cos(rake);
        CForce_Friction=-CForce_Debonding*mu*sin(rake);
        TForce_Friction=-CForce_Debonding*sin(rake);
        CForce_Radius=G_LT*df^2*pi()/4*t/(2*c+df)*cos(theta);
        CForce_Total=CForce_Radius+CForce_Debonding+CForce_Friction;
        li=length_bend;
        length(n)=length_bend;
    end
    TForce=G_LT*df^2*pi()/4*t/(c+df)*sin(theta)+TForce_Friction;
    Forces(n,:)=[-CForce_Debonding,-CForce_Radius,-CForce_Total,TForce];
end
plot(X,Forces(:,1),'*-',X,Forces(:,2),'.-',X,Forces(:,3),'+-
',X,Forces(:,4),'black--')
hold on
switch Rake
    case 5
```

```
%-------------------------------------------------------------------------
%                                Cutting - Thrust
%-------------------------------------------------------------------------

plot([90,90,90],[32.4,32.9,45],'redsquare',[90,90,90],[17.8,18.2,19.1],'black
hexagram')

plot([115,115,115],[51.6,60.9,47.6],'redsquare',[115,115,115],[8.4,8,7.6],'bl
ackhexagram')

plot([135,135,135],[13.3,16.9,24.9],'redsquare',[135,135,135],[2.2,1.8,2.7],'
blackhexagram')

plot([170,170,170],[10.7,20.46,21.8],'redsquare',[170,170,170],[8.9,13.7,14.2
],'blackhexagram')
        title('Plot of machining forces vs. fiber orientation for Rake=5')
%-------------------------------------------------------------------------
    case 10
%-------------------------------------------------------------------------
%                                Cutting - Thrust
%-------------------------------------------------------------------------

plot([90,90,90],[20.9,25.8,42.25],'redsquare',[90,90,90],[10.7,12.9,14.7],'bl
ackhexagram')

plot([115,115,115],[47.1,48.9,61.4],'redsquare',[115,115,115],[4.9,4,5.3],'bl
ackhexagram')

plot([135,135,135],[12.9,17.8,15.6],'redsquare',[135,135,135],[2.2,2.2,2.6],'
blackhexagram')

plot([170,170,170],[15.6,18.7,17.8],'redsquare',[170,170,170],[10.2,2.2,11.6]
,'blackhexagram')
        title('Plot of machining forces vs. fiber orientation for Rake=10')
%-------------------------------------------------------------------------
    case 15
%-------------------------------------------------------------------------
%                                Cutting - Thrust
%-------------------------------------------------------------------------

plot([90,90,90],[35,29.8,43],'redsquare',[90,90,90],[11.4,9.9,9.9],'blackhexa
gram')

plot([115,115,115],[53.4,58.7,33.8],'redsquare',[115,115,115],[3.5,3.1,2.6],'
blackhexagram')

plot([135,135,135],[16.8,21.3,16],'redsquare',[135,135,135],[1.8,2.2,1.9],'bl
ackhexagram')

plot([170,170,170],[9.8,14.4,17.4],'redsquare',[170,170,170],[6.2,8.2,9.1],'b
lackhexagram')
        title('Plot of machining forces vs. fiber orientation for Rake=15')
%-------------------------------------------------------------------------
    case 20
%-------------------------------------------------------------------------
%                                Cutting - Thrust
%-------------------------------------------------------------------------
```

```
plot([90,90,90],[25.9,41,32.9],'redsquare',[90,90,90],[16.9,16.2,10.4],'black
hexagram')

plot([115,115,115],[56.9,52,43.5],'redsquare',[115,115,115],[3.1,3.1,3.1],'bl
ackhexagram')

plot([135,135,135],[15.1,16.8,19.1],'redsquare',[135,135,135],[1.3,1,1.2],'bl
ackhexagram')

plot([170,170,170],[11,13.2,12.9],'redsquare',[170,170,170],[8.4,9.1,10.2],'b
lackhexagram')
        title('Plot of machining forces vs. fiber orientation for Rake=20')
%-------------------------------------------------------------------------
end
switch k
    case 1
        xlabel('Fiber orientation (Degrees)')
        ylabel('Force (Pound/inch)')
        p = legend('Bending force (Cutting)','Buckling force
(Cutting)','Total cutting force','Thrust force','Experimental cutting
force','Experimental thrust force',1);
        set(p,'Interpreter','none')
        grid on
    case 2
        xlabel('Fiber orientation (Degrees)')
        ylabel('Force (N/mm)')
        p = legend('Bending force (Cutting)','Buckling force
(Cutting)','Total cutting force','Thrust force','Experimental cutting
force','Experimental thrust force',1);
        set(p,'Interpreter','none')
        grid on
end
figure
switch k
    case 1
        plot(X,length*10^6)
        xlabel('Fiber orientation (Degrees)')
        ylabel('Debonding length along the fibers (\muin)')
        hold on
        grid on
    case 2
        plot(X,length*10^6)
        xlabel('Fiber orientation (Degrees)')
        ylabel('Debonding length along the fibers (\mum)')
        hold on
        grid on
end
```